MINISTÉRIO DA EDUCAÇÃO
UNIVERSIDADE FEDERAL DO RIO GRANDE DO SUL
PROGRAMA DE PÓS-GRADUAÇÃO EM ENGENHARIA MECÂNICA

PROJETO INVERSO APLICADO À MODELAGEM DE SISTEMAS DE ACUMULAÇÃO DE ENERGIA TÉRMICA SENSÍVEL

por

Tiago Haubert Andriotty

Tese para obtenção do Título de
Doutor em Engenharia

Porto Alegre, Dezembro de 2018

PROJETO INVERSO APLICADO À MODELAGEM DE SISTEMAS DE ACUMULAÇÃO DE ENERGIA TÉRMICA SENSÍVEL

por

Tiago Haubert Andriotty
Mestre em Engenharia

Tese submetida ao Corpo Docente do Programa de Pós-Graduação em Engenharia Mecânica, PROMEC, da Escola de Engenharia da Universidade Federal do Rio Grande do Sul, como parte dos requisitos necessários para a obtenção do Título de

Doutor em Engenharia

Área de Concentração: Fenômenos de Transporte

Orientador: Prof. Dr. Paulo Smith Schneider
Coorientador: Prof. Dra. Letícia Jenisch Rodrigues

Aprovada por:

Prof. Dr. Alexandre Kupka da Silva / EMC / UFSC
Prof. Dra. Flávia Schwarz Franceschini Zinani / PPGEM / UNISINOS
Prof. Dr. Luiz Alberto Oliveira Rocha / PROMEC / UFRGS
Prof. Dr. Cirilo Seppi Bresolin / DEMEC / UFRGS

Prof. Dr. Fernando Marcelo Pereira
Coordenador do PROMEC

Porto Alegre, 17 de Dezembro de 2018

AGRADECIMENTOS

Agradeço à Coordenação de Aperfeiçoamento de Pessoal de Nível Superior (CAPES) pelo suporte financeiro para a elaboração desta Tese.

Ao meu orientador, Paulo Smith Schneider, e minha coorientadora, Letícia Jenisch Rodrigues, pela dedicação que demonstraram em me auxiliar.

A UFRGS e ao PROMEC pelo apoio e estrutura fornecidos.

Aos meus colegas e amigos, que de todas as formas me apoiaram e me ajudaram.

RESUMO

Esta Tese desenvolve uma metodologia de dimensionamento para sistemas de acumulação de calor sensível (*Sensible Thermal Energy Storage System* T3S) baseada na filosofia de Projeto Inverso. O T3S opera como um retificador térmico, alimentado por uma fonte com variação cíclica senoidal da temperatura do fluido de trabalho e entrega uma saída retificada desse mesmo fluido. O objetivo do retificador é proporcionar uma operação estável do sistema, diminuindo picos e vales da fonte de entrada, garantida pelo material de acumulação térmica (*Heat Storage Material* HSM) disposto em placas planas paralelas. A modelagem escolhida para descrever o T3S é uma formulação global ou *lumped*, implementada pelo *Lumped Element Model* LEM, capaz de representar as principais características do sistema de acumulação de calor sensível: a geometria, as propriedades do material de acumulação e a energia térmica transportada pelo fluido. Através da combinação das estratégias *one-factor-at-a-time* OFAT e *line search* é encontrada a mínima massa de HSM que garante uma determinada capacidade de retificação (definida pala razão entre as amplitudes da temperatura do fluido na saída e na entrada do T3S). A presente Tese é composta por três artigos. O primeiro (Capítulo 2) aplica a metodologia de planejamento de experimentos Box-Behnken para investigar os desvios do modelo LEM para a amplitude e o deslocamento de fase da temperatura do fluido na saída do T3S em relação a simulações detalhadas em CFD. Os resultados mostram que os desvios para a amplitude são inferiores a 2% em aproximadamente 80% dos casos simulados, enquanto os desvios para o deslocamento de fase não ultrapassam 4%, com apenas um caso fora desse limite. O segundo artigo (Capítulo 3) apresenta a minimização da massa de HSM do T3S para uma condição de operação particularizada. O objetivo é encontrar a menor massa de HSM e sua melhor distribuição (comprimento da placa e distância entre as placas) para retificar a amplitude da temperatura do fluido na entrada, de 30°C, para uma amplitude na saída de 4°C. Infinitas combinações de comprimento e distância entre as placas para a mínima massa de HSM garantem a retificação projetada, porém sempre resultando em um valor ótimo para o Número de Trocas Unitário NTU (4,03) e para a constante de tempo τ (3.230s). O terceiro artigo (Capítulo 4) generaliza os resultados do artigo anterior e apresenta uma metodologia de dimensionamento para T3S operando como um retificador térmico. A aplicação do Projeto Inverso gera uma curva de ajuste para o NTU e outra para o τ, empregadas para dimensionar o T3S submetido a diversas condições de entrada do fluido de trabalho, propriedades do HSM e capacidades de retificação. O caso de estudo apresentado particulariza a obtenção do comprimento, da espessura e da distância entre

as placas do HSM que garantem a retificação projetada, com auxílio de gráficos parametrizados. Os resultados são comparados com simulações pelo método de volumes finitos CFD, mostrando desvios inferiores a 1,5%. O capítulo final sumariza as principais conclusões de cada artigo e propõe o prosseguimento desse estudo.

Palavras-chave: Armazenamento cíclico de energia térmica sensível; Problema inverso; Modelo de elementos Lumped; Otimização; Retificação térmica

ABSTRACT

This Thesis develops a design methodology to optimize a Sensible Thermal Energy Storage System T3S based on the Inverse Problem philosophy. The T3S operates as a thermal rectifier, fed by a working fluid source with time sinusoidal cyclic temperature and delivers a rectified output for the same fluid. The main goal of the rectifier is to provide a stable system operation, reducing the input source peaks and valleys, which is guaranteed by the Heat Storage Material disposed in a set of parallel flat plates. The application of the Inverse Problem methodology allows finding the minimum HSM mass that meets the output imposition for a specified input sinusoidal cyclic function. The T3S is described by a Lumped Element Model LEM, which is able to express the main characteristics of the Sensible Thermal Energy Storage System: geometry, Heat Storage Material properties and air thermal energy. Combining the one-factor-at-a-time OFAT and the line search strategies it is found the minimum HSM mass that ensure the system rectification capacity (defined by the ratio of the fluid temperature amplitudes at outlet and at inlet of the T3S). The present Thesis is composed by three articles. The first one (Chapter 2) applies the Box-Behnken design of experiments methodology to investigate the amplitude and phase deviations of the LEM outlet fluid temperature, compared to detailed simulations in a finite volume method CFD. The amplitude deviations found are less than 2% for approximately 80% of the simulated cases, while the phase deviations do not exceed 4%, with one exceptional case out of this range. The second article (Chapter 3) presents the HSM mass minimization for a particular operational condition. The objective is found the minimum HSM mass and the best configuration (plate length and plate distance) to rectify the inlet fluid temperature amplitude from 30°C to a 4°C fluid outlet temperature amplitude. An infinite combination of plate lengths and distances in respect to the minimum HSM mass ensure the rectification duty, however that combination always converges to optimal values for the Number of Transfer Unit NTU (4.03) and the time constant τ (3,230s). The third article (Chapter 4) generalizes the results of the previous one and presents a design methodology for the optimization of the T3S operating as a thermal rectifier. The application of the Inverse Problem generates individual correlation curves for both NTU and τ, which are employed to design the T3S submitted to different inlet air conditions, HSM properties and rectifying capacities. An example is presented to found the HSM optimal plate length, thickness and spacing that ensure the rectification duty, with the support of parameterized charts. Results are compared to simulations from a finite volume

CFD code, with deviations below 1.5%. The last chapter collects the main conclusions of each article and proposes further researches of this study.

Keywords: Cyclic sensible thermal energy storage; Inverse problem; Lumped element model; Optimization; Thermal rectifier

ÍNDICE

LISTA DE FIGURAS

LISTA DE TABELAS

LISTA DE SIGLAS E ABREVIATURAS

BTES	Armazenamento de calor subterrâneo (*Borehore Thernal Energy Storage*)
CAES	Armazenamento de energia por ar comprimido (*Compressed Air Energy Storage*)
CAPEX	Custo de bens de capital (*CApital EXPenditure*)
CFD	Modelo de elementos finitos (*Computer Fluid Dynamics*)
CSP	Usinas de concentração solar (*Concentrated Solar Power*)
FIR	Função de Integração de Renováveis (*Renewable Integration Function*)
HSM	Material de acumulação térmica (*Heat Storage Material*)
LEM	Modelo de elementos Lumped (*Lumped Element Model*)
LHTES	Armazenamento de calor latente (*Latent Heat Thermal Energy Storage*)
NTU	Número de transferência unitário (*Number of Transfer Unit*)
OFAT	Um fator de cada vez (*One-Factor-At-a-Time*)
ORC	Ciclo orgânico de Rankine (*Organic Rankine Cycle*)
PCM	Material de troca de fase (*Phase Change Material*)
PHES	Armazenamento de calor bombeado (*Pumped Heat Energy Storage*)
PHS	Armazenamento de energia bombeada (*Pumped Hydroelectric Storage*)
PIB	Produto Interno Bruto
PTES	Armazenamento de energia bombeada (*Pumped Thermal Energy Storage*)
PV	Painel fotovoltaico (*PhotoVoltaic*)
SMES	Armazenamento magnético com supercondutor (*Superconducting Magnetic Energy Storage*)
T3S	Sistema de acumulação de calor sensível (*Sensible Thermal Energy Storage System*)
TES	Armazenamento de energia térmica (*Thermal Energy Storage*)

LISTA DE SÍMBOLOS

A_c	cross section area, m²
A_s	solid-fluid interface area, m²
Amp	amplitude, K
c_p	specific heat, J/(kgK)
D_h	hydraulic diameter, m
Dev_{Amp}	temperature amplitude deviation, %
Dev_{Phase}	phase displacement deviation, %
e_f	plate distance / channel thicknesses, m
e_s	plate thicknesses, m
Fo	Fourier number
$\bar{h}$	average heat transfer coefficient, w/m²K
i	OFAT levels
j	generic section
k	thermal conductivity, W/mK
L	plate length, m
L_*	dimensionless length at the thermal entry region
$\dot{m}$	air mass flow rate, kg/s
Ms	HSM mass
Mf	working fluid mass
n	total number of independent sections
N	LEM last section
Nu	Nusselt number
$\overline{Nu}_{D_h}$	average Nusselt correlation for parallel flat plates
p	procedures
P	pressure, Pa
Pe	Peclet number
Pr	Prandtl number
q	average heat transfer rate
q''	heat flux, w/m²
R_p	optimal results matrixes
Re_{D_h}	Reynolds number based on the hydraulic diameter
t	time, s
T	temperature, K
$T_{f-CFD,t,N}$	equivalent temperature value, K
$\overline{T}_{f,j}(t)$	fluid average temperature, K
$\boldsymbol{u}$	velocity vector, m/s
u	velocity, m/s
V	volume, m³
W	unitary width, m
x	axial direction
y	transversal direction

Símbolos gregos:

α	thermal diffusivity, m²/s
μ	dynamic viscosity, Pa.s
β	cycle period, s
γ	average renewable energy power generation factor (fator de geração de potência de energia renovável médio)
ρ	density, kg/m³
τ	time constant, s
Δt	time step, s
θ	dimensionless temperature, rectifying capacity
λ	design parameter, w/K
$\varkappa$	convergence index

Subscritos:

$+$	upper limit
$-$	lower limit
CFD	Computer Fluid Dynamics
f	fluid
i	inicial
in	inlet
k	generic index
LEM	Lumped Element Model
m	periodic mean value
N	LEM last section
$oper$	operational
out	outlet
$Phase$	phase
Ran	Range
s	solid

1 INTRODUÇÃO

O crescimento da população mundial ocorreu, não por coincidência, simultaneamente com a revolução industrial. O aumento da produção industrial gerou avanços tecnológicos que possibilitaram aos governos melhorar a infraestrutura pública (transporte, iluminação, segurança, saúde, etc.), ajudando a sanar os altos índices de mortalidade infantil e as precárias condições de saúde e higienização da população. Neste novo ambiente econômico e social, a riqueza das nações aumentou drasticamente e parcelas da população que antes trabalhavam somente para a própria subsistência, podiam almejar uma melhor qualidade de vida. Esta sistemática é mantida até os dias atuais, como pode ser observado na Figura 1.1.

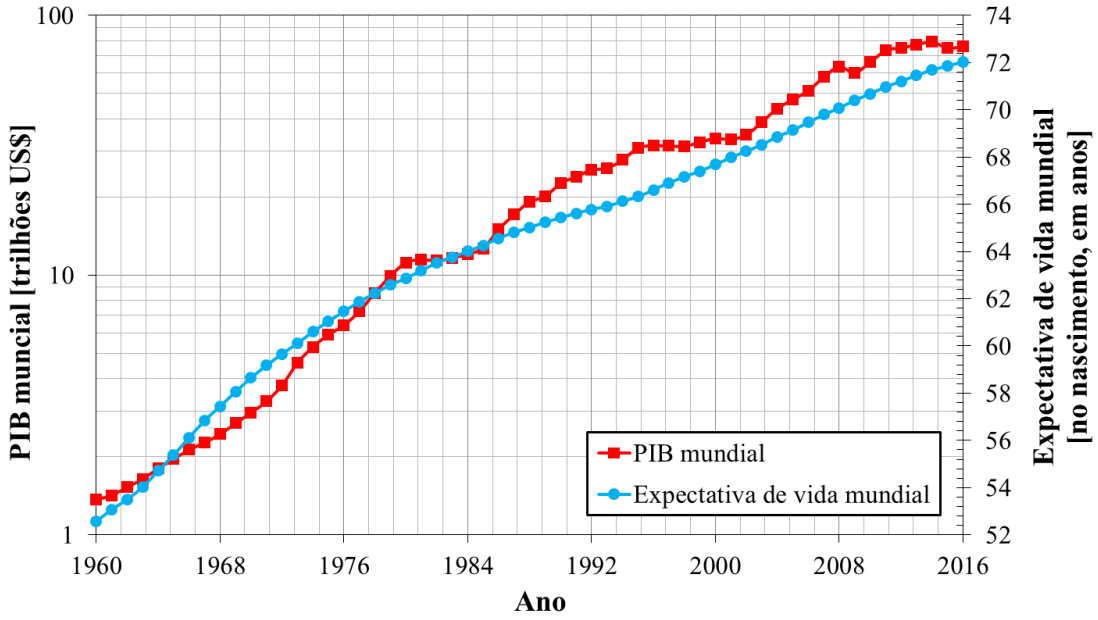

Figura 1.1 – PIB e expectativa de vida mundiais no período de 1960 a 2016 [dados: World Bank Group, 2018].

Este crescimento econômico e populacional também fez crescer a demanda por energia em todas as suas formas, tais como elétrica, mecânica, térmica etc. Segundo Conti et al., 2016, o consumo global de energia irá alcançar 239.000 TWh em 2040, um aumento de 48% em relação a 2012, como mostra a Figura 1.2.

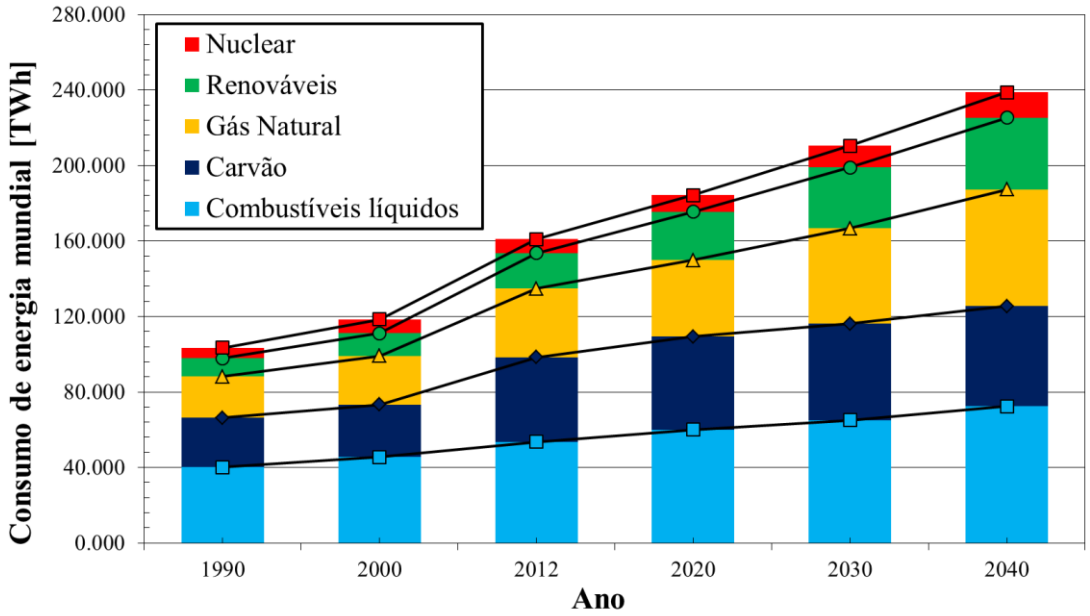

Figura 1.2 - Consumo mundial de energia por fonte geradora - histórico e projeções [dados: Conti et al., 2016].

Este crescimento ocorrerá para todos os tipos de combustíveis, até mesmo os considerados mais prejudiciais ao meio-ambiente, como os combustíveis fósseis e o carvão. Isso porque ainda é impraticável, por questões financeiras e tecnológicas, substituir completamente o sistema de geração tradicional pelas fontes renováveis.

Panorama energético brasileiro

Desde 2015, o Brasil vem passando por uma crise econômica, que culminou com recessão durante os anos de 2015 e 2016 e apresentou uma melhora tímida em 2017 e 2018. Este fraco desempenho econômico resultou na estagnação do consumo de eletricidade do país no período 2015-2016 [EPE, 2017], pois diminuiu a produção industrial e o consumo da população. Porém, com a retomada da atividade econômica, as projeções para o consumo de energia elétrica e PIB nacionais mostram crescimento significativo para os próximos anos, conforme a figura abaixo.

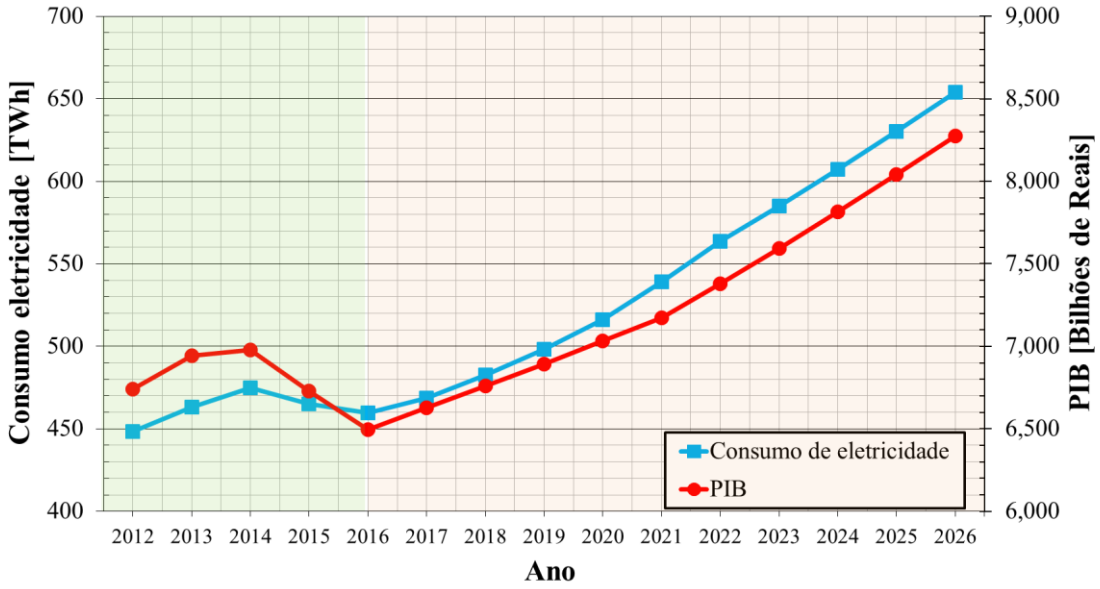

Figura 1.3 – Consumo de energia elétrica e PIB do Brasil consolidado (2012-2016) e projeções para o período de 2017 a 2026 [dados: EPE, 2017 e Banco Central do Brasil].

Para suprir esta crescente demanda por energia deve-se aumentar tanto a geração quanto melhorar a eficiência nos sistemas de geração, distribuição, consumo e comercialização de energia. Além do desafio de suprir esta demanda, existe ainda a questão dos impactos ambientais destes projetos. Uma alternativa para aumentar a geração e minimizar os impactos ambientais é a integração de fontes de energias renováveis á matriz energética.

Integração de fontes renováveis

Uma das barreiras que impedem uma maior participação das fontes renováveis na matriz energética é a sua intermitência: fontes solares só operam durante os períodos diurnos e com céu limpo, enquanto as fontes eólicas quando há correntes de vento. Esta característica torna estes sistemas pouco flexíveis, dificultando a sua incorporação á matriz energética.

Weitemeyer et al., 2015, realizam um estudo sobre a capacidade de integração das fontes de energia renováveis solar e eólica na matriz energética e qual o benefício do acoplamento de sistemas de armazenamento de energia á estas fontes renováveis.

Neste estudo, somente as fontes solar e eólica foram consideradas e as fontes não renováveis eram completamente flexíveis. A média da demanda energética da Alemanha no período de 2000 a 2007 foi adotada como base. Definiu-se a Função de Integração de

Renováveis FIR, que indica a participação na demanda abastecida pelas fontes renováveis e o fator de geração de potência de energia renovável médio γ, que representa a eletricidade total gerada pelas fontes renováveis. Quando a FIR é igual ao γ, significa que toda a energia gerada palas fontes renováveis está sendo utilizada. Quando a FIR é menor que γ, significa que existem períodos em que a geração das fontes renováveis é maior que a demanda e este excesso é desperdiçado.

No melhor cenário avaliado, no qual 60% da matriz renovável é eólica e 40% solar, a FIR e o γ se igualam até o valor de 0,5 (símbolos circulares), conforme mostra a Figura 1.4. Se as fontes renováveis fossem perfeitamente integradas e flexíveis, este valor seria igual a 1 (linha tracejada).

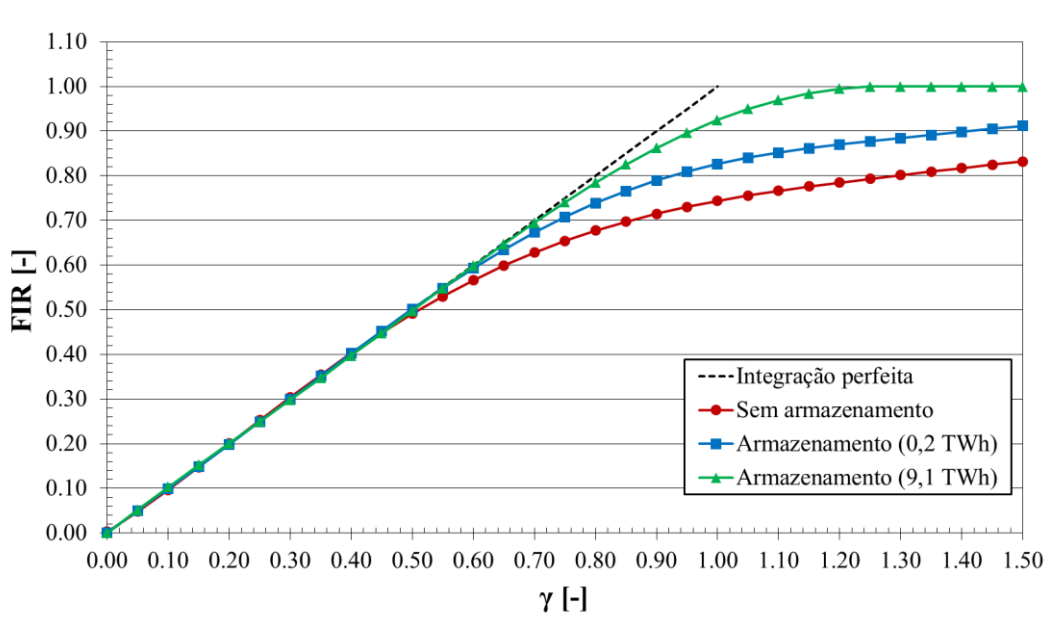

Figura 1.4 – Relação entre FIR e γ para diferentes capacidades de armazenamento acopladas à matriz energética [dados: Weitemeyer et al., 2015].

Porém, a partir deste ponto ocorre subutilização das fontes renováveis e, para suprir totalmente a demanda com fontes renováveis, seria necessário aumentar de forma significativa a capacidade de geração renovável instalada. Porém, foi constatado que a utilização de um sistema de acumulação de energia ameniza estes efeitos.

Foi observado que um sistema de armazenamento de apenas 0,2 TWh (a demanda energética média da Alemanha no período foi de 474,79 TWh) já melhora significativamente a relação FIR e γ. Com um sistema de armazenamento de 9,1 TWh, pode-se atingir uma FIR igual a 1 com γ igual a 1,2. Observa-se que 9,1 TWh representa menos de 2% da demanda

energética média da Alemanha no período, ou seja, um sistema de armazenamento bem dimensionado, mesmo pequeno, é capaz de melhorar significativamente a integração das fontes renováveis.

Existem diferentes sistemas de acumulação de energia, que podem se caracterizados de acordo com o princípio de armazenamento, conforme a Figura 1.5.

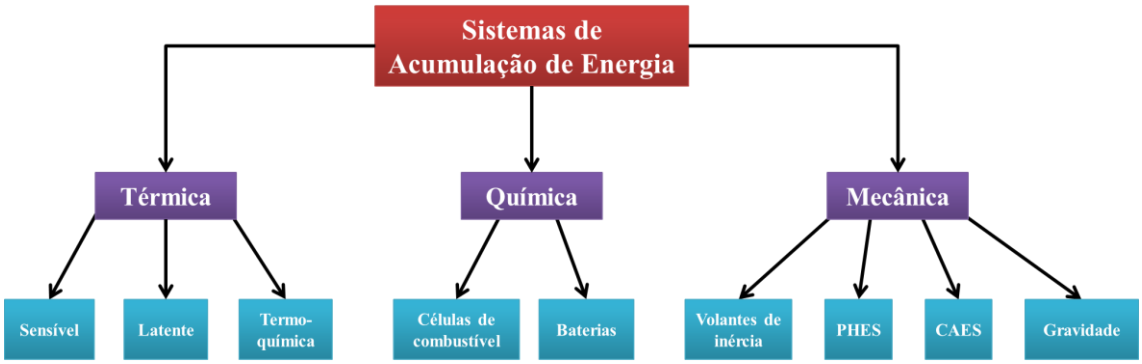

Figura 1.5 - Classificação dos tipos de sistemas de armazenamento de energia de acordo com o princípio de funcionamento.

Cada um destes sistemas possuem diferentes características, como capacidade de armazenamento, potência, custos de capital, manutenção, operação, etc. A Figura 1.6 mostra uma comparação dos custos de capital para diferentes sistemas de acumulação de energia.

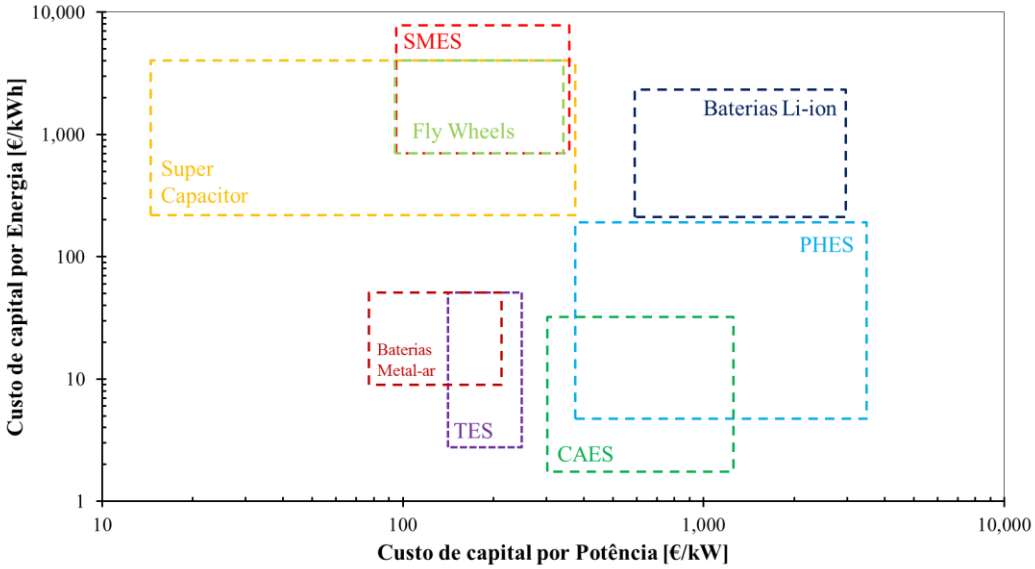

Figura 1.6 – Custos de capital por potência e energia armazenada para diferentes tipos de sistemas de acumulação [adaptado de Hameer e Niekerk, 2015].

Observa-se que os sistemas de armazenamento de calor (*Thermal Energy Storage* TES) são os únicos financeiramente competitivos com as Baterias de metal-ar, com a vantagem de serem menos prejudiciais ao meio ambiente.

Sabe-se que além dos custos de capital, existem outros fatores que devem ser reconsiderados, tais como custos de operação e manutenção, segurança na operação, ciclo de vida, etc. Portanto, assim como observado por Suberu et al., 2014, a viabilidade dos sistemas de acumulação de energia depende de diversos fatores, não existindo um único sistema de acumulação ideal, que atenderá todas as condições de demanda, geográficas e fontes de energia.

1.1 Motivação

Percebeu-se que os sistemas de acumulação de calor possuem a vantagem de serem menos nocivos ao meio ambiente e mais baratos que suas contrapartes (Figura 6) e capazes de auxiliar na incorporação das fontes de energia renováveis à matriz energética [Weitemeyer et al., 2015]. Além destas características, eles ainda possuem uma ampla faixa de aplicação, desde baixas temperaturas (20-100°C para secagem de alimentos) até temperaturas de 1.000°C para sistemas de geração de energia [Ayyappan et al., 2016, Hameer e Niekerk, 2015]. Todas estas qualidades tornam importante o estudo deste tipo de sistema na área de acumulação de energia.

O primeiro contato com o estudo e implementação de sistemas de acumulação de calor originou-se da construção de um secador solar experimental para ervas, maçãs, tomates, etc., na fazenda de educação ambiental Quinta da Estância[1], em Viamão, RS, conforme mostrado na Figura 1.7.

[1] http://www.quintadaestancia.com.br/

Figura 1.7 - Secador solar construído na Quinta da Estância.

Secadores solares empregam a energia proveniente do Sol para aquecer o ar exterior e reduzir sua umidade relativa, para posteriormente realizar a secagem dos produtos vegetais. A energia solar captada durante o dia necessita de um leito de armazenamento para evitar que os alimentos voltem a absorver unidade durante a noite. Paralelamente, a temperatura do ar aquecido pode variar sensivelmente ao longo do período diurno, justificando ainda mais o emprego de um material de acumulação de calor. No caso do secador construído na Quinta da Estância, a acumulação foi construída com um leito de pedras, por ser um material disponível no local.

As medições da temperatura do ar em diferentes pontos do secador mostraram que o leito de pedras foi pouco eficiente, pois a energia térmica acumulada foi descarregada em períodos muito curtos, ocasionando a interrupção do processo de secagem (Figura 1.8).

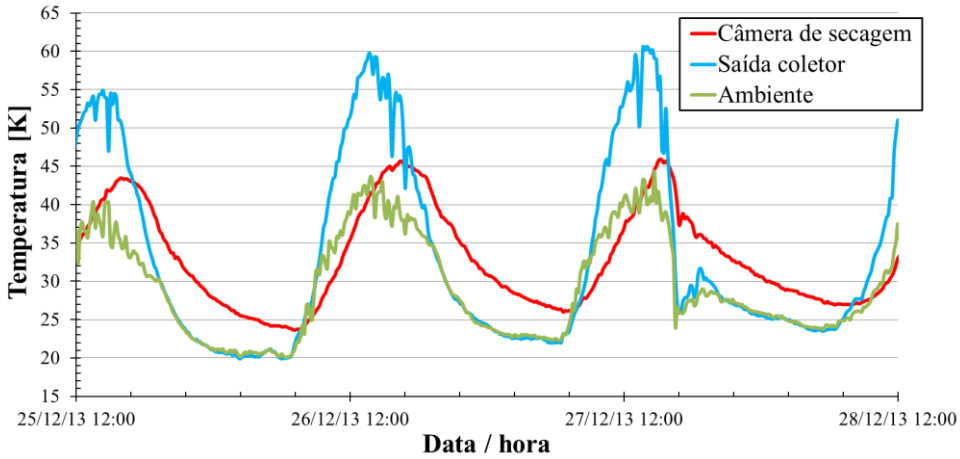

Figura 1.8 – Medições das temperaturas na saída do coletor, ambiente e na câmera de secagem do secador solar construído na Quinta da Estância, durante três dias de Dezembro de 2013.

Com base na constatação da ineficiência da acumulação no secador solar construído, nas vantagens inerentes da acumulação de calor, na sua importância para a integração das fontes renováveis e sua ampla faixa de aplicação, iniciaram-se estudos sobre modelagem, dimensionamento e otimização de sistemas de acumulação de calor sensível. O primeiro trabalho elaborado sobre o assunto foi sua Dissertação de Mestrado, intitulada "Otimização de estruturas para acumulação de calor sensível" [Andriotty, 2014]. O objetivo desta dissertação consistiu em obter a configuração mais adequada de um sistema de acumulação de placas planas paralelas, submetido a uma fonte de calor intermitente, para minimizar as variações da temperatura do ar na saída do sistema.

1.2 Revisão Bibliográfica

Reconhecendo a importância dos sistemas de armazenamento de calor, esta revisão bibliográfica explora diversas aplicações que utilizam estes sistemas. Existem duas principais características que devem ser avaliadas em sistemas de acumulação de calor: o material de acumulação (Heat Storage Material HSM) e a finalidade do sistema.

Com relação ao HSM, Hasnain, 1998a, Hasnain, 1998b, Bal et al., 2010 e Cabeza et al., 2011 fizeram revisões de materiais utilizados em termo-acumulação, ressaltando vantagens e desvantagens de vários deles, bem como suas propriedades químicas e termo-físicas. Estes trabalhos classificaram os materiais de termo-acumulação segundo a operação em regime sensível ou latente. Segundo estes autores, os materiais de termo-acumulação devem ser quimicamente estáveis, possuirem alta condutividade térmica, não serem tóxicos ou corrosivos e possuirem elevada capacidade de armazenamento, definida pelo produto da massa específica e calor específico. Para os materiais com troca de fase é desejável que possuam elevado calor latente e baixa variação de volume quando ocorre mudança de fase.

Com relação às áreas de aplicação, escalas e dimensionamento dos sistemas de acumulação de calor, foi realizada uma revisão bibliométrica de trabalhos publicados no período de 2012 a 2018, resumidos na Tabela 1.1.

Tabela 1.1 - Resultados da pesquisa bibliográfica sobre sistemas de acumulação de calor sensível realizada no período de 2012 a 2018.

Título	**Autores**	**Periódico**	**Ano**
Low temperature desalination using solar collectors augmented by thermal energy storage	Gude, V. G.; Nirmalakhandan, N.; Deng, S.; Maganti, A.	Applied Energy	2012
Numerical investigation of free-cooling system using plate type PCM storage	Darzi, A. R.; Moosania, S. M.; Tan, F. L.; Farhadi, M.	International Communications in Heat and Mass Transfer	2013
Stabilization of the outflow temperature of a packed-bed thermal energy storage by combining rocks with phase change materials	Zanganeh, G.; Commerford, M.; Haselbacher, A.; Pedretti, A.; Steinfeld, A	Applied thermal engineering	2014
Overview of direct air free cooling and thermal energy storage potential energy savings in data centres	Oró, E.; Depoorter, V.; Pflugradt, N.; Salom, J.	Applied thermal engineering	2015
Thermal analysis and design of solid energy storage systems using a modified lumped capacitance method	Jian, Y.; Bai, F.; Falcoz, Q.	Applied Thermal Engineering	2015
Industrial waste heat recovery using an enhanced conductivity latent heat thermal energy storage	Merlin, K.; Soto, J.; Delaunay, D.; Traonvouez, L.	Applied energy	2016
Performance improvement studies in a solar greenhouse drier using sensible heat storage materials	Ayyappan, S.; Mayilsamy, K.; Sreenarayanan, V. V.	Heat and Mass Transfer	2016
Levelised cost of storage for pumped heat energy storage in comparison with other energy storage technologies	Smallbone, A.; Jülch, V.; Wardle, R.; Roskilly, A. P.	Energy Conversion and Management	2017
Thermal energy storage systems for concentrated solar power plants	Pelay, U.; Luo, L.; Fan, Y.; Stitou, D.; Rood, M.	Renewable and Sustainable Energy Reviews	2017
Borehole thermal energy storage systems under the influence of groundwater flow and time-varying surface temperature	Nguyen, A.; Pasquier, P.; Marcotte, D.	Geothermics	2017
Study of cycle-to-cycle dynamic characteristics of adiabatic Compressed Air Energy Storage using packed bed Thermal Energy Storage	He, W.; Wang, J.; Wang, Y.; Ding, Y.; Chen, H.; Wu, Y.; Garvey, S.	Energy	2017
Performance evaluation of large scale rock-pit seasonal thermal energy storage for application in underground mine ventilation	Ghoreishi-Madiseh, S. A.; Sasmito, A. P.; Hassani, F. P.; Amiri, L.	Applied Energy	2017
Techno-economic analysis of a hybrid PV-CSP system with thermal energy storage applied to isolated microgrids	Aguilar-Jiménez, J. A.; Velázquez, N.; Acuña, A.	Solar Energy	2018

Uma das áreas de aplicação da acumulação de calor é a eficiência energética de ambientes e edificações. Neste sentido, Darzi et al., 2013, avaliaram a utilização de materiais de troca de fase (*Phase Change materials* PCM) com a função de auxiliar no condicionamento de ambientes em edificações. O sistema foi projetado para "armazenar frio" durante a noite e utilizá-lo durante o dia, diminuindo o uso do ar-condicionado. Foi observado que a eficiência do sistema permaneceu estável para curtos períodos de operação, porém decresceu rapidamente para períodos mais longos.

Nguyen et al., 2017, estudaram os efeitos do escoamento subterrâneo de água em sistemas de acumulação de calor subterrâneos, denominados *Borehole Thernal Energy Storage* BTES. Este tipo de sistema consiste em fazer escoar um fluido de trabalho por tubos enterrados no solo. A massa do solo é o próprio material de acumulação, que funciona como um acumulador de calor sazonal: no verão, utiliza-se o "frio" armazenado no solo e no inverno o calor. Os resultados mostraram que o escoamento de água subterrâneo reduziu significativamente a eficiência dos sistemas BTES.

Ainda sobre as vantagens do BTES, Lanahan e Tabares-Velasco, 2017, afirmam que estes sistemas podem auxiliar muito na redução do consumo das edificações e são mais flexíveis que outros sistemas de acumulação sazonal, tais como tanques de água ou aquíferos.

Oró et al., 2015, avaliaram a viabilidade econômica na combinação de "*free cooling*" com acumulação de calor em *Data Centers*. Um *Data Center* com 1.250 kW de potência foi utilizado como referência e avaliado com os dados climáticos de cinco cidades europeias: Amsterdam, Barcelona, Frankfurt, Londres e Estocolmo. Dois sistemas de acumulação de calor foram propostos, um sensível (água) e outro com PCM (sal hidratado S13). Os autores concluíram que o acoplamento de um sistema de acumulação de calor foi mais vantajoso nas regiões que possuíam grandes diferenças diárias nos custos de eletricidade, como foi o caso de Barcelona, Espanha, que apresentou redução de 51% no custo em eletricidade.

Ghoreishi-Madiseh et al., 2017, avaliaram a viabilidade econômica da utilização de rochas para o condicionamento térmico no interior de minas profundas. O sistema funcionou como um retificador térmico sazonal, armazenando calor no verão e utilizando-o para aquecimento no inverno, modelado utilizando a teoria dos volumes médios para meios porosos. A mina de Creighton, Canada, foi escolhida para a análise da viabilidade econômica, para um período de 10 anos. A utilização do sistema de acumulação gerou uma economia

estimada de US$ 437.000 por ano e redução de 8.862 toneladas de emissão de carbono pela não utilização do sistema de aquecimento/refrigeração.

Processos de dessalinização de água também são passíveis de acoplamento a sistemas de acumulação de calor. Gude et al., 2012, propuseram um processo de dessalinização de água para baixas temperaturas (40-50°C) utilizando coletores solares de placas planas e armazenamento de calor sensível. Água foi utilizada como HSM e o processo de dessalinização foi modelado através de uma formulação semi-analítica. Os autores avaliaram o desempenho do sistema de dessalinização para um período de três semanas, em duas situações: uma com todos os dias de céu limpo (sem nuvens) e outro com um dia nublado por semana. A taxa de produção de água doce foi reduzida em mais de 50% para o sistema sem acumulação na situação nublada em relação à de céu limpo. Porém, a redução com o acoplamento de um sistema de acumulação de 1 m³ de HSM foi de 8% e para 3 m³ foi de aproximadamente 5%.

Além do tratamento de água, energia solar também é utilizada em secadores e usinas concentradoras solares (*Concentrated Solar Power* CSP). Ayyappan et al., 2016, realizaram um experimento para avaliar o emprego do armazenamento de calor sensível em secadores solares de estufas. O chão da estufa foi construído com os materiais de acumulação analisados (concreto, areia e pedras). O tempo necessário para a redução do conteúdo de umidade de cocos, de 52% para 7%, utilizando concreto, areia ou pedras foi de 78 h, 66 h e 53 h, respectivamente. Se os cocos fossem secados ao ar livre, o tempo de secagem seria de 174 h. Ainda, a acumulação térmica aumentou a temperatura no interior da estufa durante a noite em 3°C, 3,5°C e 6°C ao utilizar-se concreto, areia ou pedras, respectivamente.

Zanganeh et al., 2014, propuseram uma sistema de armazenamento em leitos de esferas combinando acumulação de calor sensível e latente para CSP. O conceito proposto consiste em posicionar uma pequena quantidade de PCM na saída do sistema de acumulação, estabilizando a temperatura do fluido próxima a temperatura de troca de fase do PCM. Foi utilizado um modelo unidimensional transiente para modelar as equações de conservação de energia para os meios sólido e fluido. O sistema de acumulação foi submetido a uma condição de operação cíclica, com a mesma duração dos períodos de carga e descarga (5 h). A análise do sistema deu-se a partir do nono ciclo, quando foi alcançada a estabilização do regime transiente. O ar foi escolhido como fluido de trabalho e pedras como material de acumulação sensível, além de três diferentes PCM. O volume de PCM necessário para estabilizar a temperatura do ar na saída do sistema de acumulação foi de apenas 1,33% do volume total

ocupado pelo sistema de acumulação. Isso representou 4,4% da energia total armazenada no sistema devido ao PCM, sendo o restante acumulado na forma de calor sensível.

Jian et al., 2015, modelaram um sistema de acumulação de calor para CSP através da aplicação de transformadas de Laplace ao modelo *Lumped* tradicional, não sendo necessária uma solução numérica. Um módulo de concreto foi construído, sendo água o fluido de trabalho, e utilizado para verificar a precisão do modelo proposto. Segundo os autores, os resultados entre o experimento e o modelo *Lumped* modificado foram satisfatórios. Ao final, os autores apresentaram uma metodologia de otimização do T3S com o objetivo de reduzir o custo do sistema, composto pelos custos do material de acumulação e dos tubos para o escoamento do fluido. As restrições da otimização foram a quantidade de calor armazenada e a temperatura de saída do fluido do sistema de acumulação.

Pelay et al., 2017, revisaram de diferentes sistemas de acumulação de calor acoplados a plantas CSP. Segundo os autores, a tecnologia de usinas CSP é considerada madura, desenvolvida e disponível para o mercado. Pela sua característica de intermitência, o acoplamento de um sistema de acumulação de calor é essencial para a viabilidade econômica das CSP. A revisão dos autores identificou que o armazenamento de calor sensível é a forma mais empregada nas CSP, devido ao baixo custo, fácil implementação e confiabilidade do sistema.

Aguilar-Jiménez et al., 2018, estudaram a viabilidade econômica da substituição do atual sistema de fornecimento de eletricidade de pequeno porte da comunidade isolada de Puertecitos, Baja California, Mexico. O sistema de eletricidade atual desta comunidade consiste em painéis fotovoltaicos PV acoplados a um banco de baterias de ions de lítio. A alteração proposta foi um sistema híbrido de placas fotovoltaicas (*PhotoVoltaic* PV) e uma planta CSP. Durante o dia, as placas PV forneceriam eletricidade para a comunidade enquanto a planta CSP utilizaria tanques de água para armazenar calor. Durante a noite ou em períodos nublados, a energia armazenada nos tanques de água seria utilizada em um ciclo orgânico de Rankine (*Organic Rankine Cycle* ORC) para fornecer eletricidade.

O sistema híbrido PV-CSP seria capaz de fornecer eletricidade a um custo 2% superior ao sistema atual. O CAPEX (*capital expenditure* ou custo de bens de capital) foi o fator mais crítico para o sistema híbrido, pois foi 2.3 vezes maior que o sistema com baterias. Porém, foi observado que se a capacidade do sistema híbrido PV-CSP fosse expandida e utilizada ao máximo, o custo da geração de energia elétrica poderia cair em aproximadamente 60%.

Um sistema de acumulação de calor também é uma alternativa para o reaproveitamento de calor industrial rejeitado (*waste industrial heat*). Merlin et al., 2016, estudaram um sistema de acumulação de calor latente, denominado de LHTES, aplicado a um processo industrial de esterilização de alimentos por bateladas. O processo de esterilização iniciou com o TES carregado, cuja função foi pré-aquecer a água de esterilização, sendo substituído por um boiler para as temperaturas mais elevadas. Depois da esterilização, o LHTES voltou a participar do processo, desta vez absorvendo calor para resfriar a água de esterilização. Um experimento utilizando um esterilizador comercial foi realizado e o material de acumulação foi a parafina RT82. Os resultados mostraram que foi possível poupar 15% da energia do processo de esterilização, com o período de Payback inferior a 500 dias para o mesmo sistema de acumulação, em maior escala.

Sistemas que armazenam energia em um fluido comprimido, geralmente ar, são passíveis de acoplamento com TES. Neste sentido, Smallbone et al., 2017, compararam os custos do sistema de armazenamento de calor bombeado PTES com outros TES, tais como PHS, hidrogênio, CAES e metano. O sistema PTES gera eletricidade através de uma bomba de calor reversível, comprimindo e expandindo o fluido de trabalho.

A análise financeira utilizou o modelo de custos *Levelised Cost of Storage*, que considera o CAPEX e os custos anuais de operação e manutenção durante o ciclo de vida do sistema, por unidade de energia descarregada pelo sistema. A análise indicou que o PTES é competitivo com o CAES e até com o PHS, possuindo a vantagem da flexibilização do local de instalação. Segundo os autores, o baixo custo de armazenamento do PTES indica que esta tecnologia pode ser viável para utilização em armazenamentos de longa duração, embora tenha sido projetada para curta duração.

He et al., 2017, estudaram o acoplamento de acumulação de calor a sistemas de armazenamento de ar comprimido CAES. A função do sistema TES foi absorver o calor rejeitado durante a compressão do ar e utiliza-lo posteriormente quando admitido na turbina para geração de eletricidade. Um leito de esferas foi utilizado como configuração do sistema de acumulação e dois materiais de acumulação foram avaliados: um latente ($NaNO_3$) e um sensível (pedras). O modelo matemático do sistema combinado CAES-TES foi validado com dados experimentais disponíveis na literatura e implementado nos softwares MATLAB/ SIMULINK. A eficiência do sistema combinado CAES-TES foi avaliada para a condição de operação cíclica permanente (quando não há mais variações entre os ciclos). Cada ciclo foi

definido por um período de carregamento, um período ocioso, um período de descarregamento e outro período ocioso.

A eficiência cíclica permanente foi de 56,5% para o material de acumulação $NaNO_3$ e de 53,2% quando utilizadas pedras. Também se verificou que a eficiência da turbina para o PCM foi de 80%, maior que quando utilizadas padras (76%). Segundo os autores, esta diferença deveu-se a maior estratificação da temperatura do sistema de acumulação com o $NaNO_3$.

Observou-se que, embora o estudo tenha sido iniciado em acumulação de calor sensível para secadores solares [Andriotty, 2014], ele também pode ser empregado para outras finalidades e escalas, tais como: eficiência energética de ambientes e edificações; gestão energética em *Data Centers*; condicionamento térmico no interior de minas profundas; dessalinização de água; usinas concentradoras solares (*Concentrated Solar Power* CSP); ciclos orgânicos de Rankine (*Organic Rankine Cycle* ORC); reaproveitamento de calor industrial rejeitado; em sistemas de armazenamento de ar comprimido CAES.

Através da análise da revisão bibliográfica, nos panoramas energéticos mundial e brasileiro, na importância da incorporação das fontes de energia renováveis e nas características dos T3S, três principais conclusões foram observadas:

- O estudo de sistemas de acumulação de calor sensível T3S ainda é uma área que pode ser explorada e desenvolvida. Embora a acumulação de calor sensível possua menor densidade de energia armazenada que a latente, a primeira possui algumas vantagens: baixo custo do HSM (Figura 1.6), sem problemas de inflamabilidade, sem histerese e sem mudança de fase, baixo impacto ambiental, incorporação a sistemas de geração mais direta e simples [Hasnain, 1998a; Flueckiger et al., 2013; Lefebvre e Tezel, 2017]. Portanto, a acumulação de calor sensível ainda tem vasto campo de aplicação e não será substituída tão rapidamente pelos PCM.

- Embora existam trabalhos aplicados sobre sistemas de acumulação de calor, as metodologias utilizadas para avaliar o desempenho do T3S fazem uso de modelos numéricos complexos [Ghoreishi-Madiseh et al., 2017] ou baseiam-se em tentativa e erro [Li et al., 2012 e Zanganeh et al., 2014] ou apenas avaliam uma determinada configuração do sistema [Gude et al., 2012 e He et al., 2017], sem a otimização do sistema. E mesmo os que fazem uso da otimização, necessitam que o processo de otimização seja repetido para outras condições de operação do sistema [Jian et al., 2015].

- Muitos sistemas operam em ciclos, com momentos de alta e baixa demanda e este comportamento pode ser interpretado como um processo de retificação.

Baseando-se nestas conclusões, a presente Tese tem por objetivo desenvolver uma metodologia de dimensionamento de sistemas de acumulação de calor sensível operando como retificadores térmicos. Esta metodologia de dimensionamento garante uma determinada capacidade de retificação com a menor massa de HSM possível, de forma simples e direta (sem tentativa e erro ou métodos numéricos complexos) e sem a necessidade de realizar um processo de otimização para cada configuração diferente do sistema.

1.3 Objetivos

Objetivo Geral

O objetivo principal desta Tese foi desenvolver uma metodologia de dimensionamento de sistemas acumulação de calor sensível T3S baseada em projeto inverso, visando obter uma saída condicionada do fluido de trabalho com a mínima massa de acumulação.

Objetivos específicos

- Analisar os desvios do modelo LEM utilizado para descrever o T3S retificador submetido a uma fonte de calor cíclica.
- Minimizar a massa de HSM e encontrar a sua distribuição mais adequada para garantir que a temperatura do fluido de trabalho na saída do T3S permaneça dentro da faixa de operação desejada.
- Desenvolver uma metodologia de dimensionamento para um T3S de placas planas operando como um retificador térmico que garante a capacidade de retificação projetada com a menor massa de HSM e verificar os desvios desta metodologia.

1.4 Estrutura do trabalho

A presente Tese está estruturada em três artigos, com os seguintes conteúdos:

O Capítulo 2 apresenta a análise dos desvios do modelo LEM utilizado para descrever o T3S retificador submetido a uma fonte de calor cíclica. Através da metodologia de

planejamento de experimentos Box-Behnken, 130 simulações em CFD foram realizadas (Apêndices A e B) e utilizadas para verificar quais as condições em que o LEM apresenta desvios significativos em relação a simulações mais detalhadas. A amplitude e o deslocamento de fase da temperatura do fluido na saída do T3S foram utilizados para verificar os desvios entre os resultados do LEM e CFD (Apêndice C).

O Capítulo 3 mostra a otimização para uma situação específica de um sistema de acumulação de placas planas, modelado pelo LEM, visando atender uma determinada retificação projetada (redução da amplitude de entrada de 30°C, para uma saída com amplitude de 4°C) com a menor massa de HSM. Os resultados foram publicados em um artigo que analisou diversas vazões mássicas de ar e verificou o comprimento e a distância entre as placas que atendiam a condição de retificação projetada.

O Capítulo 4 expande os resultados do Capítulo 3 e apresenta uma metodologia de dimensionamento para a otimização de um T3S de placas planas operando como um retificador térmico. Esta metodologia de dimensionamento garante a capacidade de retificação projetada, com a menor massa de HSM, alcançada pelas escolhas das propriedades do HSM e sua geometria.

O Capítulo 5 traz as conclusões da Tese e apresenta as propostas de continuidade da pesquisa na área de acumulação de calor.

2 ACCURATENESS OF LUMPED ELEMENT MODEL APPLIED TO SENSIBLE THERMAL ENERGY STORAGE SYSTEMS[2]

This chapter presents the mathematical formulation utilized to model the Sensible Thermal Energy Storage system T3S analyzed in this Thesis and verify its the accurateness. The T3S analyzed is meant to work as a thermal rectifier, continuously powered by a cyclical thermal stream in order to retrieve a conditioned output. The storage system is composed by a set of flat parallel plates, the Heat Storage Material HSM, separated by narrow channels, where an induced fluid stream carries the exchanged energy of the system. The T3S is modeled by a Lumped Element Model LEM, but its accurateness needed to be ascertained. CFD simulations are used to assess LEM deviations following a Design of Experiments planning, performed by the Box-Behnken method. Nine T3S controlled parameters are identified: distance between HSM plates, HSM plate thickness, HSM plate length, air mass flow rate, HSM thermal conductivity, HSM density and HSM specific heat, sinusoidal function period and function amplitude. The temporal evolution of the fluid temperature in the T3S discharge is used to observe the amplitude and phase deviations in respect to CFD modeling. Amplitude deviations are found to be below 6% and phase shift below 4% for 130 simulated cases assigned by the Box-Behnken method, with an exceptional situation of 89%. Heat conduction along the HSM axial direction is prevailing in respect to the transversal transfer, meaning that significant deviations from LEM to CFD only occur when T3S combines high NTU and HSM thermal conductivity values. The present study shows that thermal energy storage systems like the one proposed in this Thesis can be simulated with LEM, allowing to perform further optimization studies.

2.1 Introduction

Sensible Thermal Energy Storage system, called here as T3S, are used to stabilize intermittent energy sources, adapting them to continuous operating conditions. When applied to solar energy, the storage system is meant to deliver an attenuated output out of a cyclic input source.

---

[2] Autors: Tiago Haubert Andriotty[*], Paulo Smith Schneider, Letícia Jenisch Rodrigues

[*]tiago.haubert@ufrgs.br (corresponding author)

In a previous work by Andriotty et al., 2016, a T3S made of parallel solid plates with air as working fluid flowing through then was optimized in order to reach an output air flow rate within a stabilized temperature range. The optimization process demanded to perform an important number of simulations of the storage system, described by a Lumped Element Model LEM, based on mass and energy balances. The exhaustive search optimization algorithm performed more than 200 million calls of the lumped model, which justified its simplified approach in terms of computational running time demand, but its accuracy was still to be verified.

An early work from Schumann, 1929, describes a simulation scheme with two differential equations to calculate the temperatures of the working fluid and the storage media. The model neglected the axial heat conduction along the solid and the fluid thermal capacitance. Bessel functions were used to solve the differential system and results were presented in graphs.

Schmidt and Szego, 1976, and Schmidt et al., 1977, modeled the working fluid as a transient 1D capacitive flow and the solid media as a transient 2D storage material. Results were presented in diagrams oriented to system design by selecting material thickness and length, plate distance, operational fluid temperatures and heat storage.

Naveira et al., 2009 proposed an analytical-numerical model to solve the transient laminar convection within the system channels with the Generalized Integral Transform Technique GITT. They found that the temperature along the aluminum interface was kept mostly constant due to the plate high thermal diffusivity.

Campo and Herranz, 2009, proposed a simple composite lumped model of the unidirectional heat conduction equation capable to predict the entire range of the dimensionless Bi number. Their model allowed evaluating all dimensionless times with good accurateness.

Souraki et al., 2014, investigated the effects of the Biot number and solid internal heat generation over the accurateness of various lumped models. Authors found improvements to the classical lumped model with the use of Hermite and polynomial approximations, which gave an extended precision to the approach.

Salomoni et al., 2014, modeled a concrete/water T3S by applying a finite element method for the solid media and a 1D energy balance with convection heat transfer correlations for the fluid. Two approaches for the fluid modeling were compared, one with a single control volume called quasi-steady and the other composed by several individual control volumes,

called non-steady. Both displayed similar results for system length up to 10m, when the non-steady became more accurate, although more time consuming.

Jian et al., 2015, worked on the cost optimization of a concrete/liquid T3S, and found out that bigger scale systems demanded more energy proportionally to smaller ones, and suggested the use of small connected modules.

Wang et al., 2016, performed T3S numerical simulations and results to the ones from lumped models with constant heat transfer coefficients, and identified that the use of constant coefficients for initial times up to 1s lead to important deviations. Another CFD to simplified models comparison was made by Jiang et al., 2018, with the use of superposition techniques within linear conditions. Their conclusions pointed out to good agreements of results followed by a sensible computing time reduction.

Sensible heat storage modeling can be found in literature, but little information is given about their accurateness and limitations. The goal of the present work was then to assess Lumped Element Model deviation in respect to more detailed results from CFD simulations of a T3S. A lumped model was used to describe a T3S composed by parallel plates and with air as the working fluid and simulated by a commercial CFD code, and comparisons followed a Design of Experiment planning.

2.2 System description

The Sensible Thermal Energy Storage system T3S proposed in the present study was meant to work as a thermal rectifier, continuously powered by a cyclical thermal flow stream in order to retrieve a conditioned output, as presented in Figure 2.1.

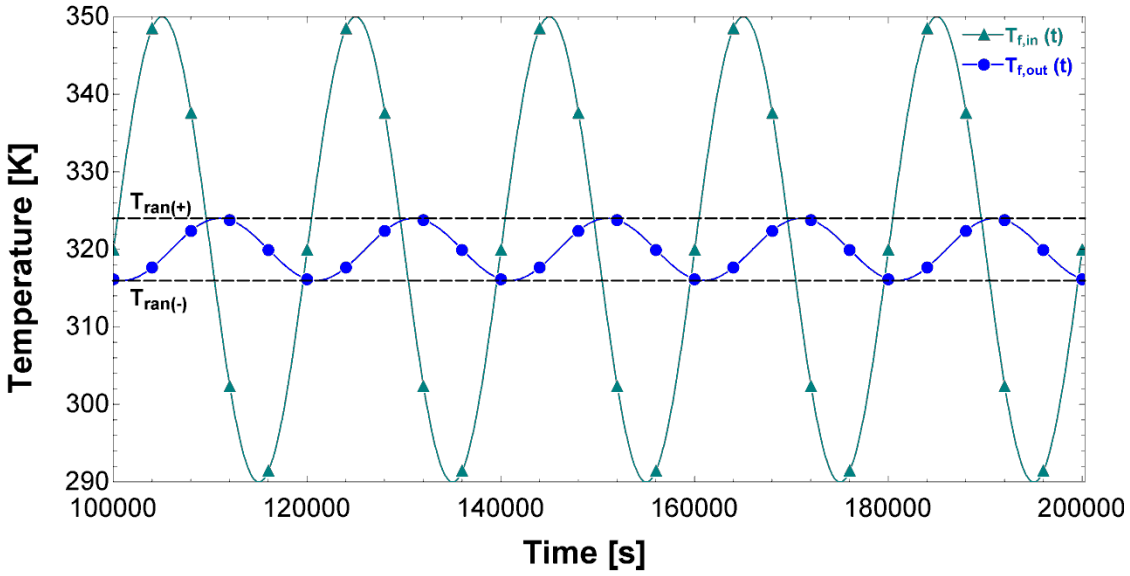

Figure 2.1 - Outlet fluid flow temperature (dot labeled curve) conditioned by the Sensible Thermal Energy Storage system T3S submitted to a cyclic inlet flow (triangular labeled curve) [Andriotty et al., 2016].

The T3S system chosen to be evaluated in the present study is depicted in Figure 2.2, composed by a set of flat parallel plates, the Heat Storage Material HSM, separated by narrow empty spaces, called hereby as channels, where an induced fluid stream carries the exchanged energy of the system.

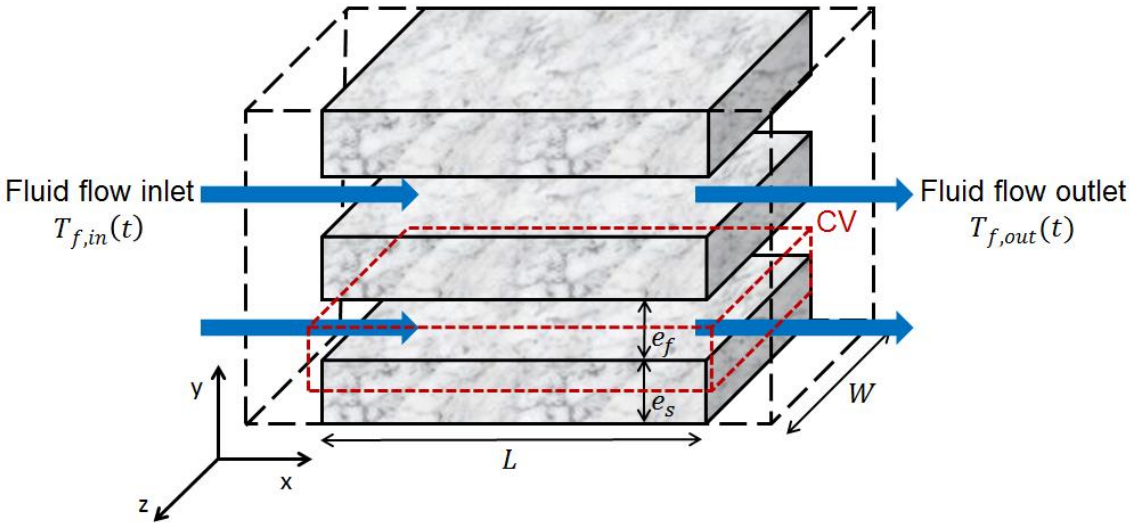

Figure 2.2 – Schematic scheme of the Sensible Thermal Energy Storage System T3S.

The HSM dynamic response was modeled by an energy conservation equation (Equation 2.1), and the fluid flow by a set of mass, force and energy conservation equations (Equations 2.2-2.4), written for an incompressible flow, with constant and uniform properties, without viscous dissipation and heat sources.

$$\rho_s c_{p,s} \frac{\partial T_s}{\partial t} = k_s \nabla^2 T_s \tag{2.1}$$

$$\nabla \cdot \boldsymbol{u}_f = 0 \tag{2.2}$$

$$\rho_f (\boldsymbol{u}_f \cdot \nabla) \boldsymbol{u}_f = -\nabla p_f + \mu_f (\nabla^2 \boldsymbol{u}_f) \tag{2.3}$$

$$\rho_f c_{p,f} \frac{\partial T}{\partial t} + \rho_f c_{p,f} \boldsymbol{u}_f \cdot \nabla T_f = k_f \nabla^2 T_f \tag{2.4}$$

Boundary and initial conditions for the control volume highlighted in red dashed lines in Figure 2.2 represent a 2D region, with half flat plate $e_s/2$ and half channel $e_f/2$ height, length L and unitary width W are presented as follows. The velocity profile for the inlet mass flow rate $\dot{m}_{inlet}$ was considered uniform and constant.

$$\frac{dq(0,0 \le y \le \frac{e_s}{2}, t>0)}{dx} = 0 \tag{2.5a}$$

$$\frac{dq(L,0 \le y \le \frac{e_s}{2}, t>0)}{dx} = 0 \tag{2.5b}$$

$$\frac{dq(0 \le x \le L,0,t>0)}{dy} = 0 \tag{2.5c}$$

$$\frac{dq(0 \le x \le L, \frac{e_s}{2}+\frac{e_f}{2}, t>0)}{dy} = 0 \tag{2.5d}$$

$$\frac{du(0 \le x \le L, \frac{e_s}{2}+\frac{e_f}{2}, t>0)}{dy} = 0 \tag{2.5e}$$

$$T_f\left(0, \frac{e_s}{2} < y \leq \frac{e_s}{2} + \frac{e_f}{2}, t > 0\right) = T_{inlet}(t) \tag{2.6a}$$

$$\dot{m}(0, \frac{e_s}{2} < y \leq \frac{e_s}{2} + \frac{e_f}{2}, t > 0) = \dot{m}_{inlet} \tag{2.6b}$$

$$P_f(L, \frac{e_s}{2} < \mathrm{y} \leq \frac{e_s}{2} + \frac{e_f}{2}, t > 0) = P_0 = 0 \tag{2.6c}$$

Initial conditions

$$T_s(0 < x \leq L, 0 \leq \mathrm{y} \leq \frac{e_s}{2}, t = 0) = T_{s,i} = T_{inlet}(t = 0) \tag{2.7a}$$

$$T_f\left(0 < x \leq L, \frac{e_s}{2} < y \leq \frac{e_s}{2} + \frac{e_f}{2}, t = 0\right) = T_{f,inlet}(t = 0) \tag{2.7b}$$

2.3 The Lumped Element Model - LEM

Lumped models are based on the simplification of spatially distributed physical parameters into a topology consisting of a certain number of components, without losing the major system characteristics, as stated by Yuan et al., 2015. This approach is useful whenever a simple and quick solution is searched to solve a much difficult and time-consuming problem, even if it can lead to a probable loss of quality information and accuracy. The original storage system T3S can be reduced to a smaller part of it, which correspond to the domain highlighted in Figure 2.2, and depicted in Figure 2.3.

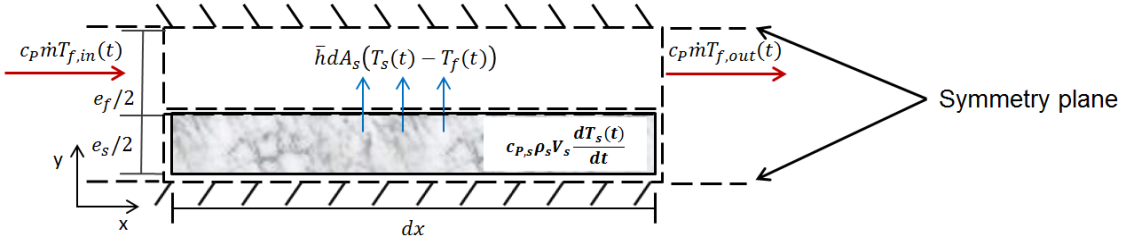

Figure 2.3 – Symmetric 2D view of the T3S control volume highlighted on Figure 2.2.

The energy balance proposed to that new symmetric 2D domain was written for both solid and fluid control volumes in order to calculate the output fluid temperature $T_{f,out}(t)$, as follows.

$$\rho_s \, c_{p,s} \, V_s \frac{dT_s(t)}{dt} = -\bar{h} \, dA_s (T_s(t) - T_f(t)) \tag{2.8}$$

$$\rho_f \, c_{p,f} \, V_f \frac{dT_{f,x}(t)}{dt} = \dot{m} \, c_{p,f} \, T_{f,in}(t) - \dot{m} \, c_{p,f} T_{f,out}(t) + \bar{h} \, dA_s \big(T_s(t) - T_f(t)\big) \tag{2.9}$$

with input fluid temperature $T_{f,in}$ defined as:

$$T_{f,in}(t) = T_{f,in(-)} + \left[1 + sen\left(\frac{\pi t}{\beta/2}\right)\right] \left([T_{f,in(+)} - T_{f,in(-)}]/2\right) \text{ for } x = 0, \frac{e_s}{2} < y \leq \frac{e_s}{2} + \frac{e_f}{2} \tag{2.10}$$

with $T_{f,in(+)}$ and $T_{f,in(-)}$ the function upper and lower limits and β its cycle period.

Fluid was modeled as non-capacitive in Equation 2.9, as its heat capacity is many times smaller than the one from HSM, but its temperature $T_f(t)$ was continuously updated with the one on the interface of the HSM. The new system was solved for the fluid output temperature $T_{f,out}(t)$ by applying the separation of variables technique, as presented in Andriotty et al., 2015, given by the following system:

$$T_s(t) = T_{s,i} - \left[1 - exp\left(-\frac{\bar{h} A_s}{c_{p,s} \rho_s V_s} t\right)\right] \left(T_{s,i} - T_f(t)\right) \tag{2.11}$$

$$T_{f,out}(t) = T_s(t) - \left[exp\left(-\frac{\bar{h} A_s}{\dot{m} c_{p,f}}\right) \left(T_s(t) - T_{f,in}(t)\right)\right] \tag{2.12}$$

with $T_{s,i}$ the HSM temperature initial value.

The T3S lumped model (Equations 2.11-2.12) is valid along its length *L*, but it was divided in *n* independent volume of length *L/n* (Figure 2.4) with the sake of keeping the model accuracy [Sragovich, 1989; Mawire et al., 2009; Maithani et al., 2013; Duffie and Beckman, 2013; Singh et al., 2009; Mumma and Marvin, 1976 *apud* Singh et al., 2009].

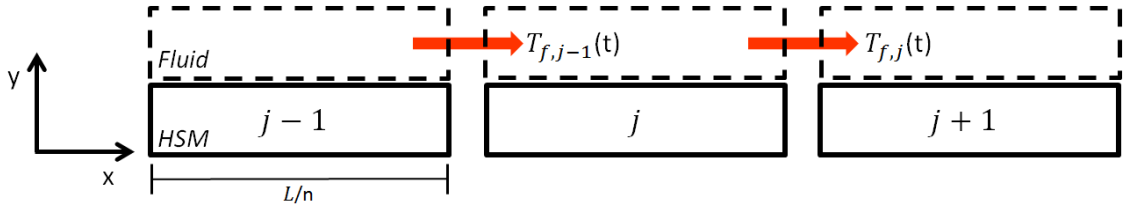

Figure 2.4 – Section scheme with 3 independent and insulated plates.

In and out fluid flow temperatures T_f couple the energy transfer along the model, whereas the solid material boundaries not connected to fluid interfaces are insulated. System Equations 2.11 and 2.12 were rewritten for a generic j section as a function of time, as follows:

$$T_{s,j}(t) = T_{s,j}(t-\Delta t) - \left[1 - exp\left(-\frac{\bar{h}_j A_{s,j}}{c_{p,s}\,\rho_s\,V_{s,j}}\Delta t\right)\right]\left(T_{s,j}(t-\Delta t) - \overline{T}_{f,j}(t)\right) \tag{2.13}$$

$$T_{f,j}(t) = T_{s,j}(t) - \left[exp\left(-\frac{\bar{h}_j(A_{s,j})}{\dot{m}\,c_{p,f}}\right)\left(T_{s,j}(t) - T_{f,j-1}(t)\right)\right] \tag{2.14}$$

The average fluid temperature $\overline{T}_{f,j}(t)$, was defined as the average value between the sections j and j -1, as follow

$$\overline{T}_{f,j}(t) = \frac{T_{f,j-1}(t) + T_{f,j}(t)}{2} \tag{2.15}$$

The average heat transfer coefficient $\bar{h}_j$ for a given section j can be calculated after the average laminar flow Nusselt correlation $\overline{Nu}_{D_h}$ from Stephan, 1959 *apud* Bejan, 2013, for infinite parallel flat plates

$$\overline{Nu}_{D_h,j} = \left(\frac{\bar{h}\,D_h}{k_f}\right)_j = 7.55 + \frac{0.024 L_*^{-1.14}}{1+0.0358 Pr_f^{0.17} L_*^{-0.64}} \qquad 0.1 \leq Pr_f \leq 1000 \tag{2.16}$$

with the hydraulic diameter D_h, the dimensionless length L_* at the thermal entry region and the Reynolds number Re_{D_h} defined by:

$$L_* = \frac{L}{D_h Re_{D_h} Pr_f}, \qquad \text{with} \quad D_h = 2e_f \text{ and } Re_{D_h} = \frac{\rho_f u_f D_h}{\mu_f} \tag{2.17}$$

The set of Equations 2.13 to 2.17 was named hereby as the Lumped Element Model LEM, as proposed by Yuan et al., 2015, to be solved for each of the T3S sections.

It is worth noticing that Hughes, 1975, modeled sensible thermal storage systems with the ε-NTU approach. HSM temperature behavior was taken as linear for each time step, whereas LEM method applied in the present chapter assumed it to behave exponentially, like classic lumped models [Çengel, 2011; Bergman et al., 2011].

It is common to look at the Biot number as a metric to assess lumped model accuracy, based on the assumption of uniform temperature along the system interface, and furthermore that heat diffusion gradients are unimportant within the solid medium. The Biot number cannot be used to assess the present T3S because the fluid temperature varies along the axial direction, leading to a not uniform heat conduction field within the solid medium.

2.3.1 LEM implementation

Air properties were kept at constant values, displayed in Table 2.1.

Table 2.1 - Air thermophysic properties @ 320K [Bergman et al., 2011].

Air properties at 320 K				
Density ρ [kg/m³]	Specific heat c_p [J/(kgK)]	Dynamic viscosity μ [kg/(ms)]	Prandtl number Pr [-]	Thermal conductivity k [W/(mK)]
1.103	1,008	1.949 E-5	0.705	2.785 E-2

The assumption of laminar flow regime was satisfied for the maximum analyzed mass flow rate (0.02 kg/s from Table 2.2) with a maximum Reynolds number *Re* around 2,000. Values for material properties were ranged in such a way they could comprehend a wide actual combination of HSM. Simulation was run for a 1 second time step and the original length *L* was divided into 100 sections, in order to guarantee output accuracy. The output fluid temperature $T_{f,N}(t)$ at the last section *N* was performed with the LEM approach by following the 6 steps presented in the flow sequence, implemented in a Fortran language:

1- Calculate the T3S fluid inlet temperature $T_{f,in}(t)$ at time t (Equation 2.10);

2- Perform the fluid temperature $T_{f,j}(t)$ (Equation 2.14) calculation at the outlet of the j^{th} section at time t with the HSM temperature $T_{s,j}(t-1)$ from the prior time $t-1$ (Equation 2.13);

3- Perform arithmetic average fluid temperature $\bar{T}_{f,j}(t)$ (Equation 2.15) from $T_{f,j-1}(t)$ and $T_{f,j}(t)$ for the j^{th} section at time t;

4- Perform the HSM temperature at time t (Equation 2.13) based on the temperature $\bar{T}_{f,j}(t)$ (Equation 2.15) from step 3;

5- Repeat steps 2 to 4 for all j sections for time t;

6- Repeat steps 1 to 5 for the next time step, and carry on the simulation till the end of the total time set to find the fluid outlet temperature $T_{f,out}(t)$ for the problem.

2.4 CFD solution

The CFD solution was implemented to provide a detailed answer to the same test case, as there were no experimental data suitable for it. The commercial code STAR-CCM+, 2017, solved mass, momentum and energy equation for the fluid flow and energy for the solid material (Equations 2.12 to 2.15), with the code built in Coupled flow and Coupled energy models, with a residue criterion of 10^{-6}.

The fluid output temperature predicted by the CFD solution was actually a field value, and an equivalent temperature $T_{f-CFD,N}(t)$ was proposed in Equation 2.18 to compare it to the one obtained from the LEM approach.

$$T_{f-CFD,N}(\mathrm{t}) = \frac{\int_{A_c} \rho_f \, u_f \, c_{p,f} \, T_f \, d \, A_c}{\dot{m} \, c_{p,f}} \tag{2.18}$$

A CFD mash independence test was performed and assessed with the aid of the Grid Convergence Index GCI [Roache, 1994; Celik et al., 2008] in respect to the fluid output temperature amplitude at the T3S N^{th} section. The average values on the Test column on Table 2.2, assessed in respect to the nine parameters range for the DoE Box-Behnken, were used to run the GCI methodology.

Table 2.2 - Data for the simulation of a reference Sensible Thermal Energy Storage System T3S.

Parameter	Description	Test	Minimum	Maximum
L	Plate length [m]	0.55	0.1	1.0
e_f	Plate distance [m]	0.105	0.010	0.200
e_s	Plate thickness [m]	0.105	0.010	0.200
$\dot{m}$	Air mass flow rate [kg/s]	0.0105	0.0010	0.0200
k_s	HSM thermal conductivity [W/mK], [18]	30.5	1.0	60.0
ρ_s	HSM density [kg/m³], [18]	4,500	1,000	8,000
$c_{p,s}$	HSM specific heat, [J/(kgK)], [18]	650	300	1,000
β	Inlet sine period [s]	45,000	3,600	86,400
Amp_{in}	Inlet temperature sine amplitude [K]	55.0	10.0	100.0

Results are displayed in Table 2.3 for three mash sizes and 1s time step.

Table 2.3 – CFD mesh independence test for the fluid output temperature amplitude.

Mesh	N° of elements	Quality	Amplitude [K]
M1	2,328	Coarse	44.2474
M2	4,600	Intermediate	44.3537
M3	8,536	Fine	44.4388

The convergence index $\varkappa$ [Roache, 1994; Celik et al., 2008] was found to be close to unit, which indicates that calculation reached an asymptotic solution. The intermediate mash M2 was chosen to run all the CFD simulations of this Thesis, due to its suitable accuracy and computing time effort.

Figure 2.5 shows the output fluid temperature $T_{f,N}(t)$ at the last section *N* calculated by Equation 2.14 together with results from the CFD code for the Test case, for further comparison, for an elapsed time of 180,000 s (50 h).

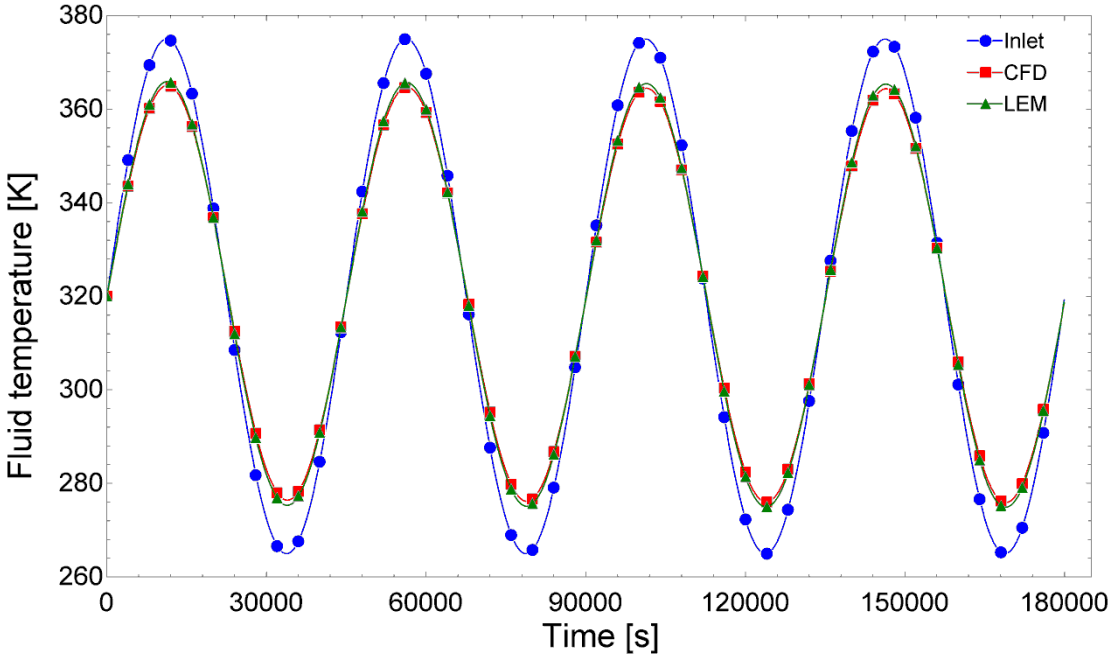

Figure 2.5 - T3S outlet fluid temperature $T_{f,N}(t)$ calculated by LEM and CFD for the reference model.

As shown in Figure 2.5, LEM to CFD outlet fluid temperature were very alike, with a maximum 2% deviation, which can be considered a good approximation for a lumped based solution.

2.5 Scale analysis

Scale analysis was performed to identify the relevance of specific phenomena and their related parameters on the T3S behavior, based on energy balances, without heat generation and for the constant and uniform properties displayed in Tables 2.1 and 2.2. The parameters that scale analysis identify as no-relevance can be neglected in a Design of Experiments technique. Energy equation for a laminar and incompressible fluid flow is written as follows

$$\rho_f \, c_{p,f} \frac{\partial T_f}{\partial t} + \rho_f \, c_{p,f} u_x \frac{\partial T_f}{\partial x} = k_f \left(\frac{\partial^2 T_f}{\partial x^2} + \frac{\partial^2 T_f}{\partial y^2} \right) \tag{2.19}$$

Fluid velocity along the *y* direction was neglected as it is times lower than the main stream one. Energy balance for the solid HSM was written considering heat diffusion, as follows

$$\rho_s \, c_{p,s} \frac{\partial T_s}{\partial t} = k_s \left(\frac{\partial^2 T_s}{\partial x^2} + \frac{\partial^2 T_s}{\partial y^2} \right) \tag{2.20}$$

Scale analysis begun by the approximation of the time differential ∂t to Δt for the inlet temperature senoidal period β. Both fluid and solid energy balances were rewritten by assuming $h \equiv q^{"}/\Delta T_f$; $\partial T_s/\partial y = h\Delta T_\infty / k_s$ and for unitary plate width W, $\partial T_f/\partial x = q'/\dot{m} c_{p,f}$ [Bejan, 2013] as follows:

Fluid energy balance

$$\underbrace{\frac{1}{\alpha_f} \frac{{e_f}^2}{\beta}}_{1st} + \underbrace{Nu \left(\frac{e_f}{L} \right)}_{2nd} = \underbrace{\frac{Nu}{Pe} \left(\frac{e_f}{L} \right)}_{3rd} + \underbrace{1}_{4th} \tag{2.21}$$

Solid energy balance

$$\underbrace{\frac{1}{Fo}}_{1st} = \underbrace{1}_{2nd} + \underbrace{\left(\frac{L}{e_s} \right)^2}_{3rd} \tag{2.22}$$

with the Nusselt *Nu*, Peclet *Pe*, and Fourier *Fo* numbers, defined as:

$$Nu = \frac{h e_f}{k_f} \, , \; Pe = \frac{u_x L}{\alpha_f} \, , \; Fo = \frac{\alpha_s \beta}{L^2} \tag{2.23}$$

Scale analysis was performed by sweeping all relevant parameters along their respective ranges proposed in Table 2.2. Beginning with the fluid energy balance (Equation 2.21), its 4th term can never be neglected, otherwise there would be no heat exchange among these media, as it accounts for the heat transfer at the solid to fluid HSM interface The 1st to the 2nd term ratio in that same equation ranged from 0.66 E-4 up to 0.53, showing that the 2nd term will be at least twice bigger then the 1st one (0.53), and many times bigger towards the end of the range, allowing to neglect the fluid transient behavior (1st term). The 2nd to the 3rd ratio is the Peclet *Pe* number, that ranged from 18 e 72 E3, meaning the dominancy of the advective transfer, allowing to neglect heat conduction along the axial direction *x* (3rd term).

Stepping ahead to the solid energy balance (Equation 2.21), its 1st term must be kept as it represents the solid thermal inertia. The 1st to the 2nd term ratio ranged from 0.73 E-3 up to 2.21 E3, which means that the 1st term can assume values that are 3 orders of magnitude

bigger or smaller than the 2nd one. The 2nd to the 3rd term ratio ranged from 01 E-4 up to 4, which means that all terms in Equation 2.22 showed to be relevant.

Fluid and solid energy balances (Equations 2.19 and 2.20) can now be rewrites as:

$$\rho_s \, c_{p,s} \frac{\partial T_s}{\partial t} = k_s \left(\frac{\partial T_s}{\partial x^2} + \frac{\partial T_s}{\partial y^2} \right) \tag{2.24}$$

$$\rho_f \, c_{p,f} u_x \frac{\partial T_f}{\partial x} = k_f \frac{\partial^2 T_f}{\partial y^2} \tag{2.25}$$

All 9 parameters listed in Table 2.2 can still be recognized in the simplified Equations 2.24 and 2.25, and were selected to perform a broader assessment of the LEM approach via a design of experiments technique, presented in the next section.

2.6 LEM range of validity

2.6.1 Parameter interactions

A set of controlled simulations were performed in order to assess the LEM accuracy when compared to CFD results for the 9 relevant parameters displayed in Table 2.2. Design of Experiments DoE encompasses several options for assessing the behavior of complex systems, providing tools to organize planned experiments [Montgomery, 2013] no matter if data are experimental or numerical. The nonlinear 3^k factorial design is a natural option, but would demand 19,683 simulations of both the LEM and CFD models, as k=9 control parameters. A less time consuming option is the Box-Behnken model, which displays the same ability to capture nonlinear tendencies and only needs 130 case combinations to perform the same task [Minitab Manual, 2018].

Results were assessed in respect to the relative deviations of LEM for outlet air temperature amplitude Dev_{Amp} and phase displacement Dev_{Phase} in respect to CFD calculations, whose values were expressed by Equations 2.26 and 2.27, respectively.

$$Dev_{Amp} = \frac{|Amp_{out,LEM} - Amp_{out,CFD}|}{Amp_{in}} 100 \tag{2.26}$$

$$Dev_{Phase} = \frac{|t_{Phase,out,LEM} - t_{Phase,out,CFD}|}{(\beta/2)} 100 \quad (2.27)$$

with $Amp_{out,LEM}$ and $Amp_{out,CFD}$ the outlet fluid temperature amplitudes, Amp_{in} the inlet fluid temperature amplitude, $t_{Phase,out,LEM}$ and $t_{Phase,out,CFD}$ are the phase times and β the senoidal phase. Deviations were assessed for a quasi-steady regime, reached for a periodic temperature fluctuation around a constant mean value, with the aid of the MiniTab software.

Analysis of the main effects for amplitude deviation showed that all 9 parameters caused maximum deviations close to 2%, but with significantly different behaviors, as shown in Figure 2.6.

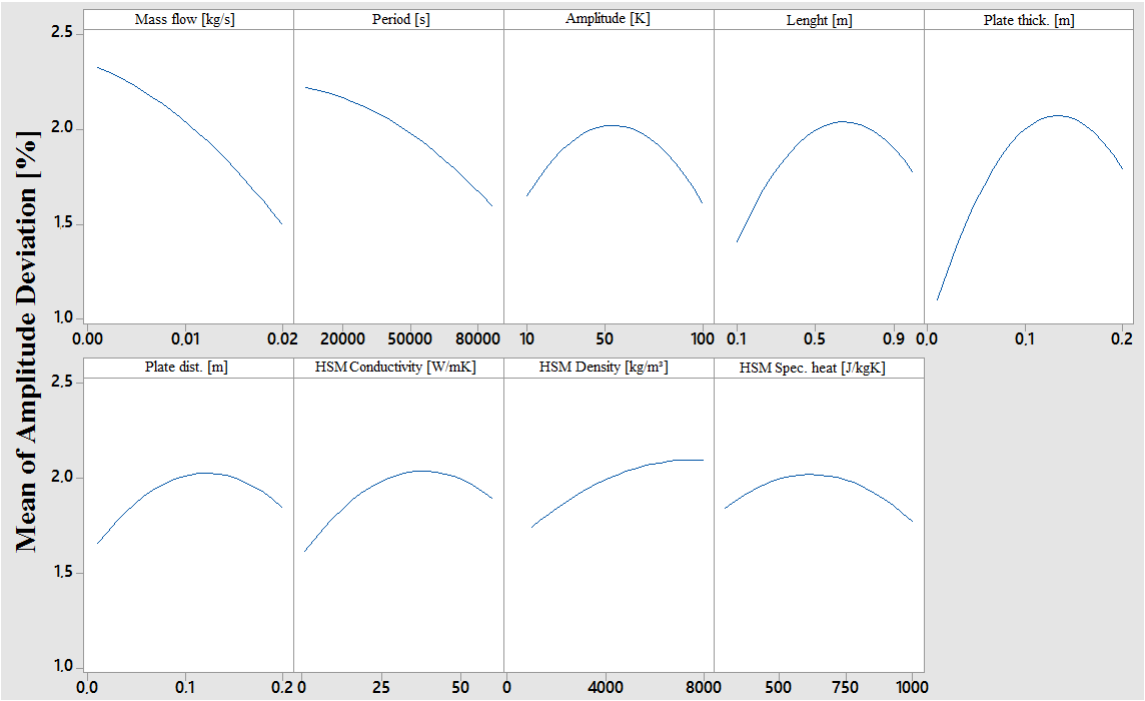

Figure 2.6 - Main effects of the 9 parameters of the Sensible Thermal Energy Storage System on the amplitude deviation Dev_{amp}.

Both the increase of the mass flow rate and the sinusoid period caused the reduction of amplitude deviations. Proportional behavior among some parameters in respect to amplitude deviations was observed. Both mass flow rate and the sinusoid period showed an inversely proportional tendency but HSM density was directly proportional. The other parameters behave nonlinearly, with maximum deviations around the center values of their individual ranges. All parameters displayed significant and predominant effects, which is corroborated by the interactions between the combined effects, shown in Figure 2.7.

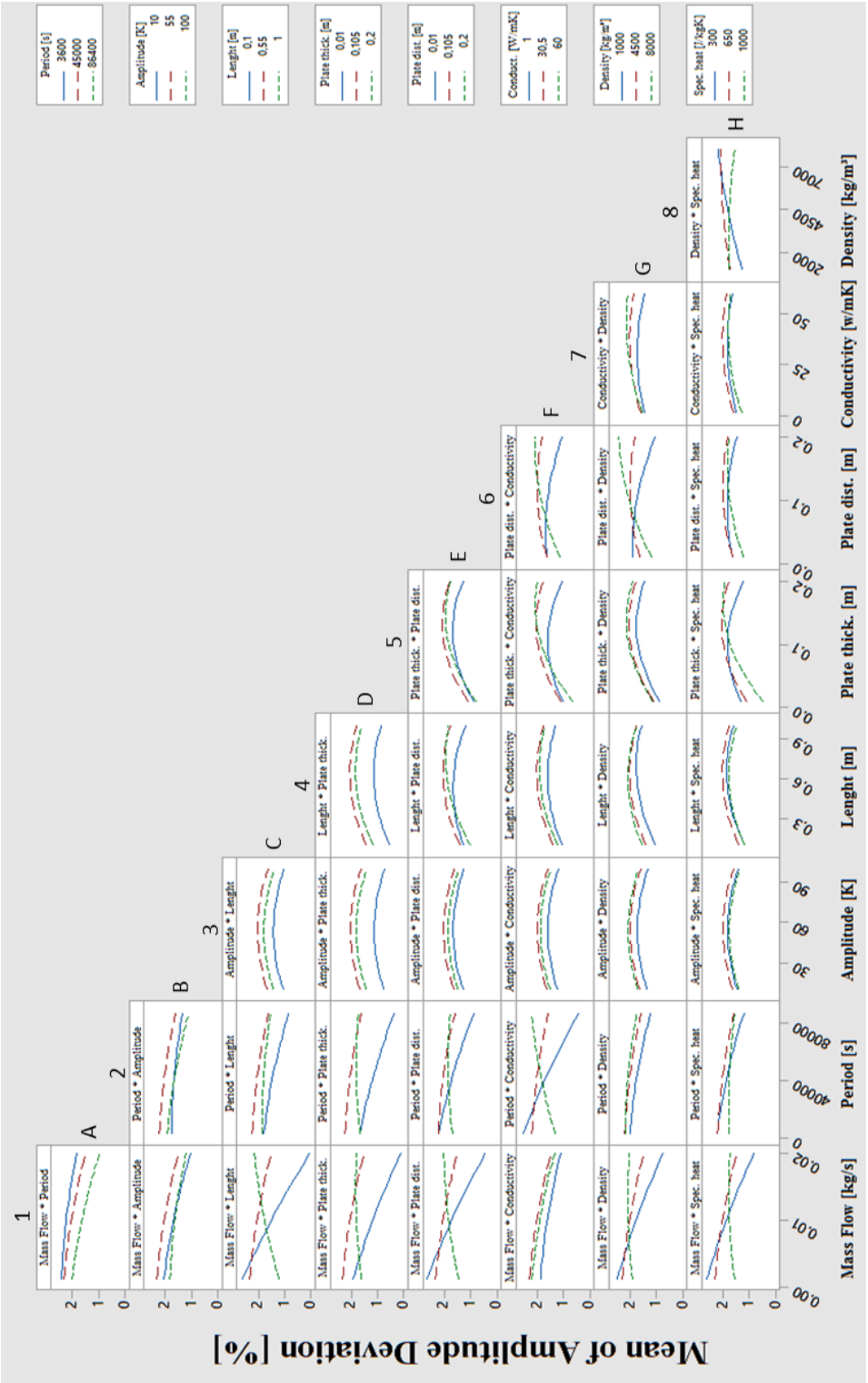

Figure 2.7 - Second order interactions between the 9 parameters of the Sensible Thermal Energy Storage System on the amplitude deviation Dev_{amp}. (Columns numbered from 1 to 8 and lines identified from A to H).

Interactions between pairs of parameters can be identified whenever their curves are nonparallel, meaning that the pair is mutually dependent. The more the lines are nonparallel, the greater the strength of the interaction [Minitab Manual, 2018]. Taking the pair flow rate to plate length (1C) as an example, the augmentation on flow rate lead to a smaller amplitude

deviation for plate length from 0.10 to 0.55 m, but made that deviation to rise at 1.00 m plate length, meaning that both parameters can mutually affect deviation in different ways. Strong iterations were observed for pairs 1C, 1D, 1E, 1G, 1H, 2D, 2E, 2F, 5H, 6F and 6G, which encompass most of the listed parameters, with the exception of the amplitude. Whenever the curves' slope is smooth, like in 8H, the parameters interaction is weak or negligible. Finally, parallel curves denote no iteration between parameters, like in 3C and 1F.

The same assessment was performed for main and combined effects in respect to phase displacement Dev_{Phase}, displayed in Figures 2.8 and 2.9 respectively.

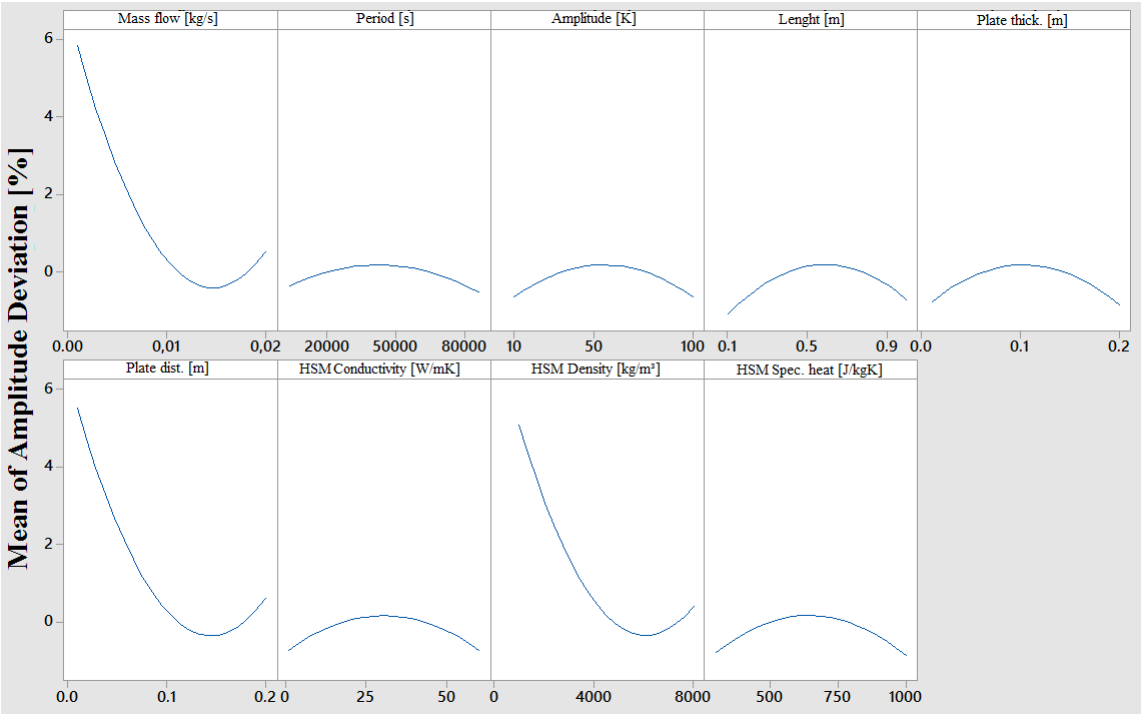

Figure 2.8 - Main effects of the 9 parameters of the Sensible Thermal Energy Storage System on the phase deviation Dev_{Phase}.

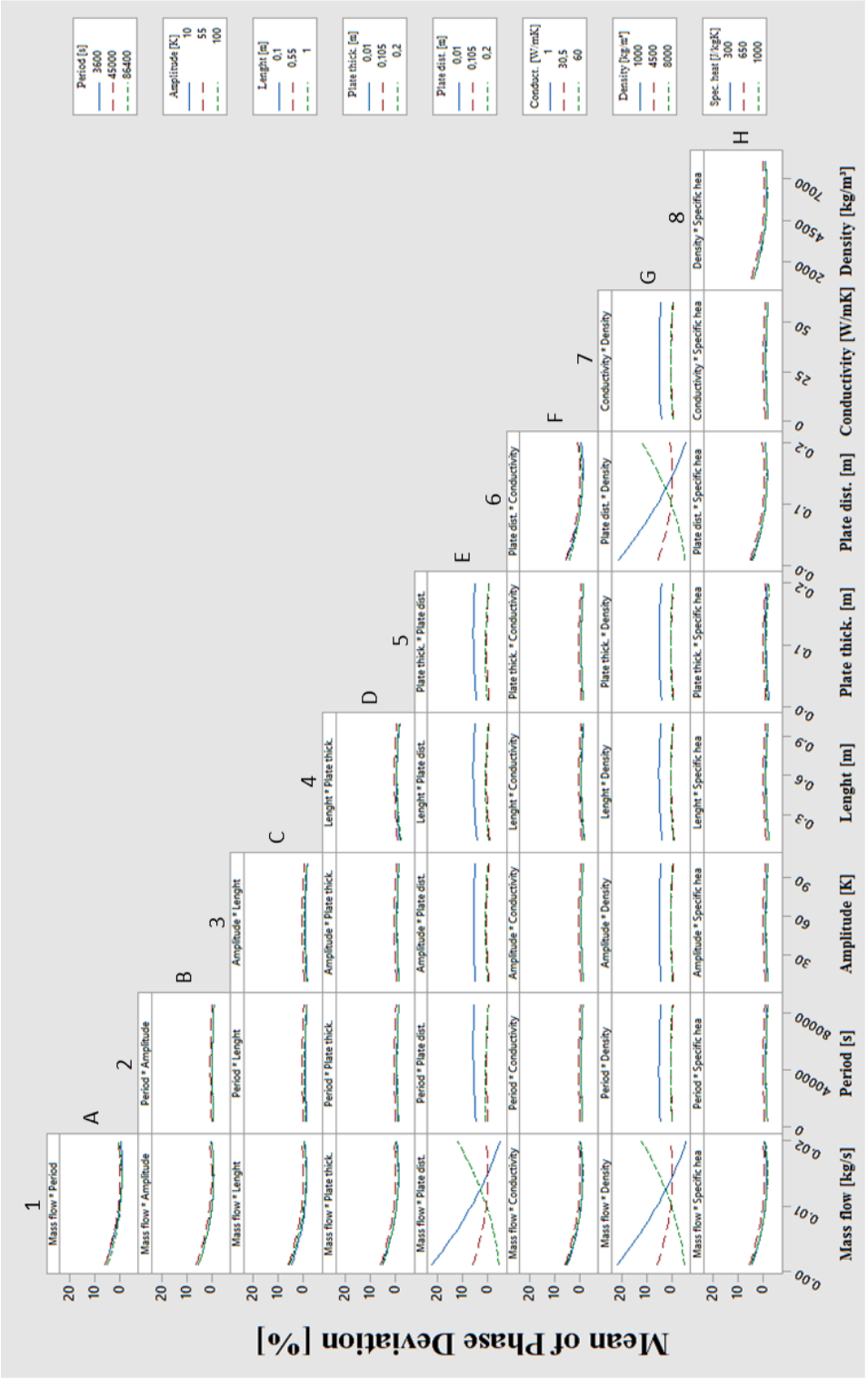

Figure 2.9 - Second order interactions between the 9 parameters of the Sensible Thermal Energy Storage System on the phase deviation Dev_{Phase}. (Columns numbered from 1 to 8 and lines identified from A to H).

Curves in Figure 2.8 and pairs 1E, 1G and 6G in Figure 2.9 showed that phase deviation was mainly dependent of mass flow rate, plate distance and HSM density. Individual effects (Figure 2.8) of these parameters did not exceed 6%, whereas they reached maximum values of 20% for second order iterations.

2.6.2 Overall deviation

Figure 2.10 brings a more detailed view on the modeling behavior, by classifying it on deviation ranges.

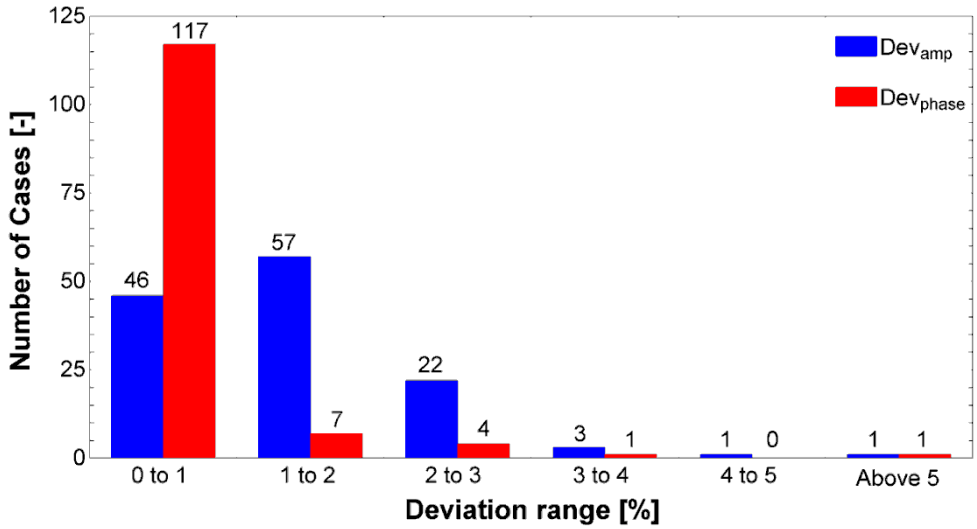

Figure 2.10 - Histogram of fluid output temperature amplitude and phase deviation between LEM and CDF for the Sensible Thermal Energy Storage System.

Temperature amplitude deviation of the LEM model in respect to CFD results lied within 2% for approximately 80% of the simulated domain (103 combinations). Temperature phase deviation was even better, with 95% of the simulated domain (124 combinations) within the same deviation limit. Looking at the extreme cases, the maximum deviations of 5.5% for temperature amplitude and 89% for temperature phase were observed for the same case, labeled as 55. That last value was quite unusual, as the rest of the test sample did not displayed phase deviation higher than 4%. Simulated values for the outlet air temperature for case 55 is presented in Figure 2.11, followed by its parameter values.

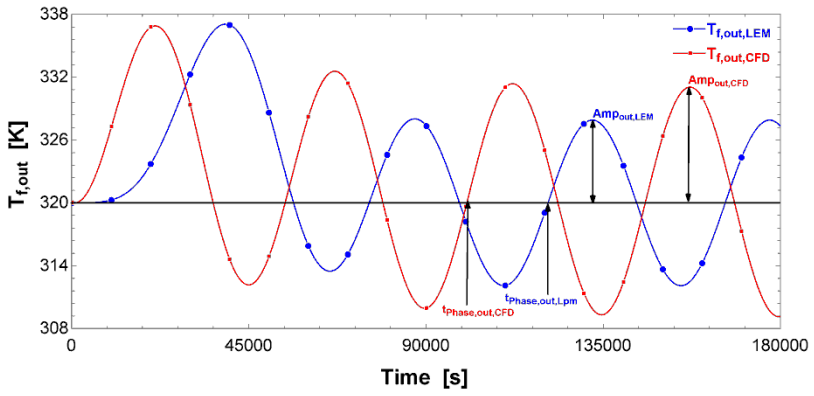

Case 55:

e_f= 0.01 [m]

e_s= 0.105 [m]

L= 0.55 [m]

$\dot{m}$= 0.001 [kg/s]

β= 45,000 [s]

Amp_{in}= 55 [K]

k_s= 30.5 [W/mK]

ρ_s= 1,000 [kg/m³]

$c_{p,s}$= 650 [J/(kgK)]

Figure 2.11- LEM and CFD simulations for the T3S outlet air temperature T3S for case 55.

Case 55 displays a particular combination of high Number of Transfer Unit NTU value and high HSM axial heat conduction. NTU is the ratio of heat convection exchange to fluid heat capacity along the solid to fluid interface, as shown in Equation 2.28,

$$NTU = \frac{\bar{h} A_s}{\dot{m}\, c_{p,f}} = \sum_{j=1}^{n} \frac{(\bar{h}\, A_s)_j}{\dot{m}\, c_{p,f}} \tag{2.28}$$

Case 55 displayed a NTU value of 5.788, the highest among all simulated cases, with a HSM thermal conductivity of 30.5 $Wm^{-1}K^{-1}$. High NTU values indicate intense heat transfer notably at the entrance of the T3S, which leads to temperature differences along the HSM axial direction, which can only be captured by CFD models. In order to confirm that observation, case 55 was resimulated for small thermal conductivity (1 $Wm^{-1}K^{-1}$) and amplitude and phase deviations were reduced to 2.36% and 45.78%, respectively.

CFD simulations were performed by 5 independent Intel Core i7, 3.4 GHz, 4GB RAM computers and one Intel Xenon 12 cores, 3.47 GHz, 48 GB RAM and took 30 consecutive days. LEM simulations were performed by one Intel Core i7, 3.4 GHz, 4GB RAM computer and took 30 minutes.

2.7 Conclusion

The use of a Lumped Element Method LEM approach to model and simulate a Sensible Energy Storage System, called here T3S, was presented and discussed. The proposed T3S case study was composed by a set of flat parallel plates, the Heat Storage Material HSM,

separated by narrow channels where an induced fluid stream carries the exchanged energy of the system. The T3S was submitted to a cyclical thermal flow stream and its goal was to retrieve a conditioned output, working as a thermal rectifier. The LEM model was already used to find T3S optimal configurations by the authors in other research work, but the model accuracy needed to be ascertained. Results from a reference CFD solution were presented by solving the symmetric domain composed by one half part of the heat storage material and one half of flow channel.

The temporal evolution of the fluid temperature in the T3S discharge was used to observe the amplitude and phase deviations in respect to the reference case, throughout a design of experiment procedure. Nine T3S controlled parameters were identified: distance between HSM plates, HSM plate thickness, HSM plate length, air mass flow rate, HSM thermal conductivity, HSM density and HSM specific heat, sinusoidal function period and function amplitude. The Box-Behnken experiment planning technique was chosen due to its capacity to capture nonlinear behaviors and smaller case combinations in comparison to a 3^k factorial experiment, which reached 130 combinations for the former and would demand 19,683 simulations for the latest.

The nine T3S controlled parameters showed to be significant and displayed similar influence on the amplitude deviations, whereas only air mass flow rate, distance between HSM plates and their densities appeared to be more relevant for phase deviations.

Among the 130 Box-Behnken combinations, amplitude deviations from LEM in respect to CFD solutions displayed overall differences below 6%, composed by 46 cases below 1% and 103 cases below 2%. Deviations related to the phase shift did not exceed 4%, with only an exceptional situation of 89%, due to the importance of the heat conduction along the HSM axial direction, meaning that significant deviations between LEM and CFD models occur only when T3S combines high NTU and HSM thermal conductivity values. Whenever both parameters are sufficiently low, deviations will not be significant.

The present study showed that thermal energy storage systems like the one proposed in this Thesis can be simulated with LEM, allowing to perform further optimization studies.

3 OPTIMIZATION OF A SENSIBLE THERMAL STORAGE SYSTEM BY A LUMPED APPROACH[3]

The geometry and the HSM mass of the previously T3S are the main subject of this chapter. The objective is to find the minimum HSM mass and the T3S geometry that guarantee its operation within an admissible temperature range. The HSM is modeled as a Lumped system and the working fluid by a non-capacitive energy balance. The T3S is composed by an array of parallel flat plates submitted to a sinusoidal cyclic air stream. The exhaustive search method is used to find the minimum HSM mass and the T3S geometry. It is observed that the minimum heat storage mass is proportional to the mass airflow rate. An optimal relationship between the superficial heat transfer rate and the fluid flow inertia, given by the dimensionless parameter NTU, is found to be constant (4.03) and independent in respect to the mass flow rate. The system time constant was invariable (3,230 s) for the optimal relationship between the interface heat transfer rate and the system inertia.

3.1 Introduction

Among the renewable sources, solar energy is recognized as one of the most promising ones, mainly because it is abundant, free and environmentally clean. However, solar energy is intermittent, seasonal and varies according to local conditions. Thus, its storage can play a special role whenever the system is meant to operate under continuous and stable conditions. Energy accumulators can reduce the time delay between demand and supply, thereby improving the system performance.

In this context, the study of Thermal Energy Storage (TES) systems is gaining strength today. Published reviews [Hasnain, 1998; Bal et al., 2010 and Cabeza et al., 2011] on TES systems classify the Heat Storage Materials (HSM) in two main groups: sensible and latent HSM, or PCM. In a general view, HSM must be chemically stable, with high thermal conductivity and high storage capacity, which means high density combined to high specific heat, non-toxic and non-corrosive. Latent HSM must also display high phase change enthalpies together with small volume variation along the phase change.

---

[3] Autors: Tiago Haubert Andriotty*, Letícia Jenisch Rodrigues, Luiz Alberto Oliveira Rocha, Paulo Smith Schneider

*tiago.haubert@ufrgs.br (corresponding author)

A numerical code to evaluate a coriander solar dryer was developed by Chauhan, 1996. Two cases were assessed: in the first case, the drying process was performed without any storage system, while in the second one, rocks were used as HSM. The objective was to reduce the coriander moisture from 28,2% to 11,4%. Results indicated 27 sunshine hours (3 days) for the first case and 31 cumulative hours, including the night period, for the second case.

A high temperature heat storage system for Solar Thermochemical Pipeline System was optimized by Sragovich, 1989. The author adapted the methodology proposed by Duffie and Beckman, 2013, based on a Lumped approach to evaluate the HSM coupled to an energy balance applied to the working fluid. The objective was to sustain the system air temperature above 900°C along cloud periods for at least 30 min. The optimization focused the geometry of the heat exchanger and attained the operational.

Salomoni et al., 2014, proposed two different numerical methodologies to design a sensible TES with tubular channels inside concrete blocks for solar power plants, with water as the working fluid.

The HSM model was solved by a finite element numeric approach, and the heat transfer along the interface with the working fluid was modeled by convective correlations. In the first methodology, named “quasi-steady”, the fluid was modeled in one unique control volume and its transient term was neglected. The second one, named “non-steady”, discretized the fluid in several volumes, following Sragovich, 1989. Both models reached similar results whenever the tube length did not exceed 10 m. In this case, authors suggested that the “quasi-steady” model was more indicated, since it demanded less computational effort. For longer tubes, the “non-steady” model generated better results.

The present chapter was about the geometrical aspects of a heat storage system, and focused on the search of a minimal HSM mass under a given geometry, capable of operating a cyclic TES system within an admissible temperature operating range.

3.2 LEM implementation

In addition to the LEM formulation presented in chapter 2, two new definitions were introduced in Equations 2.13 and 2.14: the time constant τ and the Number of Transfer Units NTU [Duffie and Beckman, 2013], as followed

$$\tau = \frac{M_s C_{p,s}}{hA_{s,j}} = \frac{c_{p,s}\rho_s V_{s,j}}{hA_{s,j}} \tag{3.1}$$

$$NTU_j = \frac{NTU}{n} = \frac{hA_{s,j}}{\dot{m}\, c_{p,f}} \tag{3.2}$$

Equations 2.13 and 2.14 were rewritten after these definitions as:

$$T_{s,j}(t) = T_{s,j}(t-\Delta t) - \left[1 - exp\left(-\frac{\Delta t}{\tau}\right)\right]\left(T_{s,j}(t-\Delta t) - \overline{T}_{f,j}(t)\right) \tag{3.3}$$

$$T_{f,j}(t) = T_{s,j}(t) - \left[exp\left(-NTU_j\right)\left(T_{s,j}(t) - T_{f,j-1}(t)\right)\right] \tag{3.4}$$

3.3 Simulation parameters

The T3S inlet air temperature $T_{f,in}(t)$ was predicted by Equation 3.5

$$T_{f,in}(t) = T_{f,in(-)} + \left[1 + sen\left(\frac{\pi t}{\beta/2}\right)\right]\left(\left[T_{f,in(+)} - T_{f,in(-)}\right]/2\right) \tag{3.5}$$

with inlet air temperature ranging from $T_{f,in(-)}$ = 290 K to $T_{f,in(+)}$ = 350 K. This simple sine wave expression can represent cyclic behaviors in storage systems. Simulations were performed for 10 cycles of β = 20 000 seconds each.

Stainless steel AISI 304 was chosen as the HSM, due to its high volumetric heat capacity (Table 3.1) and air was the heat transfer fluid (Table 3.2).

Table 3.1 - Thermophysical properties of the HSM [Bergman et al., 2011].

Material	Density ρ [kg/m³]	Specific heat c_p [J/(kgK)]	Thermal conductivity k [W/(mK)]	Thermal diffusivity [m² /s]	Volumetric heat capacity [J/(m³K)]
AISI 304 (steel)	7 900	477	14.90	3.95 E-6	3.76 E+6

Table 3.2 - Air proprieties calculated with respect to an average temperature of 320 K [Bergman et al., 2011].

Density ρ [kg/m³]	Specific heat c_p [J/(kgK)]	Dynamic Viscosity μ[kg/(ms)]	Prandtl Number *Pr* [-]	Thermal conductivity k [W/(mK)]	Volumetric heat capacity [J/(m³K)]
1.103	1 008	1.949 E-5	0.705	2.785 E-2	1.111 E+3

3.4 Solution algorithm

Five different mass flow rates $\dot{m}$ are analyzed and for each one was searched the minimum HSM mass that satisfied the following condition

$$T_{\mathrm{ran}(-)} < T_{\mathrm{f,out}}(t) < T_{\mathrm{ran}(+)} \quad \text{with} \quad T_{\mathrm{ran}(-)} = 316\ K \text{ and } T_{\mathrm{ran}(+)} = 324\ K \tag{3.6}$$

Thus, the HSM mass was the objective function, while plate length *L* and plate distance e_f are the best system geometry that satisfied Equation 3.6.

The HSM mass minimization was performed by exhaustive search written in a specific FORTRAN code. The geometric limits of the plate length *L*, plate distance e_f, HSM mass M_s, and the five mass flow rates $\dot{m}$, as well as the increment of each parameter for the exhaustive search method are presented in Table 3.3.

Table 3.3 – T3S parameters for the exhaustive search.

Parameters	Range	Increment
Mass flow rate [kg/s]	0.001 – 0.005	0.001
HSM mass [kg]	10 – 180	0.01
Plate distance [m]	0.01 – 0.5	0.01
Plate length [m]	0.1 - 6	0.1

It is worth noting that a trivial solution for the T3S to deliver the working fluid at a constant output temperature, 320 K for the inlet air temperature profile in Equation 3.5, can be reached with HSM infinite mass, which is far from a good technical and economical option.

The verification whether the T3S was operating within the admissible outlet fluid temperature range was simplified by following the results for the maximum outlet fluid temperature. Thus, the optimal solution for the T3S was the plate length and plate distance in which the minimum HSM mass that reduced the maximum outlet fluid temperature within the operational range (Equation 3.6).

The optimization was only performed for stabilized cycles, i.e., when the cycling output amplitude remained constant, after 5 cycles. Simulations were performed with several section numbers and time steps, with domain independence around 60 sections. The same procedure was applied to the time discretization and a time step of 100 s was found to be adequate.

3.5 Results

The results for minimum HSM mass of the T3S were those able to keep the outlet fluid temperature within the limits of Eq. 3.6 as shown in Figure 3.1.

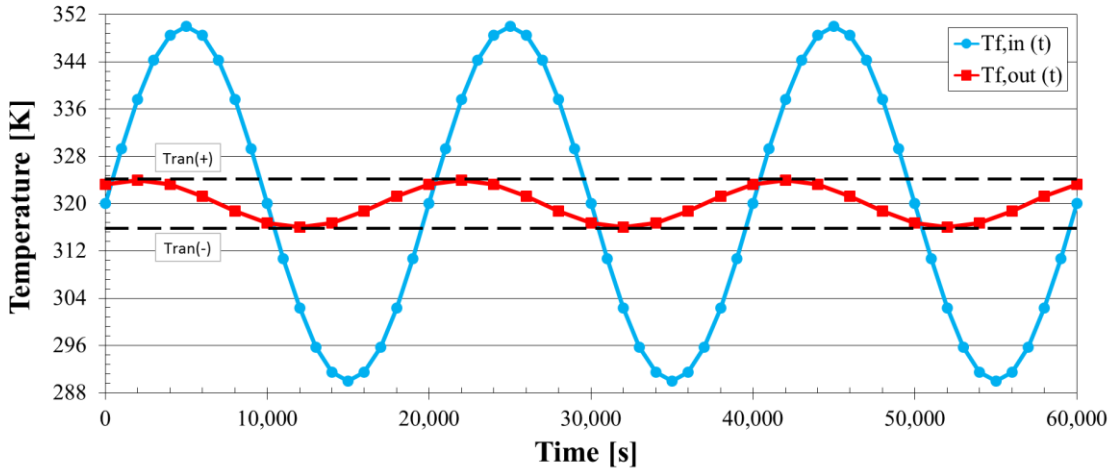

Figure 3.1 - Outlet fluid temperature for the optimized sensible TES system.

Figure 3.2 displays the maximum outlet air temperature for various HSM mass and the minimum HSM mass that satisfies the bound in Equation 3.6.

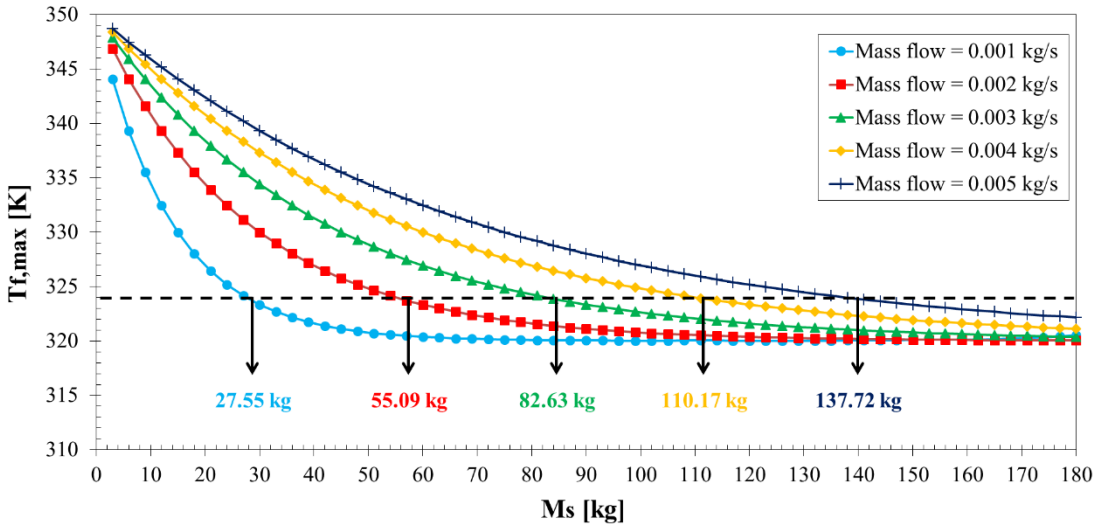

Figure 3.2 – Best system geometry relative to the HSM mass, with the minimum HSM mass that satisfy the admissible temperature range.

The greater the mass flow rate, greater the HSM mass necessary to operate the TES within the temperature operating range (Equation 3.6). It was observed that the increase in the HSM mass was directly proportional to the mass flow rate. Moreover, the geometry of the T3S, i.e. plate length and plate distance, was not fixed.

The optimal HSM mass can be a combination of different geometries, which still satisfied the operating range, meaning that the system surface area (dependent on the plate length) and the heat transfer coefficient (dependent on the plate length and plate distance) were interdependent. Figure 3.3 shows the maximum outlet fluid temperature as a function of the NTU, for 0.001 kg/s mass flow rate.

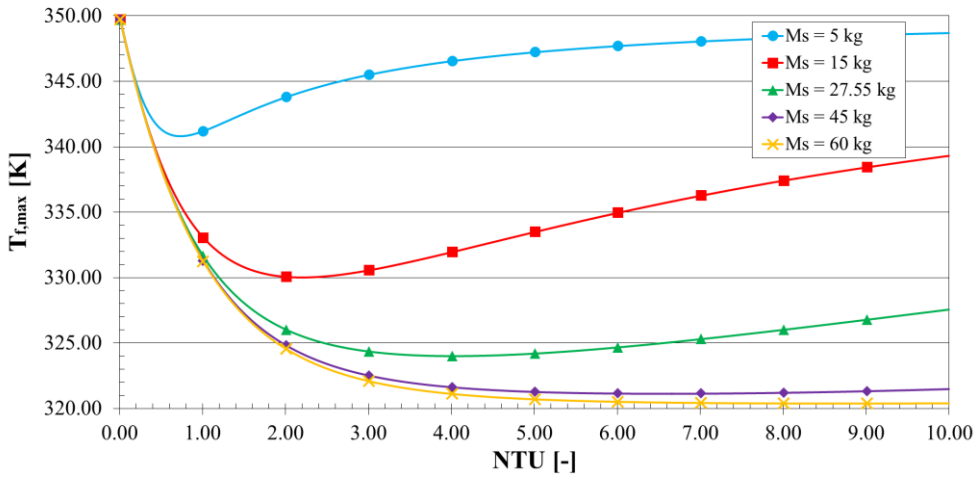

Figure 3.3 - Maximum outlet fluid temperature as a function of NTU for different HSM mass.

The 4th curve represents the behavior of the minimal HSM mass (*Ms*=27.55 kg), which satisfied the temperature operating limit from Equation 3.6, with NTU = 4.03. Smaller NTU values led to weaker heat transfer rates, which was not capable of adequately control the fluid flow inertia, given by $\dot{m}\, c_{p,f}$. But, for high NTU values, it is not so evidently why the maximum outlet air temperature increases. To understand this behavior, the results for NTU = 4.03 and NTU = 10 were compared in respect to the HSM temperature (Figure 3.4) and the average heat transfer rate (Figure 3.5), calculated according to Equation 3.7.

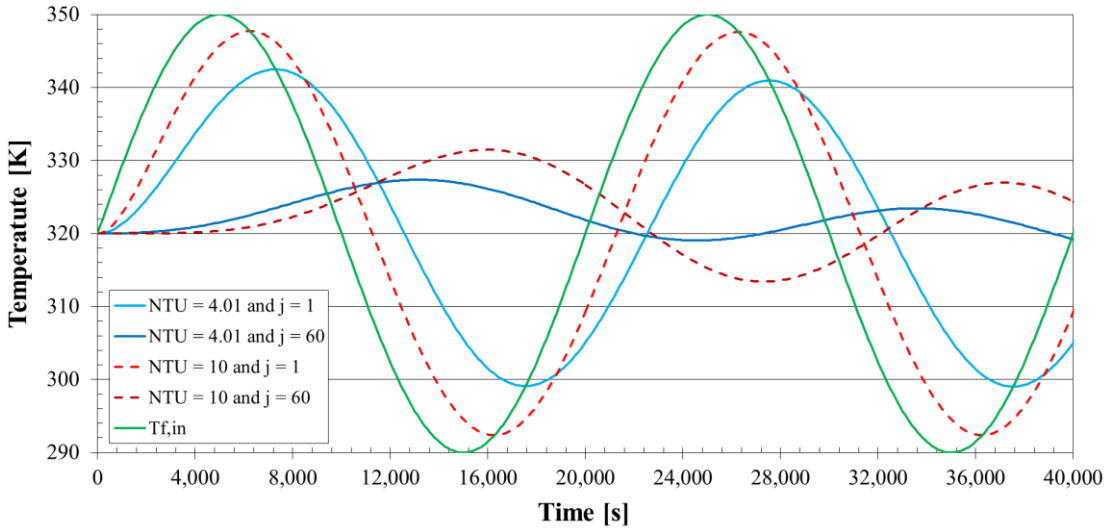

Figure 3.4 – Temperature behavior of the HSM first and last sections for the cases with NTU = 10 and NTU = 4.03.

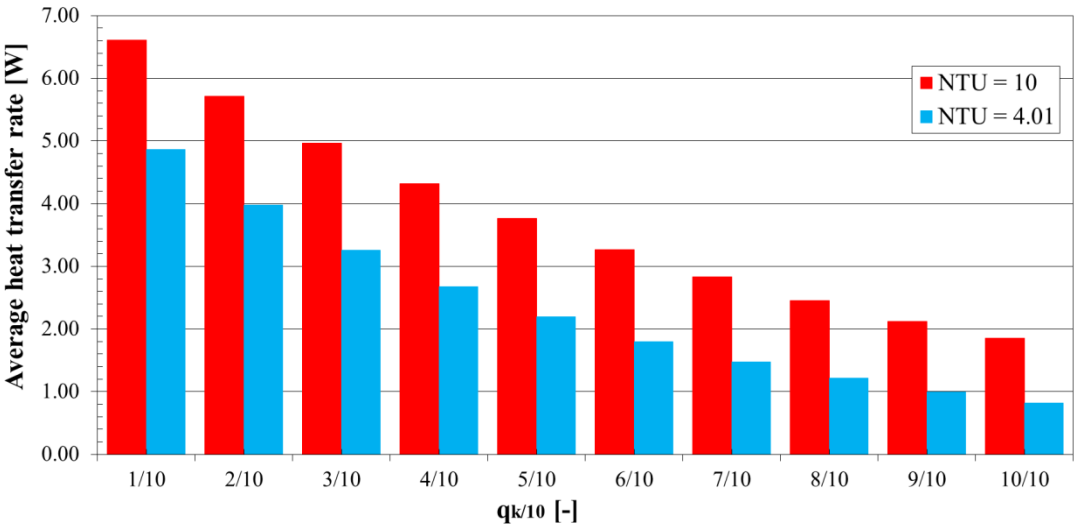

Figure 3.5 – Average heat transfer rate for each 1/10 plate length.

$$q_{\frac{k}{10}} = \sum_{i=0}^{i=\frac{\beta}{\Delta t}} \frac{\left|T_{f,j=1+6(k-1)}(t) - T_{f,j=1+6(k-1)}(t+1)\right| + \left|T_{f,j=7+6(k-1)}(t) - T_{f,j=7+6(k-1)}(t+1)\right|}{2} \frac{\left(\frac{M_s}{10} C_{p,s}\right)}{\beta} \quad (3.7)$$

$for\ k = 1,2,\dots,10$

The temperature of first and last HSM sections for NTU = 10 oscillated more than for NTU = 4.03. This behavior is caused by a more intense average heat transfer rate for NTU = 10, as showed in Figure 3.5, which is more difficult to control. This emphasis the existence of an optimal correlation between heat transfer rate and fluid flow inertia and that only enhancing the system heat transfer it is not always beneficial to the project design.

By analyzing the behavior of NTU in the best plate length and plate distance for each different HSM masses it was possible to observe that it reached a constant value (4.03), independent of the mass flow rate, as displayed Figure 3.6.

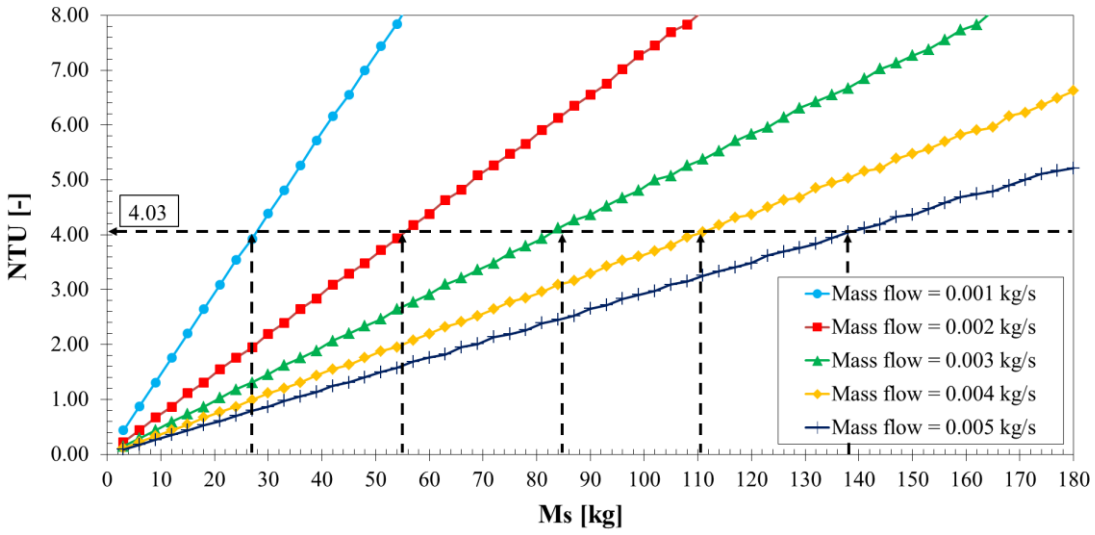

Figure 3.6 - NTU value (4.03) that minimize the maximum outlet fluid temperature for different HSM mass.

This indicated that the NTU value remain fixed, independent of the mass flow rate and satisfied the operational limits given by Equation 3.6. Therefore, it was possible to determine the plate length and plate distance for the T3S, based on the NTU optimal number.

As NTU characterized the working fluid behavior, the same analyses was made to evaluate the HSM behavior, described by the HSM time constant τ. It was observed that the time constant reached the same value, 3,230s for all optimal NTU values. This result is similar to the NTU behavior, which indicated that there was a desirable HSM behavior, to satisfy the admissible temperature operating range. As a conclusion, it was noticed that the

T3S can be designed according to the HSM time constant and the fluid NTU for a given inlet air temperature and a prescribed outlet air temperature behavior.

Pressure drop

Another important aspect that deserves to be mentioned is the T3S pressure drop. Like previously observed, there are infinite combinations of plate length and plate distance for the minimal HSM mass that guaranteed the outlet fluid temperature within the operational range. Although the system thermal behavior converged always to the same optimal values (NTU and τ), the same not occurs to the pressure drop. Based on Çengel, 2011, the pressure drop for laminar flow inside a channel formed by infinite parallel flat plates (i.e., unitary plate width W) can be estimated as

$$\Delta P = \frac{12\mu \dot{m} L}{\rho_f {e_f}^3 W} \tag{3.8}$$

Figure 3.7 shows the dimensionless pressure drop, relative to the maximum pressure drop (e_f = 0.06 m), for the mass flow rate 0.002 kg/s and the best plate length and plate distance configurations. Due the exhaustive search approach and the increments of Table 3.3, some oscillations were observed. If smaller increments were applied, the oscillations will be suppressed and more optimal configurations will be found, until de limited of infinitesimal increments, which will resulted in infinite number of best configurations.

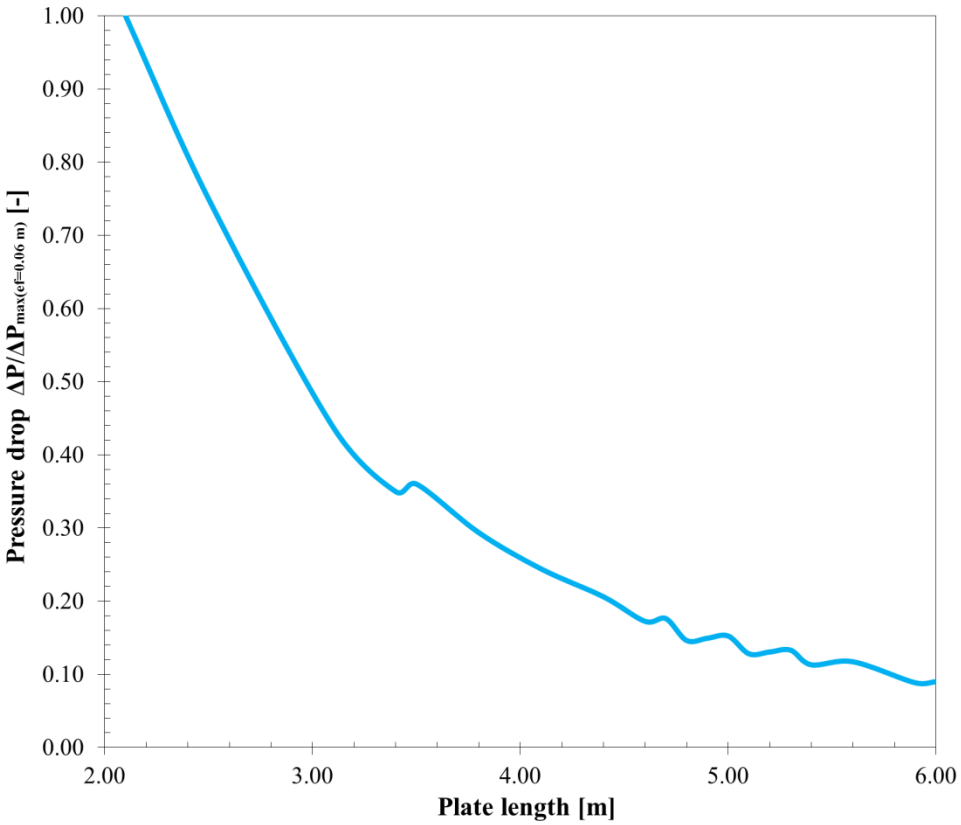

$L[m]$	e_f[m]
2.1	0.06
2.5	0.07
3.1	0.09
3.4	0.10
3.5	0.10
3.8	0.11
4.1	0.12
4.4	0.13
4.6	0.14
4.7	0.14
4.8	0.15
4.9	0.15
5.0	0.15
5.1	0.16
5.2	0.16
5.3	0.16
5.4	0.17
5.6	0.17
5.9	0.19
6.0	0.19

Figure 3.7 – Dimensionless pressure drop, relative to the maximum pressure drop (dashed red line), for the mass flow rate 0.002 kg/s and the best plate length and plate distance configurations.

The greater the plate length, smaller the pressure drop, as the plate distance increase. According to Equation 3.7, the pressure drop is inversely proportional to the plate distance 3th power, but only linearly proportional to the plate length. The plate distance is more significant than the plate length. If the pressure drop is an important factor for the storage system, than may be a good choice to design a large system, if space is not a restriction.

3.6 Conclusion

The minimization of the Heat Storage Material HSM mass that guaranteed an outlet airflow temperature within the operational range was performed. The minimal HSM mass was found to be linearly proportional to the mass airflow rate, but the dimensionless parameter

NTU, the Number of Transfer Units, converged to the common value of 4.03. This behavior allows for the characterization of the T3S and must be better investigated. This result showed that, for a prescribed inlet flow condition, there was an optimal relationship between the interface heat transfer rate and the fluid flow inertia. A similar result was observed for the HSM behavior, where the HSM time constant of 3,230s was reached as the optimal relationship between the interface heat transfer rate and the HSM inertia.

Both constant values indicated the existence of an optimal relationship between the thermal behaviors of the fluid flow and HSM that guarantee the desired temperature operating range.

4 INVERSE DESIGN METHODOLOGY TO OPTIMIZE SENSIBLE THERMAL ENERGY STORAGE SYSTEMS WORKING AS RECTIFIERS[4]

The forth chapter expands the analyses of the previous chapter and generalizes the T3S behavior as functions of the NTU and time constant. With this generalization, it is possible to present a methodology to achieve the optimal design of a Sensible Thermal Energy Storage System T3S working as a thermal rectifier. The system was composed by the Heat Storage Material HSM, distributed in a set of flat parallel plates, and the working fluid, both modeled by a simplified Lumped Element Model LEM. The ratio of operational outlet temperature range to source temperature oscillation is defined as the designed rectifying duty. Optimization procedure combines a one-factor-at-a-time OFAT and line search strategies in order to find optimal T3S design that satisfies the designed rectifying duty with the minimum HSM mass. The Inverse Design philosophy is applied to the optimal results to generalized the T3S dynamic behavior as functions fitting curves of the Number of Transfer Unit NTU and the time constant τ. These fitting curves can be used to identify T3S geometric parameters, , HSM thermal properties, fluid inlet conditions, among others, which guarantee the outlet fluid temperature to be found within the operational range with the minimum HSM mass. A 3 step-by-step sequence design methodology is presented and detailed, based on design charts from the NTU and τ correlations. The proposed design methodology is able to find the optimal plate length L, plate thickness e_s and plate distance e_f that satisfies the designed rectifying duty for three test cases. These optimal T3S designs are simulated in a CFD code, with deviations below 1.5% between the designed rectifying duty and the one simulated. With the proposed approach, several design solutions or configurations can be found for T3S operating as a thermal rectifier based on NTU and τ fitting curves submitted to a sinusoidal cyclic temperature input and with constant and uniform HSM and fluid properties.

4.1 Introduction

Sensible Thermal Energy Storage Systems T3S must be accessed according to their storage material and application. Literature review indicates previous work on design methodologies connecting storage system characteristics to operational condition, like the one

---

[4] Autors: Tiago Haubert Andriotty[*], Paulo Smith Schneider, Letícia Jenisch Rodrigues

[*]tiago.haubert@ufrgs.br (corresponding author)

from Klein et al, 1976, which proposed graphical design tools for domestic solar systems, known as f-chart, with air or water as thermal fluids.

Schmidt and Szego,1976, and Schmidt et al, 1977, proposed storage systems based on flat parallel plates, by modeling the working fluid as a transient 1D capacitive flow and the solid media as a transient 2D storage material. Results were presented in diagrams oriented to system design by selecting material thickness and length, plate distance, operational fluid temperatures and heat storage.

A design method for Concentrated Solar Power CSP plants was proposed by Li et al, 2012, based on similarity analysis, which was able to generalize system devices, such as water tanks, rock beds and imbedded tubes into Heat Storage Materials HSM. Results were once more presented in graphical form, relating system geometry to load and unload times.

Jian et al, 2015, modified a Lumped model by using Laplace transforms to solve several T3S configurations, whose accuracy was verified in respect to a real scale concrete prototype storage unit and showed reasonable agreement. A T3S design procedure was presented, in order to reduce the system costs.

Gude et al, 2012, worked on low temperature (40-50°C) water desalinization systems based on solar collectors with sensible heat storage, solved by a semi-analytical model. Authors submitted the system to a 3-week clear sky weather sequence and a 3-week weather sequence with one cloudy day per week. Freshwater production rate for a non-storage system was 50% smaller on cloudy weather compared to the clear sky one, but differences were found to be 8% with a 1 m^3 HSM, and 5% for 3 m^3 HSM.

Darzi et al, 2013, simulated the use of Phase Change Materials PCM to reduce the air conditioning consumption in buildings, by storing low level energy during nighttime. The system effectiveness was proven for short operation periods, but it rapidly decreased for longer periods.

Zanganeh et al, 2014, proposed a hybrid sensible and latent packed bed heat storage system. The system was modeled by a transient one-dimensional formulation and submitted to an air inlet flow with cyclic temperature. The PCM was placed in the system outlet in order to stabilize the fluid temperature, and its minimum dimension represented only 1.33% of the total volume, which was less than 5% of the total storage energy in the system, mainly based on sensible storage.

Soda and Beyene, 2016, assessed different PCMs to be used in an organic Rankine cycle. Authors emphasized that the advantage of latent heat storage in respect to sensible one

relies on its capacity to deliver constant fluid output temperature, a desirable quality whenever steady state regimes are to be performed, but highlighted handicaps as inflammability, hysteresis and cost.

Rezaie et al, 2017, studied the T3S transient behavior along charging and discharging duties. The T3S was modeled as a fully mixed storage system, neglecting temperature gradients within the storage material and capable of recovering the entire input energy flow rate. Results showed that the increase in discharging temperature could be met by adjusting both the input and output energy rates associated to the working fluid.

Ghoreishi-Madiseh et al, 2017, studied deep mine thermal air conditioning. Heat stored in a rockpit along summer days was employed during winter, as a sort of seasonal thermal rectifier. Volume average theory was used to model a 3D unsteady porous media for a 10 years long period, and compared to real data from the Creighton mines in Canada. T3S was able to save up to US$ 437,000 per year and to reduce 8,862 tons of carbon emissions by avoiding artificial conditioning systems.

Demir and Dincer, 2018, proposed the integration of a Thermal Energy Storage TES to a solar energy system for fresh water and electricity production. The system was based on a Rankine cycle driven by solar energy stored at a molten salt medium coupled to a multi-stage flash process for water desalination. The authors found that the highest exergy destruction and heat losses were identified to occur at the solar receiver and the steam generator, in contrast to lower ones for the storage tanks.

Whenever the storage system operates under continuous regime, the inlet energy brought by the working fluid is partially storage by the system material and simultaneous transferred to along its pathway, which can be considered as a rectification process. As in solar dryers, the input energy during daytime is stored to be recovered during the night period, but that process also helps to stabilize the outlet fluid flow temperature to the drying chamber.

Literature review showed that although sensible heat storage is less energy intensive compared to PCM, it displays advantages as lower HSM cost, no inflammability issues, no hysteresis, lower environmental impact and it is easier to be installed or linked to building facilities [Hasnain, 1998; Flueckiger et al., 2014; Pelay et al., 2017 e Lefebvre and Tezel, 2017]. Moreover, some methods evaluate T3S performance employing complex and time consuming numerical models [Ghoreishi-Madiseh et al, 2017], some are based on try-and-error method [Li et al., 2012; Zanganeh et al, 2014] or evaluate the performance of specific system configuration [Gude et al, 2012], not taking into account the minimization of the HSM

mass nor the more appropriate system geometry. It is worth noticing that some optimization methodologies [Jian et al, 2015] are not generic and need to be processed whenever the system parameters are changed.

The main goal of this work is to present a methodology to optimal design of sensible heat storage systems working as thermal rectifiers when submitted to sinusoidal cyclic outside air temperature, based on the advantages of sensible thermal storage, together with the limitations of the current design methodologies.

4.2 The Lumped Element Model (LEM) applied to the T3S Rectifier

4.2.1 Modeling

The Sensible Thermal Energy Storage System T3S presented in this chapter was meant to operate as a thermal rectifier, designed to soften temperature oscillations from cyclic sources, as depicted in Figure 4.1.

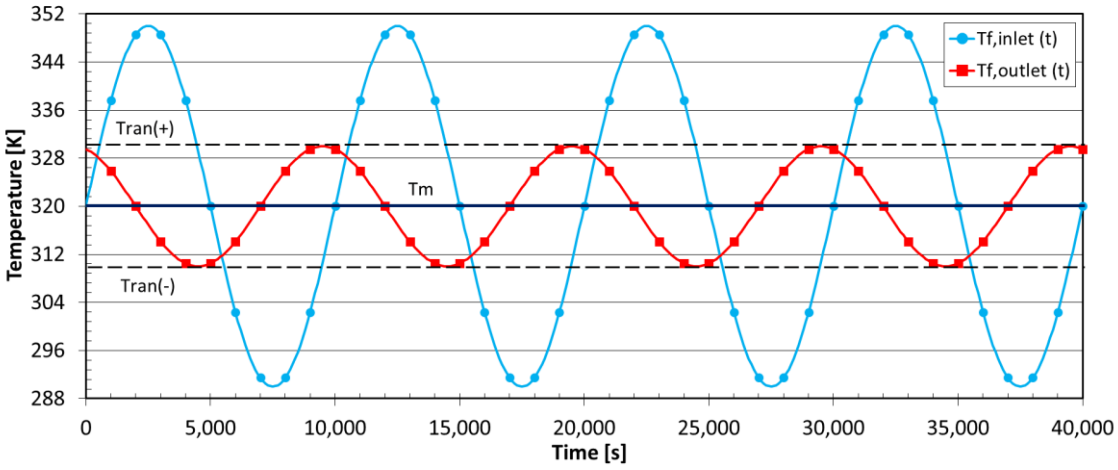

Figure 4.1 – Rectified outlet air temperature (square dot) of a Sensible Thermal Energy Storage System T3S fed by a cyclic thermal source (circle dot).

The system was composed by the Heat Storage Material HSM, distributed in a set of flat parallel plates, and the working fluid, as depicted in Figure 4.2.

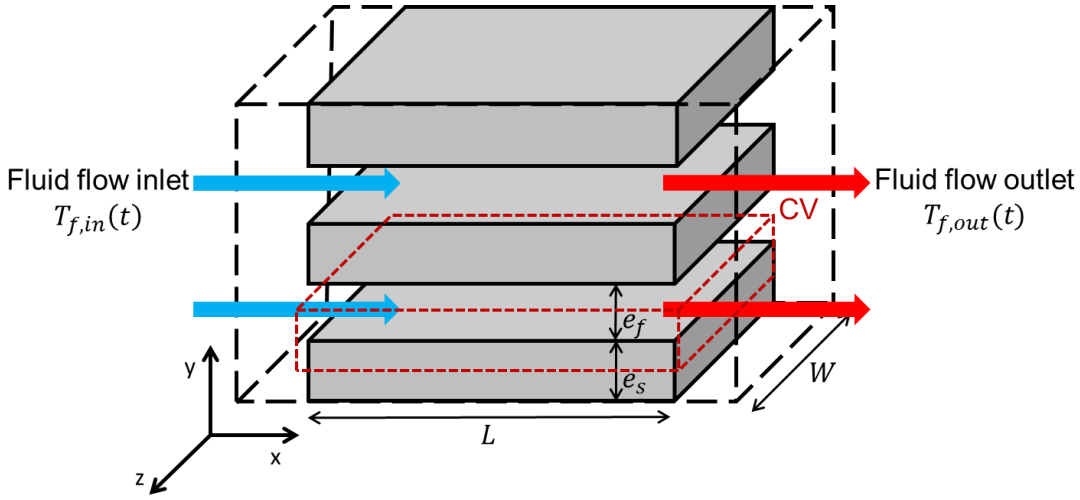

Figure 4.2 –Schematic view of the Sensible Thermal Energy Storage System T3S.

T3S modeling was implemented to a reduced 2D region (Figure 4.3), whose domain was limited to half flat plate $e_s/2$ and half channel $e_f/2$ height, length *L* and unitary width *W*. The symmetric 2D region was divided in *n* independent sections, with individual length *L/n*, for the sake of keeping the model accuracy [Sragovich, 1989; Mawire et al., 2009; Maithani et al., 2013; Duffie and Beckman, 2013; Singh et al., 2009; Mumma and Marvin, 1976 *apud* Singh et al., 2009].

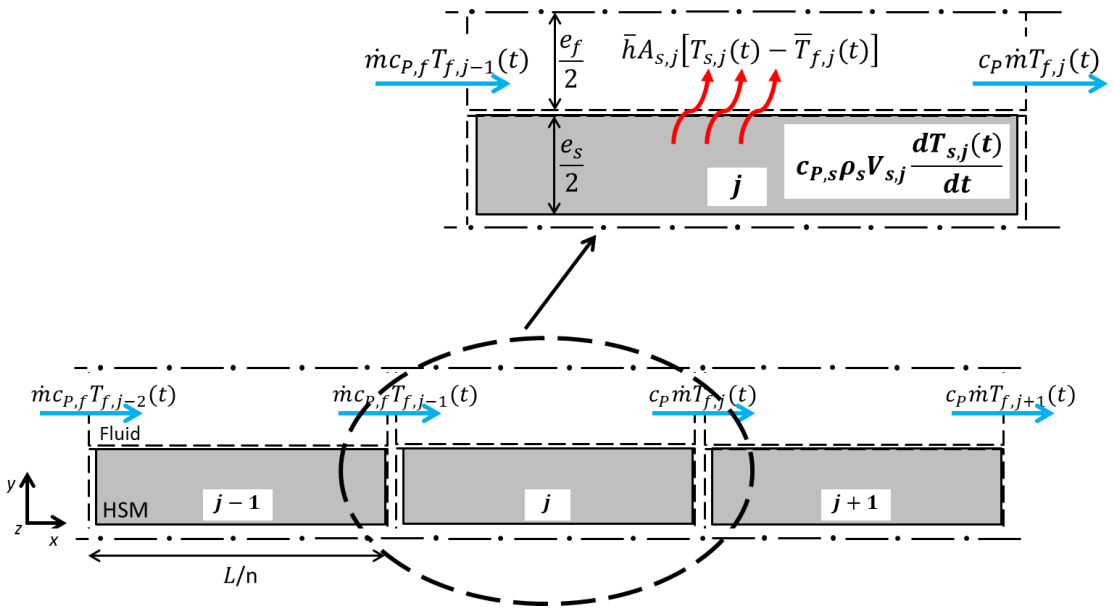

Figure 4.3 – Scheme of the symmetric 2D region with 3 independent sections of length L/n.

Energy balances were written for the coupled solid and fluid control volumes for a given *j* section in order to calculate the system outlet fluid temperature $T_{f,j}(t)$. Working fluid thermal capacitance, defined by the product $M_f c_{p,f}$, is much smaller than the one from HSM, assuming it as non-capacitive [Duffie and Beckman, 2013]. The new system was solved for $T_{f,j}(t)$ by applying the separation of variables technique, as presented on Andriotty, 2015, given by the following equation system.

$$T_{s,j}(t) = T_{s,j}(t-\Delta t) - \left[1 - \ exp\left(-\frac{\bar{h}_j A_{s,j}}{c_{p,s}\,\rho_s\,V_{s,j}}\Delta t\right)\right]\left(T_{s,j}(t-\Delta t) - \overline{T}_{f,j}(t)\right) \tag{4.1}$$

$$T_{f,j}(t) = T_{s,j}(t) - \left[exp\left(-\frac{\bar{h}_j A_{s,j}}{\dot{m} c_{p,f}}\right)\left(T_{s,j}(t) - \ T_{f,j-1}(t)\right)\right] \tag{4.2}$$

Symmetry conditions were imposed to the T3S upper and lower boundaries, leaving heat transfer to occur along the fluid interface with the HSM surface and the mass flow connection to the adjacent sections. The time constant τ and the Number of Transfer Unit NTU [Çengel, 2011] were identified on these equations, rewritten as:

$$T_{s,j}(t) = T_{s,j}(t-\Delta t) - \left[1 - \ exp\left(-\frac{\Delta t}{\tau}\right)\right]\left(T_{s,j}(t-\Delta t) - \overline{T}_{f,j}(t)\right) \tag{4.3}$$

$$T_{f,j}(t) = T_{s,j}(t) - \left[exp\left(-\ NTU_j\right)\left(T_{s,j}(t) - \ T_{f,j-1}(t)\right)\right] \tag{4.4}$$

with $\tau = \frac{c_{p,s}\rho_s V_{s,j}}{h A_{s,j}}$ and $NTU_j = \frac{NTU}{n} = \frac{\bar{h} A_{s,j}}{\dot{m} c_{p,f}}$

The average fluid temperature $\overline{T}_{f,j}(t)$, last term in Equation 4.3, was expressed as the average value between the sections *j* and *j* -1, as follow

$$\overline{T}_{f,j}(t) = \frac{T_{f,j-1}(t) + T_{f,j}(t)}{2} \tag{4.5}$$

The set of Equations 4.3 to 4.5 assembles the Lumped Element Model LEM used to model the T3S. The inlet working fluid temperature $T_{f,in}$ was given by the following sinusoidal function

$$T_{f,in}(t) = T_{f,in(-)} + \left[1 + sen\left(\frac{\pi t}{\beta/2}\right)\right]\left(\left[T_{f,in(+)} - T_{f,in(-)}\right]/2\right) \quad (4.6)$$

with $T_{f,in(+)}$ and $T_{f,in(-)}$ the function upper and lower limits and β its cycle period.

4.2.2 LEM implementation

Simulation was run for a 10 second time step Δt and for the original length L divided into 100 sections. The LEM was performed to find the fluid outlet temperature $T_{f,out}(t)$ at the last section N by following these 6 steps.

1- Calculate the T3S fluid inlet temperature $T_{f,in}(t)$ at time t (Equation 4.6);
2- Perform the fluid temperature $T_{f,j}(t)$ (Equation 4.4) calculation at the outlet of the j^{th} section at time t with the HSM temperature $T_{s,j}(t-1)$ from the prior time $t-1$ (Equation 4.3);
3- Perform arithmetic average fluid temperature $\bar{T}_{f,j}(t)$ (Equation 4.5) from $T_{f,j-1}(t)$ and $T_{f,j}(t)$ for the j^{th} section at time t;
4- Perform the HSM temperature at time t (Equation 4.3) based on the temperature $\bar{T}_{f,j}(t)$ (Equation 4.5) from step 3;
5- Repeat steps 2 to 4 for all j sections for time t;
6- Repeat steps 1 to 5 for the next time step, and carry on the simulation till the end of the total time set to find the fluid outlet temperature $T_{f,out}(t)$ for the problem.

Results were assessed for a quasi-steady regime, reached for a periodic temperature fluctuation around a constant mean value T_m. Calculation was implemented in a Matlab code.

4.3 Inverse Design approach

Inverse design approach consists in determining the system parameters by defining its response behavior, instead of leaving that behavior as the consequence of a direct calculation. In the present work, this philosophy was chosen to propose a design methodology for the T3S with aim to find the minimal HSM mass that satisfies the constraint stablished in Equation 4.7.

$$T_{\mathrm{ran}(-)} < T_{\mathrm{f,out}}(t) < T_{\mathrm{ran}(+)} \tag{4.7}$$

A sensible storage system, with constant and uniform thermophysical properties, submitted to a sinusoidal thermal excitation gives a dynamic sinusoidal response, expressed as a function of the system dimensionless operational temperature θ_{oper}, given by

$$\theta_{oper} = \frac{\left|T_m - T_{f,out(+)}\right|}{\left|T_m - T_{f,in(+)}\right|} \tag{4.8}$$

Equation 4.8 can range from θ_{oper} = 1, meaning that there is no heat transfer between the HSM and the working fluid, as $T_{f,out(+)} = T_{f,in(+)}$, to $\theta_{oper} = 0$ meaning that $T_{f,out(+)} = T_m$. When $T_{f,out(+)} = T_{\mathrm{ran}(+)}$, the T3S reached its designed rectifying duty, expressed by Equation 4.9.

$$\theta_{oper} = \theta_{ran(+)} = \frac{\left|T_m - T_{\mathrm{ran}(+)}\right|}{\left|T_m - T_{f,in(+)}\right|} \tag{4.9}$$

Previous assessments were presented in chapter 2 concerning the T3S depicted in Figure 4.2. The system was optimized to find simultaneously the minimum HSM mass, the best plate length and plate distance that satisfied the rectifying duty $\theta_{ran(+)}$ = 0.133, for several working fluid mass flow rates. Three major conclusions have been taken from that work:

1- The minimum HSM mass and the hA_s product displayed direct correlations, leading to optimum values for NTU and τ, independent from fluid mass flow rate. The plot of θ_{oper}

versus system NTU for different HSM mass *Ms* (Figure 4.4) allows identifying the minimal value for the dimensionless operational parameter θ_{oper} of each system, and graphically indicates the system that satisfies the desired operational condition.

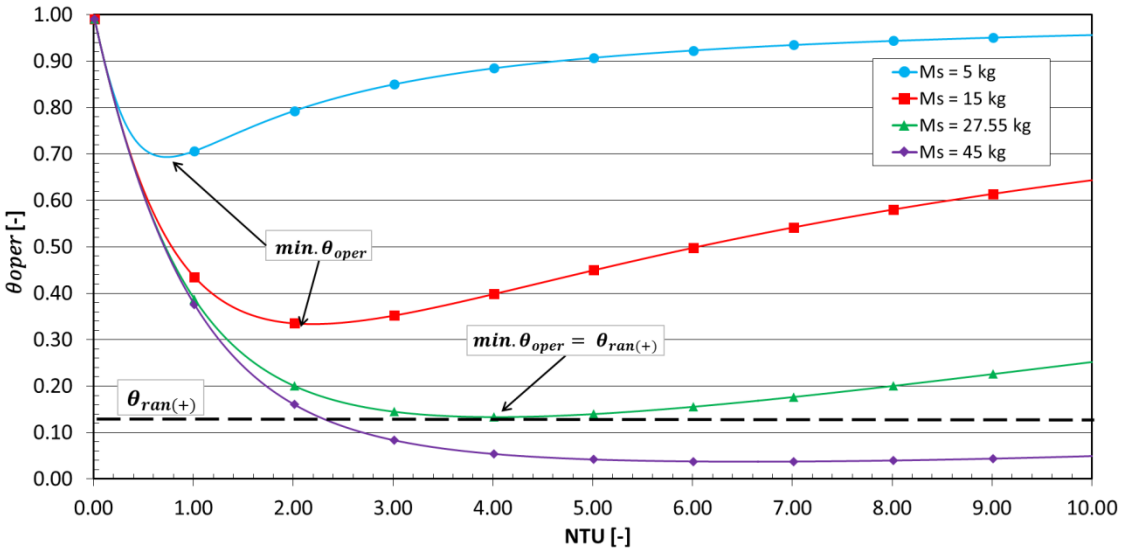

Figure 4.4 - Dimensionless operation temperature as a function of NTU for different HSM mass ($\dot{m} = 0.001$ kg/s and $\beta = 20{,}000\ s$).

Smaller NTU values led to lower heat transfer rates, which means that the outlet fluid temperature is almost the same as the inlet. For greater NTU values, the heat transfer is more intense and consequently more difficult to control (Chapter 2).

2- The optimal NTU, the one that satisfies the minimum HSM mass, is in fact an infinite combination of superficial area A_s and heat transfer coefficient $\bar{h}$. The A_s and $\bar{h}$ combinations can be expressed as a Pareto front [Stiglitz, 1981; Luenberger, 1992 e Tomoiagă et al., 2013] as displayed in Figure 4.5.

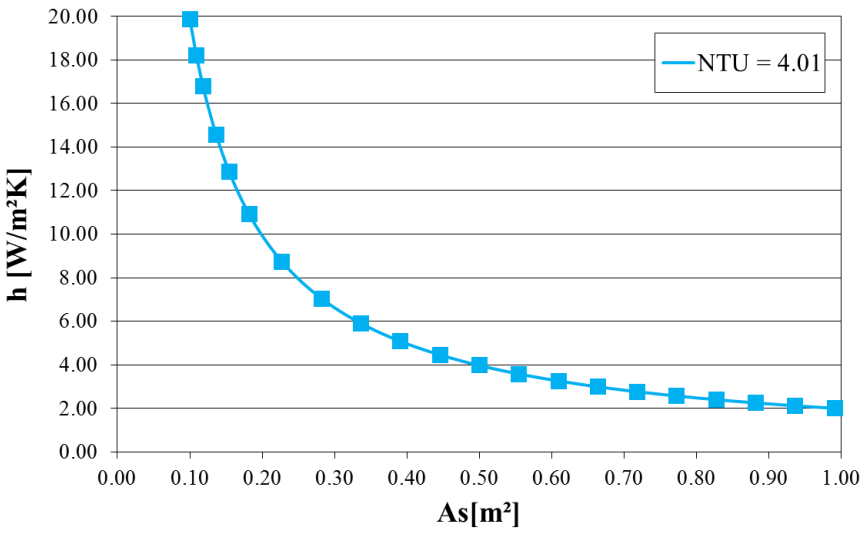

Figure 4.5 – Heat transfer coefficient $\bar{h}$ and superficial area A_s as a Pareto front for a T3S with NTU = 4.01 ($\dot{m} = 0.001$ kg/s).

All values along that Pareto front are system Pareto optimal. Any outside value mean that the HSM mass would not guarantee the maximal T3S rectifying capacity, as presented in Figure 4.4.

3- Same behavior can be identified in respect to the optimal time constant τ, with common dependent parameters in respect to NTU.

Based on those behaviors, a T3S design methodology was proposed as a function of the combination of the system NTU, time constant τ and $\theta_{ran(+)}$. NTU and HSM mass were chosen as optimization parameters, and τ can be obtained from NTU results by post-processing.

Air and HSM properties were taken as constant and uniform (Table 4.1). It is worth noticing that HSM thermal conductivity is not taken into account on the LEM approach.

Table 4.1 - Properties of Air and HSM @ 320 K [Bergman et al., 2011].

	Density ρ [kg/m³]	Specific heat c_p [J/(kgK)]	Dynamic viscosity μ [kg/(ms)]	Prandtl number Pr [-]	Thermal conductivity k [W/(mK)]
Fluid (Air)	1.103	1,008	1.949 E-5	0.705	2.785 E-2
HSM (AISI 304)	7,900	477.00	-	-	14.9

The one-factor-at-a-time OFAT [Montgomery, 2013] strategy was used to individually analyze mass flow rate $\dot{m}$, period β and the designed rectifying duty $\theta_{ran(+)}$, displayed in Table 4.2, organized in 3 procedures.

Table 4.2 - T3S parameters bounds for the proposed procedures ($T_m = 320$ K).

Procedures *p*	Input	Minimum	Maximum	Increment	Levels *i*
1*	$\dot{m}$ [kg/s]	0.001	0.005	0.001	5
2	β [s]	4,000	20,000	4,000	5
3	$\theta_{ran(+)}$ [-]	0.066	0.933	0.066	14
Optimized variables					
NTU [-]		0.01	10.00	0.01	
HSM mass M_s [kg]		0.001	Unconstrained	0.001	
Related restrictions					
1	$\beta = 20{,}000\ s$ and $\theta_{ran(+)} = 0.133$				
2	$\dot{m} = 0.001\ kg/s$ and $\theta_{ran(+)} = 0.133$				
3	$\dot{m} = 0.001\ kg/s$ and $\beta = 20{,}000\ s$				

* Chapter 2.

Calculations were performed for different increments (Table 4.2), following the line search strategy [Boyd, 2004; Sun and Yuan, 2006] in respect to the *p* procedures in order to assemble the R_p matrices, as depicted in Figure 4.6. The solutions for each level *i* of each procedure *p* from the R_p matrices are presented next section.

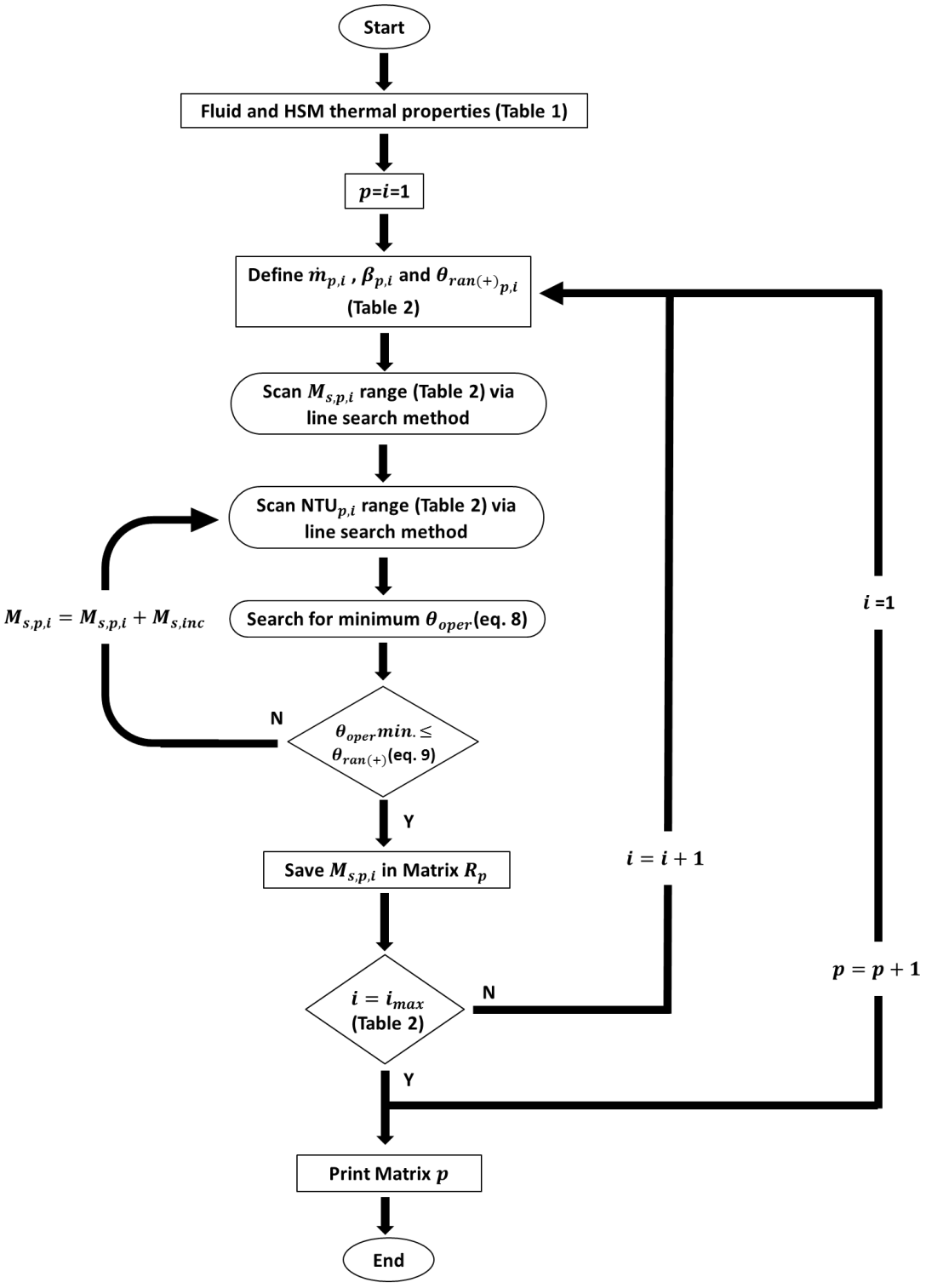

Figure 4.6 – Minimum HSM mass search algorithm based on the one-factor-at-a-time OFAT approach for mass flow rate $\dot{m}$, period β and the designed rectifying duty $\theta_{ran(+)}$ for a range of HSM mass M_s and NTU values.

4.4 Results

4.4.1 Overall results

Tables 4.3 to 4.5 present results for NTU, Ms_{min} and τ obtained with procedures 1 to 3, respectively.

Table 4.3 - NTU, Ms_{min} and τ for 5 levels of mass flow rate $\dot{m}$ (Procedure p=1).

Level	Mass flow rate $\dot{m}$ [kg/s]	NTU [-]	Ms_{min} [kg]	τ [10^3 s]
1	0.001	4.01	27.15	3.204
2	0.002	4.02	54.30	3.196
3	0.003	4.02	81.45	3.196
4	0.004	4.02	108.61	3.196
5	0.005	4.03	135.76	3.188

Mass flow rate and the HSM minimum mass displayed a linear dependency, whereas NTU and τ can be considered as constant. The maximum 0.5% deviation from the optimal NTU and τ values can be considered as numerical fluctuations, due to the line search strategy and parameters bounds (Table 4.2).

Table 4.4 - NTU, Ms_{min} and τ for 5 levels of period β (Procedure p=2).

Level	Period β [s]	NTU [-]	Ms_{min} [kg]	τ [10^3 s]
1	4,000	3.97	5.46	0.651
2	8,000	3.98	10.88	1.294
3	12,000	4.02	16.30	1.919
4	16,000	4.01	21.70	2.564
5	20,000	4.01	27.15	3.204

Both Ms_{min} and τ displayed a linear dependency with period β, while NTU can be considered as constant. Figure 4.7 brings the time evolution of the fluid outlet temperature

$T_{f,out}$ and the half plate length (L/2) temperature predicted for procedures and levels (p=1; i=1), (p=1; i=2) and (p=2; i=1).

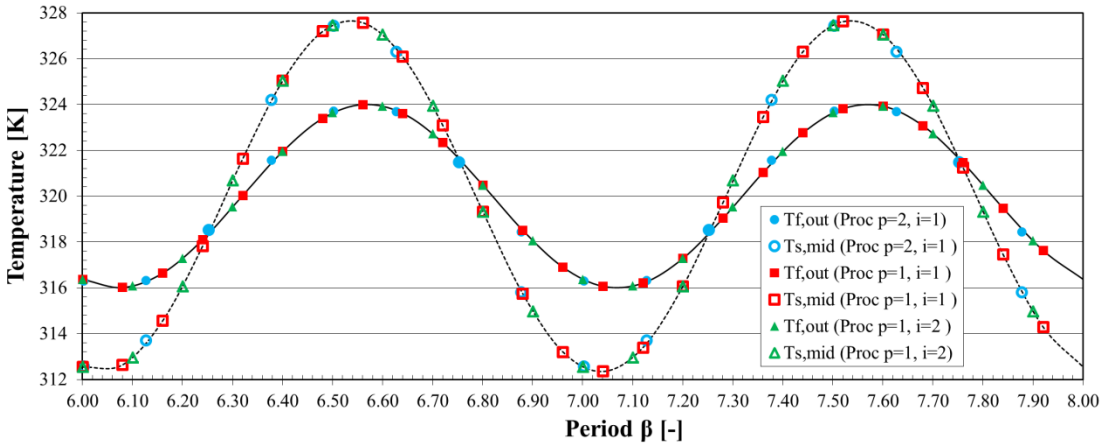

Figure 4.7 – Time evolution of fluid outlet temperature $T_{f,out}$ and HSM half plate length temperature $T_{s,mid}$ (L/2).

These three cases were selected due to proportional relations such as $\dot{m}_{1,2} = \dot{m}_{2,1} = 2\dot{m}_{1,1}$ and $\beta_{1,1} = \beta_{1,2} = 5\beta_{2,1}$. It can be noticed that the fluid outlet temperature were similar for the 3 cases, as well as for the HSM half plate length (L/2) temperature, meaning that the T3S optimization converged to the same optimal temperatures field for a given designed rectifying duty, *e. g.*, $\theta_{ran(+)} = 0.133$. Looking back to Equations 4.3 and 4.4, it can be stated that any change in the parameters that compose NTU or τ demands the remaining ones to be changed in order to follow the same fluid and HSM half plate length temperatures. As an example, the HSM minimum mass was increased in a factor of 10 from (p=2; i=1) to (p=1; i=2), following the same behavior of the mass flow rate to period product. This observation allows to generalize the T3S behavior as a function of NTU and τ.

Results for the designed rectifying duty $\theta_{ran(+)}$ (Procedure p=3) are presented in Table 4.5.

Table 4.5 - NTU, Ms_{min} and τ for 14 levels of the designed rectifying duty $\theta_{ran(+)}$ (Procedure p=3)

Level	$\theta_{ran(+)}$ [-]	NTU [-]	Ms_{min} [kg]	τ [10^3 s]
1	0.933	0.140	0.929	3.141
2	0.867	0.280	1.927	3.257
3	0.800	0.450	3.005	3.159
4	0.733	0.620	4.177	3.187
5	0.667	0.810	5.460	3.189
6	0.600	1.010	6.879	3.223
7	0.533	1.250	8.465	3.204
8	0.467	1.520	10.263	3.195
9	0.400	1.830	12.339	3.190
10	0.333	2.200	14.795	3.182
11	0.267	2.630	17.801	3.202
12	0.200	3.210	21.675	3.195
13	0.133	4.020	27.137	3.194
14	0.067	5.400	36.477	3.196

The smaller the designed rectifying duty $\theta_{ran(+)}$, the bigger amount of heat must be transferred by the HSM, making its minimum mass and NTU to increase. NTU is strongly dependent of $\theta_{ran(+)}$, whereas τ is not, as its 3.5% deviation allows to consider it as constant.

4.4.2 Generalization

Qualitative trends for NTU, Ms_{min} and τ as a function of the mass flow rate $\dot{m}$, period β and designed rectification duty $\theta_{ran(+)}$ are summarized in Table 4.6.

Table 4.6 – Qualitative behavior of NTU, Ms_{min} and τ in respect to the T3S input parameters.

Parameters	NTU [-]	Ms_{min} [kg]	τ [s]
Mass flow rate $\dot{m}$	Constant	Directly proportional	Constant
Period β	Constant	Directly proportional	Directly proportional
Design rectifying duty $\theta_{ran(+)}$	Non-linear association	Non-linear association	Approx. constant

Fitting curves were proposed to express the NTU (Equation 4.10) and τ (Equation 4.11) behavior of the T3S submitted to a sinusoidal temperature input.

$$NTU(\theta_{ran(+)}) = -1.996ln\left[\theta_{ran(+)}\right] \tag{4.10}$$

$$\tau(\beta) = 3{,}196\left(\frac{\beta}{20{,}000}\right) \tag{4.11}$$

With these fitting curves, any T3S under that input restriction can be designed to operate for a given $\theta_{ran(+)}$, with the minimum HSM mass. Both NTU and τ followed a Pareto front, with an infinity combination of system parameters. In order to obtain the T3S geometry, based on fitting curves Equations 4.10 and 4.11, next section details a step-by-step sequence for the proposed design methodology. It is worth noticing that the fitting curves Equations 4.10 and 4.11 can be used to compose different designs methodologies.

4.5 Step-by step sequence

4.5.1 Input conditions

Heat transfer coefficient $\bar{h}$ was calculated for the average laminar flow Nusselt correlation $\overline{Nu}_{D_h}$ for infinite parallel flat plates [Stephan, 1959 *apud* Bejan, 2013] with air as the working fluid (Table 4.1)

$$\overline{Nu}_{D_h} = \left(\frac{\bar{h}\, D_h}{k_f}\right)_j = 7.55 + \frac{0.024 L_*^{-1.14}}{1+0.0358 Pr_f^{0.17} L_*^{-0.64}} \qquad 0.1 \leq Pr_f \leq 1000 \qquad (4.12)$$

with the hydraulic diameter D_h, the dimensionless length L_* at the thermal entry region and the Reynolds number Re_{D_h} defined by:

$$L_* = \frac{L}{D_h Re_{D_h} Pr_f}, \qquad \text{with} \quad D_h = 2e_f \text{ and } Re_{D_h} = \frac{\rho_f u_f D_h}{\mu_f} \qquad (4.13)$$

Figure 4.8 presents a 3 step-by-step sequence to find the T3S geometric dimensions (plate length L, thickness e_s and distance e_f) according to operational conditions as mass flow rate $\dot{m}$, design rectifying duty $\theta_{ran(+)}$ and period β, for a given HSM.

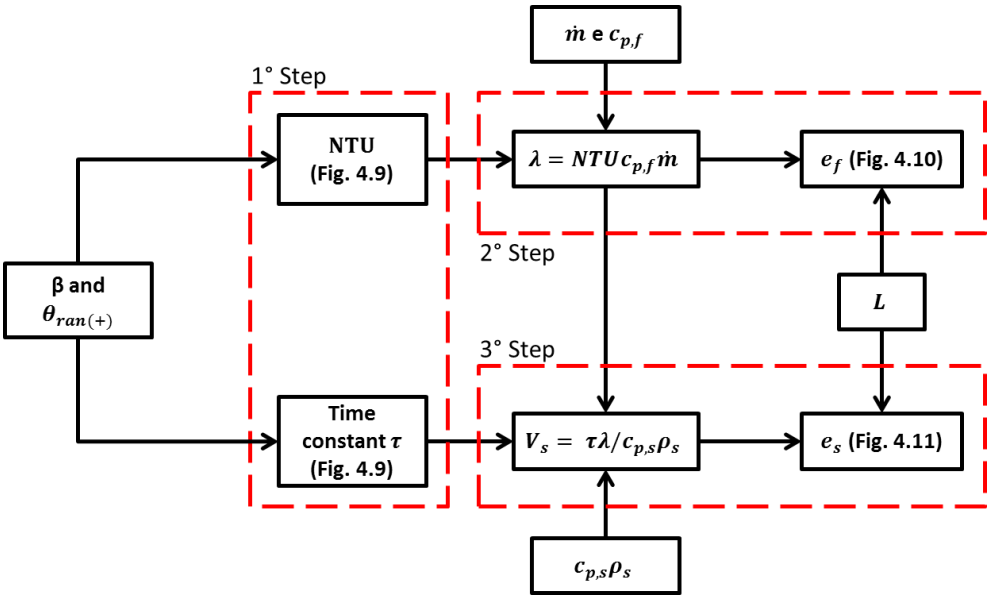

Figure 4.8 – Proposed methodology to design a T3S.

First definition comes from setting the period β and the design rectifying duty $\theta_{ran(+)}$, that allows finding τ and NTU in Figure 4.9. Step 2 defines $\lambda = NTUc_{p,f}\dot{m}$, with the optimal value for NTU, air specific heat and mass flow rate per channel.

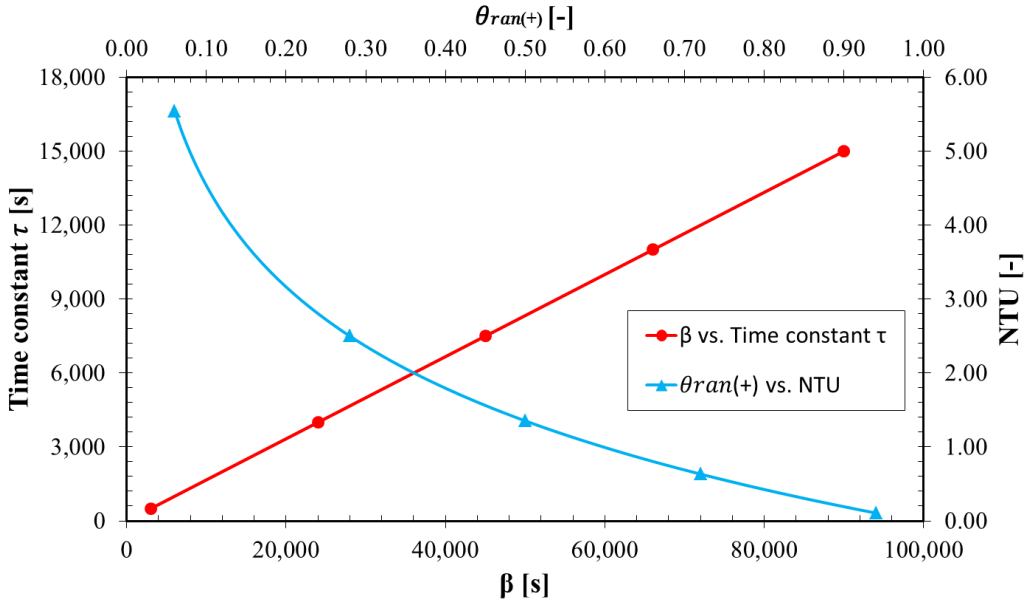

Figure 4.9 – Time constant τ and NTU selection graph according to β and $\theta_{ran(+)}$ settings.

Figure 4.10 allows selecting the optimal distance e_f, by the aid of λ, at the x axis. Its value intercepts several plate length L curves, and the chosen one gives the optimal distance e_f at the y axis.

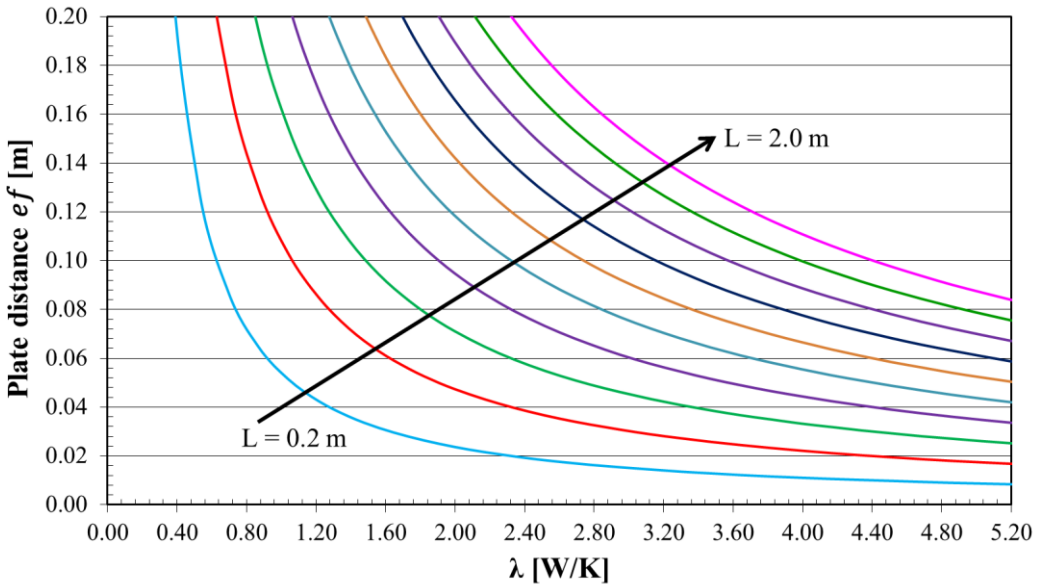

Figure 4.10 - Plate distance e_f selection graph as a function of the design parameter λ and plate length L.

Finally, step 3 aims to find the HMS volume $V_s = \tau\lambda/c_{p,s}\rho_s$, based on the optimal values of τ (Step 1), λ (Step 2) and material proprieties. Volume V_s and plate length L define the plate thickness e_s, as shown in Figura 4.11.

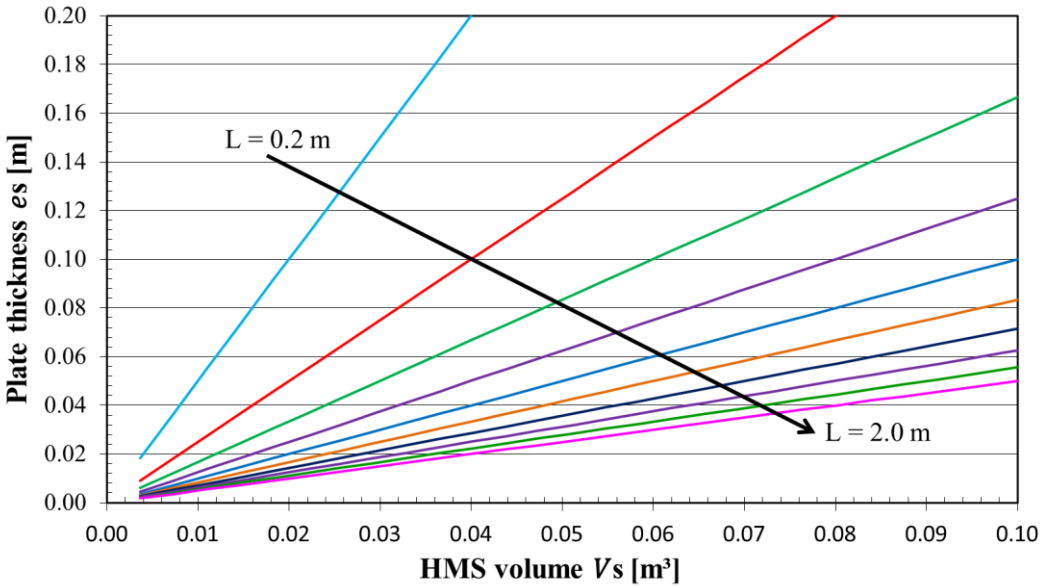

Figure 4.11 - Plate thickness e_s selection graph as a function of the HMS volume V_s and plate length L.

All calculations may be performed with the aid of Equations 4.10 and 4.11, without the last 3 figures, but it will need the help of a nonlinear solution software. New figures must be built for working fluids different than air or for air properties different than those on Table 4.1, as the convective heat transfer correlations may change.

4.5.2 Case study

Tests were proposed to give a methodology overview, compared to CFD simulations [STAR-CCM+ Manual, 2017]. That last software considers air proprieties as temperature dependent, as presented in Table 4.7. Specific heat was taken as constant due to its weak dependency for the simulated range of temperatures. Air properties for LEM were based on values from Table 4.1.

Table 4.7 – Polynomial fit for air thermophysical properties for the temperature range of 150 K to 3,000 K [Zografos, 1987].

Properties	Polynomial fit
Density ρ_f [kg/m³]	$345.57(T-2.6884)^{-1}$
Thermal conductivity k_f [W/(mK)]	$1.5797x10^{-17}T^5 + 9.46x10^{-14}T^4 + 2.2012x10^{-10}T^3 - 2.3758x10^{-7}T^2 + 1.7082x10^{-4}T - 7.488x10^{-3}$
Dynamic viscosity μ_f [kg/(ms)]	$2.5914x10^{-15}T^3 - 1.4346x10^{-11}T^2 + 5.0523x10^{-8}T + 4.1130x10^{-6}$
Specific heat $c_{p,f}$ [J/(kgK)]	Constant; 1,008

HSM density ρ_s and HSM specific heat $c_{p,s}$ were defined for each test and then assumed as constant and uniform. HSM thermal conductivity *k* was taken as unitary (1 $Wm^{-1}K^{-1}$), to respect LEM modeling restrictions (Chapter 2). Table 4.8 presents input data and operational conditions for 3 test cases.

Table 4.8 – Performed test cases for LEM and CFD comparison

T3S operation parameters	Test 1	Test 2	Test 3
Mass flow ṁ [kg/s]	0.002	0.002	0.008
Inlet sine period β [s]	40,000	30,000	30,000
Senoid central temperature T_m [K]	320.00	350.00	400.00
Inlet senoid upper temperature $T_{f,in(+)}$	370.00	360.00	440.00
Designed outlet senoid upper temperature $T_{\mathrm{ran}(+)}$	340.00	353.00	430.00
HSM density ρ_s [kg/m³]	1,000	2,000	3,000
HSM specific heat $c_{p,s}$ [J/(kgK)]	900	400	300

T3S dimensions are reported in Table 4.9, calculated by the design proposed methodology.

Table 4.9 - Parameters and dimensions for the 3 test cases calculated by the proposed design methodology.

T3S dimensions	Test 1	Test 2	Test 3
Plate length L [m]	0.4	0.8	1.0
Plate distance e_f [m]	0.0248	0.0364	0.0466
Plate thickness e_s [m]	0.06756	0.0363	0.02545
T3S parameters			
Dimensionless temperature $\theta_{ran(+)}$ [-]	0.4	0.3	0.75
NTU [-]	1.789	2.34	0.57
Time constant τ [s]	6,684	4,912	5,000
λ [w/K]	3.606	4.717	4.596
V_s [m³]	0.02678	0.02896	0.02553

Results in respect to the Maximal outlet temperature are presented in Table 4.10. All results displayed relative deviations below 1.5%.

Table 4.10 - Values for the design maximal outlet temperature and the ones predicted from LEM and CFD methods for the 3 test cases.

Maximal outlet temperature	Test 1	Test 2	Test 3
Design	340.00	353.00	430.00
LEM	339.42	352.99	429.80
CFD	340.33	353.10	430.48

Figure 4.12 brings Test 3 results to show how the T3S proposed design methodology arrived to ensure the rectifying capacity duty.

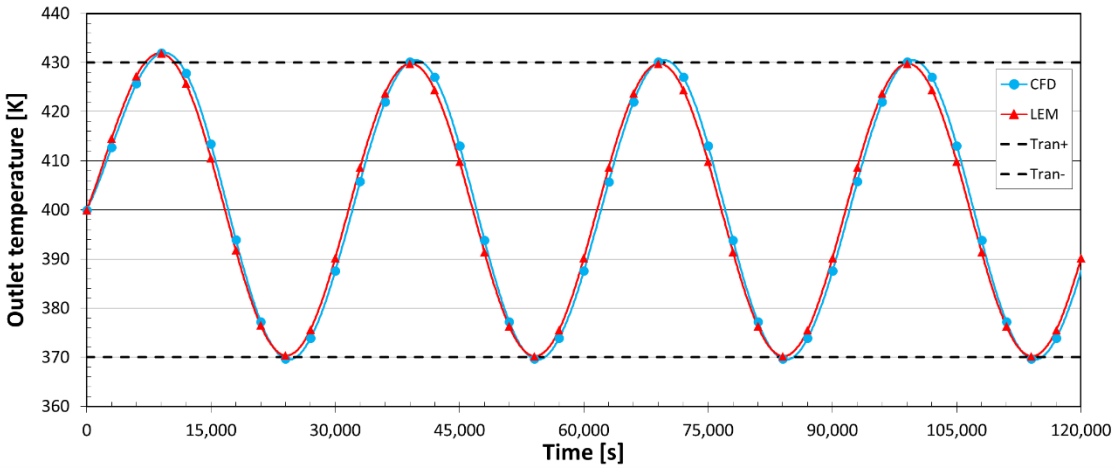

Figure 4.12 – T3S outlet air temperature $T_{f,out}$ for Test 3 from LEM and CFD simulation.

Results presented very little deviation from CFD, LEM and the rectifying capacity duty, and showed the suitability of the proposed design methodology to simulate heat storage under cyclic conditions, within the method validity range.

4.6 Conclusions

This paper presented and discussed a methodology to design Sensible Thermal Energy Storage System T3S based on Lumped Element Models LEM, meant to work as a thermal rectifier. LEM is a simplified and low time consuming approach that can replace more sophisticated ones, like CFD solutions, within a range of well-known restrictions.

The T3S was composed by a set of flat parallel plates, the Heat Storage Material HSM, separated by narrow channels, where an induced fluid stream carries the exchanged energy of the system. A sinusoidal cyclic inlet temperature flow was imposed to the system and a continuous outlet was obtained within a narrow limit range of temperature values, which characterized the system as a thermal rectifier.

The methodology was based on Inverse Design approach and searched for the minimization of the HSM mass capable to restrain the outlet temperature to the operational range. The optimization algorithm implies on a large number of calls of the user function, also known as the direct solution, which is time consuming, especially if that direct solution was

based on CFD models, and justified the search for more rapid but still accurate models, like LEM. Scale analysis revealed that the Number of Transfer Unit NTU and time constant τ can describe the T3S thermal behavior, whose respective dependency are the design rectifying duty and the inlet temperature period.

A step-by-step sequence to the proposed design methodology was presented and detailed. Any future user can choose from using fitted curves for Number of Transfer Unit NTU and time constant τ calculation, together with some extra relations, or follow a sequence of detailed graphs to reach the T3S design that respects the operational outlet temperature range.

The proposed design methodology solution was compared to CFD simulations and results showed little deviations among them, whenever LEM respected the modeling restrictions, with values below 1.5% for the tested cases.

In conclusion, any T3S operating as a thermal rectifier, submitted to a sinusoidal cyclic temperature input and with constant and uniform HSM and fluid properties, can be designed with the NTU and τ fitting curves. The resulting T3S configuration will guaranteed the outlet fluid temperature within the operational range using the minimum HSM mass.

5 CONCLUSÃO

O T3S foi definido pelo HSM, disposto em um conjunto de placas planas paralelas, pelo escoamento do fluido de trabalho, ar, e submetido a fontes de calor cíclicas. A abordagem escolhida para modelar o T3S foi uma formulação *Lumped* capaz de representar as principais características do problema de acumulação sensível: a geometria, as propriedades do material de acumulação e a energia térmica carregada pelo fluido. A formulação *Lumped* foi escolhida, pois a otimização do T3S requereu centenas de milhões de chamadas da rotina de cálculo, o que justificou sua utilização em termos de tempo computacional. O procedimento de otimização combinou as estratégias *one-factor-at-a-time* OFAT (Montgomery, 2013) e *line search* (Boyd, 2004; Sun e Yuan, 2006). A otimização do sistema foi baseada em projeto inverso, visando obter uma saída condicionada com a menor massa de HSM possível. A metodologia de dimensionamento determina as propriedades do HSM e qual a disposição desta massa que garante a saída condicionada.

A validade do modelo LEM foi verificada no Capítulo 2 através de simulações pelo método de volumes finitos CFD. A amplitude e a fase da temperatura do fluido na saída do T3S foram utilizadas para verificar os desvios entre os modelos LEM e CFD. Nove fatores do T3S foram selecionados para realizar esta avaliação: comprimento das placas, distância entre as placas, espessura das placas, condutividade térmica do HSM, densidade do HSM, calor específico do HSM, amplitude e período da temperatura do ar na entrada do T3S e vazão mássica de ar. A técnica de planejamento de experimentos Box-Behnken foi escolhida para analisar o comportamento multivariável do sistema, resultando em 130 casos para comparação. Foi observado que os desvios para a amplitude foram inferiores a 2% em aproximadamente 80% dos casos simulados, enquanto os desvios para o deslocamento de fase não ultrapassaram 4%, com apenas um caso fora desse valor. Estes resultados mostraram que o LEM é capaz de descrever sistemas de acumulação de calor sensível, desde que sejam respeitadas as restrições do modelo.

Após esta verificação, o método de otimização foi aplicado ao T3S no Capítulo 3 para encontrar a menor massa de HSM que garantisse uma determinada capacidade de retificação projetada, para diversas vazões mássicas. Foi aplicado o método de busca exaustiva para obter a disposição ótima da massa de HSM (comprimento e distância entre as placas). Os resultados mostraram que, para uma determinada massa de HSM, existe uma infinidade de combinações de comprimento e distância entre as placas que otimizam a capacidade de retificação do T3S. Mais significativo: todas estas infinitas combinações convergiram para valores constantes do NTU e da constante de tempo, independente da vazão mássica de ar. Para a capacidade de

retificação projetada de 0,133, os valores ótimos do NTU e da constante de tempo foram 4,03 e 3.230s, respectivamente.

A partir destas constatações, a análise do T3S retificador foi expandida no Capítulo 4 para diferentes capacidades de retificação do sistema e períodos dos ciclos da temperatura do fluido na entrada. Foi observado que o valor ótimo do NTU é função somente da capacidade de retificação do T3S, enquanto a constante de tempo ótima é diretamente proporcional ao período. Duas curvas de ajuste, uma para o NTU e outra para a constante de tempo, foram construídas e utilizadas para propor uma metodologia de dimensionamento para o T3S via projeto inverso. A metodologia de dimensionamento foi apresentada em uma sequência de três passos, utilizando gráficos para uma melhor visualização da metodologia. Seguindo esta sequência de passos, obteve-se o comprimento da placa, a espessura da placa e a distância entre as placas que garantiram a capacidade de retificação projetada. Estas dimensões do T3S obtidas com a metodologia de dimensionamento proposta foram simuladas em um software CFD para verificar se a capacidade de retificação projetada foi realmente atendida. O maior desvio entre os casos analisados foi inferior a 1,5%, demonstrando que a metodologia de dimensionamento proposta atendeu ao requisito de retificação projetado.

Com relação ao estado da arte, a Tabela 5.1 apresenta uma comparação entre as contribuições de alguns trabalhos existentes na literatura e os desta Tese:

Tabela 5.1 – Comparativo da contribuição da presente Tese para o estado da arte.

Autores / ***Parâm. T3S***	Gude et al., 2012	Ghoreishi-Madiseh et al., 2017	Sragovich, 1989	Li et al., 2012	Schmidt et al, 1977	Jian et al., 2015	Tese
HSM sensível	✓	✓	✓	✓	✓	✓	✓
Fluido (ar)		✓	✓		✓	✓	✓
Cíclico	✓	✓		✓		✓	✓
Met. Dimens.							
Simples			✓		✓		✓
Mim. massa						✓	✓
Otim. restrita[5]			✓	✓	✓	✓	✓
Otim. geral[6]				✓	✓		✓

[5] Otim. restrita: o T3S foi otimizado, mas se algun parâmetro for alterado, é necessário otimizar novamente.

[6] Otim. geral: mesmo alterando-se parâmetros do sistema, não há necessaidade de otimizá-lo novamente.

Resumidamente, a presente Tese contribuiu para o estado da arte com:

- A verificação dos desvios de um modelo simplificado para descrever sistemas de acumulação de calor sensível operando como retificadores térmicos

- A demonstração que a capacidade de retificação de uma determinada massa de HSM é maximizada pelos valores ótimos do NTU e da constante de tempo.

- Uma metodologia de dimensionamento capaz de determinar a melhor geometria do T3S que assegura a capacidade de retificação projetada.

5.1 Trabalhos futuros

Para trabalhos futuros, propõe-se:

- Aplicar a metodologia de otimização para outras funções de entrada (triangular, Heaviside, trapezoidal, etc.).

- Analisar os desvios da generalização dos resultados ótimos para funções "comportadas" (senoide, Heaviside, etc.) e para situações reais (gases de exaustão de um processo industrial, secador solar, etc.).

- Mostrar que os resultados obtidos no capítulo 4 podem ser aplicados para outras geometrias (leito de esferas, cilindros, etc.) e verificar os desvios decorrentes deste procedimento.

- Aplicar a metodologia de dimensionamento, baseada nas curvas ótimas do NTU e constante de tempo, em uma aplicação real.

- Alterar o equacionamento para descrever materiais de troca de fase PCM e verificar se uma metodologia de dimensionamento similar a proposta nesta Tese pode ser elaborada.

REFERÊNCIAS BIBLIOGRÁFICAS

Aguilar-Jiménez, J. A., Velázquez, N. e Acuña, A. Techno-economic analysis of a hybrid PV-CSP system with thermal energy storage applied to isolated microgrids. **Solar Energy**, vol. 174, p. 55–65, 2018.

Andriotty, T. H. **Otimização de estruturas para acumulação de calor sensível**. Dissertação de mestrado, Universidade Federal do Rio Grande do Sul, 2014.

Andriotty, T. H., Rodrigues, L. J., Rocha, L. A. O. e Schneider, P. S., Optimization of a Sensible Thermal Storage System by a Lumped Approach, **Defect and Diffusion Forum**, vol. 366, p. 182–191, 2016.

Andriotty, T. H., Rodrigues, L. J., Rocha, L. A. O. e Schneider, P. S. Lumped methodology applied to sensible thermal storage systems. **Proceedings of ECOS 2015 - the 28th international conference on Efficiency, Cost, Optimization, Simulation and environmental impact of energy systems**, June 30 - July 3, 2015, Pau, France.

Ayyappan, S., Mayilsamy, K. e Sreenarayanan, VOL. VOL. Performance improvement studies in a solar greenhouse drier using sensible heat storage materials. **Heat and Mass Transfer**, vol. 52, n. 3, p. 459–467, 2016.

Bal, L. M., Satya, S. e Naik, S. N. Solar dryer with thermal energy storage systems for drying agricultural food products: a review. **Renewable and Sustainable Energy Reviews**, vol. 14, n. 8, p. 2298–2314, 2010.

Bejan, A., Convection Heat Transfer, 4th edition, New Jersey, John Wiley & Sons, INC., p. 135, 2013.

Bergman, T. L., Incropera, F. P., Dewitt, D. P. e Lavine, A. S. Fundamentals of heat and mass transfer. New Jersey: John Wiley & Sons, 2011.

Boyd, S. e Vandenberghe L. Convex optimization. Cambridge university press, 2004.

Cabeza, L. F., Castell, A., Barreneche, C. D, De Gracia, A. e Fernández, A. I. Materials used as PCM in thermal energy storage in buildings: a review. **Renewable and Sustainable Energy Reviews**, vol. 15, n. 3, p. 1675–1695, 2011.

Campo, A. e Herranz, L. E.. Expanded Lumped Model for the Algebraic Evaluation of the Total Heat Rejection from a Large Plate Immersed in a Fluid during a Period of Time, **Heat Transfer Research**, vol. 40, no. 4, p. 305-319, 2009.

Celik, I. B., Ghia, U., Roache, P. J., Freitas, C. J., Coleman, H. e Raad, P. E. Procedure for estimation and reporting of uncertainty due to discretization in CFD applications, **Journal of Fluids Engineering**, vol. 130, p. 078001-1 – 078001–4, 2008.

Çengel, A. Y. Heat and mass transfer: fundamentals and applications. New York: McGraw-Hill, 2011.

Chauhan, P., Choudhury, C. e Garg, H. Comparative performance of coriander dryer coupled to solar air heater and solar air-heater-cum-rockbed storage. **Applied thermal engineering**, vol. 16, n. 6, p. 475-486, 1996.

Conti, J., Holtberg, P., Diefenderfer, J., LaRose, A.,Turnure, J. T. e Westfall, L. **International energy outlook 2016 with projections to 2040**. USDOE Energy Information Administration (EIA), Washington, DC (United States). Office of Energy Analysis, 2016.

Darzi, A. R., Moosania, S. M., Tan, F. L. e Farhadi, M. Numerical investigation of free-cooling system using plate type PCM storage. **International Communications in Heat and Mass Transfer**, vol. 48, p. 155–163, 2013.

Demir, M. E. e Dincer I. Development and analysis of a new integrated solar energy system with thermal storage for fresh water and power production. **International Journal of Energy Research**,vol. 42, p. 2864–2874, 2018.

Duffie, J. A. e Beckman, W. A., *Solar Engineering of Thermal Processes*, 4th edition, New Jersey, John Wiley & Sons, INC., chapter 8, 2013.

EPE, **Projeção da demanda de energia elétrica**, Rio de Janeiro, Brasil, 2017.

Flueckiger, S. M., Iverson, B. D., Garimella, S. VOL. e Pacheco, J. E. System-level simulation of a solar power tower plant with thermocline thermal energy storage. **Applied Energy**, vol. 113, p. 86–96, 2014.

Ghoreishi-Madiseh, S. A., Sasmito, A. P., Hassani, F. P. e Amiri, L. Performance evaluation of large scale rock-pit seasonal thermal energy storage for application in underground mine ventilation. **Applied Energy**, vol. 185, p. 1940–1947, 2017.

Gude, VOL. G., Nirmalakhandan, N., Deng, S. e Maganti, A. Low temperature desalination using solar collectors augmented by thermal energy storage. **Applied Energy**, vol. 91, n. 1, p. 466–474, 2012.

Hameer, S., Van Niekerk, J. L. A review of large-scale electrical energy storage. **International journal of energy research**, vol. 39, n. 9, p. 1179–1195, 2015.

Hasnain, S. M. Review on sustainable thermal energy storage technologies, Part I: heat storage materials and techniques. **Energy Conversion and Management**, vol. 39, n. 11, p. 1127–1138, 1998a.

Hasnain, S. M. Review on sustainable thermal energy storage technologies, Part II: cool thermal storage. **Energy conversion and management**, vol. 39, n. 11, p. 1139–1153, 1998b.

He, W., Wang, J., Wang, Y., Ding, Y., Chen, H., Wu, Y. e Garvey, S. Study of cycle-to-cycle dynamic characteristics of adiabatic Compressed Air Energy Storage using packed bed Thermal Energy Storage. **Energy**, vol. 141, p. 2120–2134, 2017.

Hughes, P. J. The design and predicted performance of Arlington House. Master thesis, University of Wisconsin-Madison, 1975.

Jian, Y., Falcoz, Q., Neveu, P., Bai, F., Wang, Y. e Wang, Z. Design and optimization of solid thermal energy storage modules for solar thermal power plant applications, **Applied Energy**, vol. 139, p. 30–42, 2015.

Jiang, Y., Li, E., Zhang, X.Q., Wu, Q.G. e Yap, Y. H. Superposition method for the simulation of heat transfer, **International Journal of Heat and Mass Transfer**, vol. 120, p. 914–922, 2018.

Klein, S. A., Beckman, W. A. e Duffie, J. A. A design procedure for solar heating systems. **Solar Energy**, vol. 18(2), p. 113–127, 1976.

Lanahan, M. e Tabares-Velasco, P. C. Seasonal thermal-energy storage: a critical review on BTES systems, modeling, and system design for higher system efficiency. **Energies**, vol. 10, n. 6, p. 743, 2017.

Lefebvre, D. e Tezel, F. H. A review of energy storage technologies with a focus on adsorption thermal energy storage processes for heating applications. **Renewable and Sustainable Energy Reviews**, vol. 67, p. 116–125, 2017.

Li, P., Van Lew, J,, Chan, C., Karaki, W., Stephens J. e O'Brien, J. E. Similarity and generalized analysis of efficiencies of thermal energy storage systems. **Renewable Energy**, vol. 39(1), p. 388–402, 2012.

Luenberger, D. G. New optimality principles for economic efficiency and equilibrium. **Journal of optimization theory and applications**, vol. 75(2), p. 221–264, 1992.

Maithani, R., Patil, A. K. e Saini, J. S., Investigation of effect of stratification on the thermal performance of packed bed solar air heater. **International Journal of Energy Science**, vol. 3, p. 267-275, 2013.

Mawire, A., McPherson, M., Van den Heetkamp, R. R. J. e Mlatho, S. J. P. Simulated performance of storage materials for pebble bed thermal energy storage (TES) systems, **Applied Energy**, vol. 86, p. 1246–1252, 2009.

Merlin, K., Soto, J., Delaunay, D. e Traonvouez, L. Industrial waste heat recovery using an enhanced conductivity latent heat thermal energy storage. **Applied energy**, vol. 183, p. 491–503, 2016.

Minitab Manual, Getting Started with Minitab 18, 2018.

Montgomery, D. C. Design and Analysis of Experiments, 8th edition, John Wiley & Sons, INC., chapter 11, 2013.

Mumma, S. A. e Marvin, W. C. A method of simulating the performance of a pebble bed thermal energy storage and recovery system. American Society of Mechanical Engineers and American Institute of Chemical Engineers, **Heat Transfer Conference**, 1976, Aug. 9-11, *apud* Singh et al., 2009.

Naveira, C. P., Lachi, M., Cotta, R. M.e Padet, J. Hybrid formulation and solution for transient conjugated conduction–external convection, **International Journal of Heat and Mass Transfer**, vol. 52, p. 112–123, 2009.

Nguyen, A., Pasquier, P. e Marcotte, D. Borehole thermal energy storage systems under the influence of groundwater flow and time-varying surface temperature. **Geothermics**, vol. 66, p. 110–118, 2017.

Oró, E., Depoorter, VOL., Pflugradt, N. e Salom, J. Overview of direct air free cooling and thermal energy storage potential energy savings in data centers. **Applied thermal engineering**, vol. 85, p. 100–110, 2015.

Pelay, U., Luo, L., Fan, Y., Stitou, D. e Rood, M. Thermal energy storage systems for concentrated solar power plants. **Renewable and Sustainable Energy Reviews**, vol. 79, p. 82–100, 2017.

Rezaie, B., Reddy, B. VOL. e Rosen, M. A. Thermodynamic analysis and the design of sensible thermal energy storages. **International Journal of Energy Research**, vol. 41(1), p. 39–48, 2017.

Roache, P. J., Perspective: a method for uniform reporting of grid refinement studies. **Journal of Fluids Engineering**, vol. 116, p. 405–405, 1994.

Salomoni, VOL. A., Majorana, C. E., Giannuzzi, G. M., Miliozzi, A., Di Maggio, R., Girardi, F., Mele, D. e Lucentini, M. Thermal storage of sensible heat using concrete modules in solar power plants. **Solar Energy**, vol. 103, p. 303–315, 2014.

Schmidt, F. W., Somers, R. R., Szego, J. e Laananen, D. H. Design optimization of a single fluid, solid sensible heat storage unit. **Journal of Heat Transfer**, vol. 99, p. 174–179, 1977.

Schmidt, F. W. e Szego, J. Transient response of solid sensible heat thermal storage units - Single fluid. **Journal of Heat Transfer**, vol. 98, p. 471–477, 1976.

Schumann, T. E. Heat transfer: a liquid flowing through a porous prism, **Journal of the Franklin Institute**. vol. 208, p. 405–416, 1929.

Singh, R., Saini, R. P. e Saini, J. S. Models for Predicting Thermal Performance of Packed Bed Energy Storage System for Solar Air Heaters - A Review. **Open Fuels & Energy Science Journal**, vol. 2, p. 47–53, 2009.

Smallbone, A., Jülch, VOL., Wardle, R. e Roskilly, A. P. Levelised cost of storage for pumped heat energy storage in comparison with other energy storage technologies. **Energy Conversion and Management**, vol. 152, p. 221–228, 2017.

Souraki, B. A., Assareh, N. e Omidi, M. Effect of internal heat generation on the applicability of different lumped models with unsteady one-dimensional conduction. **Heat Transfer Research**, vol. 45, n. 8, p. 767-793, 2014.

Sragovich, D., Transient analysis for designing and predicting operational performance of a high-temperature sensible thermal-energy storage-system, **Solar energy**, vol. 43(1), p. 7-16, 1989.

Soda M e Beyene A. Multiphase ultra-low grade thermal energy storage for organic Rankine cycle. **International Journal of Energy Research**, vol. 40(1), p. 51–60, 2016.

STAR-CCM+ Manual, CD Adapco, 2017.

Stephan, K. Wärmeübergang und Druckabfall bei nicht ausgebildeter Laminarströmung in Röhren und ebenen Spalten. **Chen. Int. Tech**, vol. 31, p. 773-778, 1959, *apud* Bejan, A., 2004.

Stiglitz, J. E. Pareto optimality and competition. **The Journal of Finance**, vol. 36(2), p. 235–251, 1981.

Suberu, M. Y., Mustafa, M. W. e Bashir, N. Energy storage systems for renewable energy power sector integration and mitigation of intermittency. **Renewable and Sustainable Energy Reviews**, vol. 35, p. 499–514, 2014.

Sun, W. e Yuan, Y. X. Optimization theory and methods: nonlinear programming. New York: Springer Science & Business Media, 2006.

Tomoiagă, B., Chindriş, M., Sumper, A., Sudria-Andreu, A. e Villafafila-Robles, R. Pareto optimal reconfiguration of power distribution systems using a genetic algorithm based on NSGA-II. **Energies**, vol. 6(3), p. 1439–1455, 2013.

Wang, B., Shih, T. -M. e Wu, C. -X. Characteristics of instantaneous heat transfer rates in three heat-transfer-coefficient regimes. **International Journal of Heat and Mass Transfer**, vol. 93, p. 889–895, 2016.

Weitemeyer, S., Kleinhans, D., Vogt, T. e Agert, C. Integration of Renewable Energy Sources in future power systems: The role of storage. **Renewable Energy**, vol. 75, p. 14–20, 2015.

World Bank Group - International Development, Poverty, & Sustainability. http://www.worldbank.org/, 1944. Acesso em: 19-9-2018.

Yuan, S., Zhou, J. e Hu, J., A lumped element method for modeling the two-phase choking flow through hydraulic orifices. **International Journal of Heat and Mass Transfer**, vol. 81, p. 355–361, 2015.

Zanganeh, G., Commerford, M., Haselbacher, A., Pedretti, A. e Steinfeld, A. Stabilization of the outflow temperature of a packed-bed thermal energy storage by combining rocks with phase change materials. **Applied thermal engineering**, vol. 70, n. 1, p. 316–320, 2014.

Zografos, A. I., Martin, W. A. e Sunderland, J. E. Equations of properties as a function of temperature for seven fluids. **Computer Methods in Applied Mechanics and Engineering**, vol. 61(2), p. 177–187, 1987.

APÊNDICE A – Dados e resultados das simulações do Box-Behnken

Tabela A.1 - Dados dos casos simulados em CFD e LEM para o planejamento de experimentos Box-Behnken.

Caso	$\dot{m}$ [kg/s]	β [s]	Amp_{ent} [K]	L [m]	e_s [m]	e_f [m]	k_s [W/mK]	ρ_s [kg/m³]	$c_{p,s}$ [J/kgK]	h [W/m²K]	Bi [-]	NTU [-]	τ [s]
1	0,0105	45.000	10	0,55	0,105	0,2	30,5	4.500	1.000	1,291	0,002	0,067	365.995
2	0,0105	3.600	55	0,55	0,01	0,105	30,5	8.000	650	1,901	0,000	0,099	27.354
3	0,0105	45.000	10	0,55	0,01	0,105	1	4.500	650	1,901	0,010	0,099	15.387
4	0,0105	45.000	55	0,55	0,105	0,105	1	8.000	1.000	1,901	0,100	0,099	441.873
5	0,001	45.000	55	0,55	0,2	0,105	30,5	4.500	1.000	1,11	0,004	0,606	810.811
6	0,0105	45.000	55	0,55	0,105	0,105	30,5	4.500	650	1,901	0,003	0,099	161.560
7	0,0105	86.400	55	0,55	0,2	0,105	30,5	1.000	650	1,901	0,006	0,099	68.385
8	0,0105	45.000	100	0,1	0,105	0,105	30,5	8.000	650	3,983	0,007	0,038	137.083
9	0,001	45.000	55	0,1	0,105	0,105	60	4.500	650	1,532	0,001	0,152	200.473
10	0,0105	3.600	55	0,55	0,105	0,2	60	4.500	650	1,291	0,001	0,067	237.897
11	0,0105	86.400	55	1	0,105	0,105	30,5	4.500	1.000	1,555	0,003	0,147	303.859
12	0,0105	45.000	55	1	0,2	0,2	30,5	4.500	650	1,015	0,003	0,096	576.355
13	0,02	45.000	55	0,55	0,01	0,105	30,5	4.500	300	2,46	0,000	0,067	5.488
14	0,02	45.000	55	0,55	0,105	0,01	30,5	8.000	650	12,662	0,022	0,345	43.121
15	0,001	45.000	55	0,55	0,105	0,01	30,5	8.000	650	10,608	0,018	5,788	51.471
16	0,02	86.400	100	0,55	0,105	0,105	30,5	4.500	650	2,46	0,004	0,067	124.848
17	0,02	45.000	55	0,55	0,105	0,01	30,5	1.000	650	12,662	0,022	0,345	5.390
18	0,0105	86.400	55	0,55	0,105	0,2	60	4.500	650	1,291	0,001	0,067	237.897
19	0,0105	86.400	55	0,55	0,105	0,2	1	4.500	650	1,291	0,068	0,067	237.897
20	0,0105	45.000	10	0,55	0,105	0,2	30,5	4.500	300	1,291	0,002	0,067	109.799
21	0,02	45.000	55	0,55	0,105	0,2	30,5	1.000	650	1,721	0,003	0,047	39.657
22	0,001	45.000	55	1	0,105	0,105	60	4.500	650	1,061	0,001	1,053	289.467

Caso	$\dot{m}$ [kg/s]	β [s]	Amp_{ent} [K]	L [m]	e_s [m]	e_f [m]	k_s [W/mK]	ρ_s [kg/m³]	$c_{p,s}$ [J/kgK]	h [W/m²K]	Bi [-]	NTU [-]	τ [s]
23	0,0105	45.000	55	0,55	0,105	0,105	30,5	4.500	650	1,901	0,003	0,099	161.560
24	0,0105	86.400	55	0,1	0,105	0,105	30,5	4.500	300	3,983	0,007	0,038	35.589
25	0,02	45.000	55	1	0,105	0,105	60	4.500	650	1,934	0,002	0,096	158.803
26	0,0105	45.000	100	0,55	0,105	0,01	30,5	4.500	1.000	11,66	0,020	0,606	40.523
27	0,0105	86.400	55	0,55	0,2	0,105	30,5	1.000	650	1,901	0,006	0,099	68.385
28	0,0105	3.600	55	0,1	0,105	0,105	30,5	4.500	1.000	3,983	0,007	0,038	118.629
29	0,0105	45.000	100	0,55	0,01	0,105	1	4.500	650	1,901	0,010	0,099	15.387
30	0,02	45.000	55	0,55	0,01	0,105	30,5	4.500	1.000	2,46	0,000	0,067	18.293
31	0,0105	3.600	55	0,55	0,105	0,2	1	4.500	650	1,291	0,068	0,067	237.897
32	0,0105	45.000	10	0,55	0,105	0,01	30,5	4.500	1.000	11,66	0,020	0,606	40.523
33	0,0105	45.000	55	1	0,2	0,01	30,5	4.500	650	11,137	0,037	1,052	52.528
34	0,0105	45.000	55	0,55	0,105	0,105	60	8.000	300	1,901	0,002	0,099	132.562
35	0,001	3.600	10	0,55	0,105	0,105	30,5	4.500	650	1,11	0,002	0,606	276.689
36	0,001	86.400	100	0,55	0,105	0,105	30,5	4.500	650	1,11	0,002	0,606	276.689
37	0,0105	45.000	55	0,55	0,105	0,105	60	1.000	1.000	1,901	0,002	0,099	55.234
38	0,0105	3.600	55	0,55	0,2	0,105	30,5	1.000	650	1,901	0,006	0,099	68.385
39	0,0105	45.000	100	0,55	0,2	0,105	60	4.500	650	1,901	0,003	0,099	307.733
40	0,0105	45.000	100	0,55	0,105	0,2	30,5	4.500	300	1,291	0,002	0,067	109.799
41	0,02	45.000	55	0,55	0,2	0,105	30,5	4.500	1.000	2,46	0,008	0,067	365.854
42	0,0105	45.000	100	0,55	0,01	0,105	60	4.500	650	1,901	0,000	0,099	15.387
43	0,0105	45.000	55	0,55	0,105	0,105	30,5	4.500	650	1,901	0,003	0,099	161.560
44	0,001	45.000	55	0,1	0,105	0,105	1	4.500	650	1,532	0,080	0,152	200.473
45	0,0105	3.600	55	1	0,105	0,105	30,5	4.500	300	1,555	0,003	0,147	91.158
46	0,0105	45.000	100	0,55	0,105	0,2	30,5	4.500	1.000	1,291	0,002	0,067	365.995
47	0,0105	45.000	10	1	0,105	0,105	30,5	1.000	650	1,555	0,003	0,147	43.891
48	0,0105	45.000	55	0,55	0,105	0,105	30,5	4.500	650	1,901	0,003	0,099	161.560

Caso	$\dot{m}$ [kg/s]	β [s]	Amp_{ent} [K]	L [m]	e_s [m]	e_f [m]	k_s [W/mK]	ρ_s [kg/m³]	$c_{p,s}$ [J/kgK]	h [W/m²K]	Bi [-]	NTU [-]	τ [s]
49	0,0105	86.400	55	0,55	0,105	0,01	1	4.500	650	11,66	0,612	0,606	26.340
50	0,0105	45.000	55	0,55	0,105	0,105	1	1.000	1.000	1,901	0,100	0,099	55.234
51	0,0105	86.400	55	0,1	0,105	0,105	30,5	4.500	1.000	3,983	0,007	0,038	118.629
52	0,0105	45.000	10	1	0,105	0,105	30,5	8.000	650	1,555	0,003	0,147	351.125
53	0,0105	45.000	10	0,55	0,105	0,2	30,5	4.500	300	1,291	0,002	0,067	109.799
54	0,0105	45.000	100	1	0,105	0,105	30,5	1.000	650	1,555	0,003	0,147	43.891
55	0,001	45.000	55	0,55	0,105	0,01	30,5	1.000	650	10,608	0,018	5,788	6.434
56	0,0105	3.600	55	0,55	0,01	0,105	30,5	1.000	650	1,901	0,000	0,099	3.419
57	0,0105	45.000	55	0,55	0,105	0,105	30,5	4.500	650	1,901	0,003	0,099	161.560
58	0,0105	45.000	55	0,55	0,105	0,105	1	8.000	300	1,901	0,100	0,099	132.562
59	0,0105	3.600	55	0,55	0,2	0,105	30,5	1.000	650	1,901	0,006	0,099	68.385
60	0,0105	45.000	100	0,1	0,105	0,105	30,5	1.000	650	3,983	0,007	0,038	17.135
61	0,0105	45.000	55	0,55	0,105	0,105	30,5	4.500	650	1,901	0,003	0,099	161.560
62	0,0105	45.000	55	1	0,01	0,2	30,5	4.500	650	1,015	0,000	0,096	28.818
63	0,0105	86.400	55	0,55	0,01	0,105	30,5	1.000	650	1,901	0,000	0,099	3.419
64	0,0105	45.000	55	1	0,01	0,01	30,5	4.500	650	11,137	0,002	1,052	2.626
65	0,02	45.000	55	0,55	0,2	0,105	30,5	4.500	300	2,46	0,008	0,067	109.756
66	0,0105	86.400	55	0,55	0,105	0,01	60	4.500	650	11,66	0,010	0,606	26.340
67	0,0105	3.600	55	0,1	0,105	0,105	30,5	4.500	300	3,983	0,007	0,038	35.589
68	0,0105	45.000	10	0,1	0,105	0,105	30,5	1.000	650	3,983	0,007	0,038	17.135
69	0,0105	45.000	100	0,55	0,105	0,01	30,5	4.500	1000	11,66	0,020	0,606	40.523
70	0,02	45.000	55	0,1	0,105	0,105	1	4.500	650	5,429	0,285	0,027	56.571
71	0,0105	45.000	10	0,55	0,105	0,2	30,5	4.500	1.000	1,291	0,002	0,067	365.995
72	0,0105	45.000	55	0,1	0,01	0,01	30,5	4.500	650	16,091	0,003	0,152	1.818
73	0,0105	3.600	55	0,55	0,105	0,01	60	4.500	650	11,66	0,010	0,606	26.340
74	0,0105	45.000	10	0,55	0,105	0,01	30,5	4.500	1.000	11,66	0,020	0,606	40.523

Caso	$\dot{m}$ [kg/s]	β [s]	Amp_{ent} [K]	L [m]	e_s [m]	e_f [m]	k_s [W/mK]	ρ_s [kg/m³]	$c_{p,s}$ [J/kgK]	h [W/m²K]	Bi [-]	NTU [-]	τ [s]
75	0,0105	45.000	55	0,55	0,105	0,105	30,5	4.500	650	1,901	0,003	0,099	161.560
76	0,0105	3.600	55	0,55	0,2	0,105	30,5	8.000	650	1,901	0,006	0,099	547.080
77	0,02	45.000	55	0,55	0,105	0,2	30,5	8.000	650	1,721	0,003	0,047	317.257
78	0,001	45.000	55	1	0,105	0,105	60	4.500	650	1,061	0,001	1,053	289.467
79	0,02	86.400	10	0,55	0,105	0,105	30,5	4.500	650	2,46	0,004	0,067	124.848
80	0,001	45.000	55	1	0,105	0,105	1	4.500	650	1,061	0,056	1,053	289.467
81	0,0105	45.000	10	0,55	0,2	0,105	60	4.500	650	1,901	0,003	0,099	307.733
82	0,0105	45.000	10	0,1	0,105	0,105	30,5	8.000	650	3,983	0,007	0,038	137.083
83	0,001	45.000	55	0,55	0,105	0,2	30,5	8.000	650	0,633	0,001	0,345	862.559
84	0,001	45.000	55	0,55	0,105	0,2	30,5	1.000	650	0,633	0,001	0,345	107.820
85	0,0105	45.000	55	0,55	0,105	0,105	30,5	4.500	650	1,901	0,003	0,099	161.560
86	0,02	45.000	55	0,1	0,105	0,105	60	4.500	650	5,429	0,005	0,027	56.571
87	0,0105	45.000	55	0,1	0,2	0,2	30,5	4.500	650	2,85	0,009	0,027	205.263
88	0,0105	45.000	55	0,55	0,105	0,105	1	1.000	300	1,901	0,100	0,099	16.570
89	0,0105	45.000	55	0,55	0,105	0,105	30,5	4.500	650	1,901	0,003	0,099	161.560
90	0,0105	86.400	55	0,55	0,01	0,105	30,5	8.000	650	1,901	0,000	0,099	27.354
91	0,0105	45.000	100	0,55	0,105	0,2	30,5	4.500	1.000	1,291	0,002	0,067	365.995
92	0,0105	45.000	55	0,55	0,105	0,105	60	8.000	1.000	1,901	0,002	0,099	441.873
93	0,0105	86.400	55	0,55	0,01	0,105	30,5	8.000	650	1,901	0,000	0,099	27.354
94	0,0105	45.000	10	0,55	0,105	0,01	30,5	4.500	300	11,66	0,020	0,606	12.157
95	0,02	45.000	55	1	0,105	0,105	1	4.500	650	1,934	0,102	0,096	158.803
96	0,02	45.000	55	0,1	0,105	0,105	60	4.500	650	5,429	0,005	0,027	56.571
97	0,0105	45.000	55	0,55	0,105	0,105	60	1.000	300	1,901	0,002	0,099	16.570
98	0,0105	45.000	55	0,1	0,2	0,01	30,5	4.500	650	16,091	0,053	0,152	36.356
99	0,0105	45.000	55	0,1	0,01	0,2	30,5	4.500	650	2,85	0,000	0,027	10.263
100	0,02	45.000	55	0,1	0,105	0,105	1	4.500	650	5,429	0,285	0,027	56.571

Caso	$\dot{m}$ [kg/s]	β [s]	Amp_{ent} [K]	L [m]	e_s [m]	e_f [m]	k_s [W/mK]	ρ_s [kg/m³]	$c_{p,s}$ [J/kgK]	h [W/m²K]	Bi [-]	NTU [-]	τ [s]
101	0,0105	86.400	55	0,55	0,2	0,105	30,5	8.000	650	1,901	0,006	0,099	547.080
102	0,0105	3.600	55	1	0,105	0,105	30,5	4.500	1.000	1,555	0,003	0,147	303.859
103	0,0105	45.000	100	1	0,105	0,105	30,5	8.000	650	1,555	0,003	0,147	351.125
104	0,0105	3.600	55	0,55	0,2	0,105	30,5	8.000	650	1,901	0,006	0,099	547.080
105	0,0105	86.400	55	1	0,105	0,105	30,5	4.500	300	1,555	0,003	0,147	91.158
106	0,001	45.000	55	0,55	0,2	0,105	30,5	4.500	300	1,11	0,004	0,606	243.243
107	0,0105	86.400	55	0,55	0,01	0,105	30,5	1.000	650	1,901	0,000	0,099	3.419
108	0,001	45.000	55	0,55	0,01	0,105	30,5	4.500	300	1,11	0,000	0,606	12.162
109	0,0105	86.400	55	0,55	0,2	0,105	30,5	8.000	650	1,901	0,006	0,099	547.080
110	0,001	86.400	10	0,55	0,105	0,105	30,5	4.500	650	1,11	0,002	0,606	276.689
111	0,02	3.600	10	0,55	0,105	0,105	30,5	4.500	650	2,46	0,004	0,067	124.848
112	0,0105	45.000	100	0,55	0,105	0,2	30,5	4.500	300	1,291	0,002	0,067	109.799
113	0,0105	45.000	10	0,55	0,01	0,105	60	4.500	650	1,901	0,000	0,099	15.387
114	0,02	3.600	100	0,55	0,105	0,105	30,5	4.500	650	2,46	0,004	0,067	124.848
115	0,001	45.000	55	0,1	0,105	0,105	60	4.500	650	1,532	0,001	0,152	200.473
116	0,001	3.600	100	0,55	0,105	0,105	30,5	4.500	650	1,11	0,002	0,606	276.689
117	0,0105	3.600	55	0,55	0,01	0,105	30,5	1.000	650	1,901	0,000	0,099	3.419
118	0,0105	45.000	10	0,55	0,105	0,01	30,5	4.500	300	11,66	0,020	0,606	12.157
119	0,02	45.000	55	1	0,105	0,105	1	4.500	650	1,934	0,102	0,096	158.803
120	0,001	45.000	55	1	0,105	0,105	1	4.500	650	1,061	0,056	1,053	289.467
121	0,001	45.000	55	0,55	0,01	0,105	30,5	4.500	1.000	1,11	0,000	0,606	40.541
122	0,0105	45.000	55	0,55	0,105	0,105	30,5	4.500	650	1,901	0,003	0,099	161.560
123	0,0105	45.000	100	0,55	0,2	0,105	1	4.500	650	1,901	0,190	0,099	307.733
124	0,02	45.000	55	1	0,105	0,105	60	4.500	650	1,934	0,002	0,096	158.803
125	0,0105	3.600	55	0,55	0,105	0,01	1	4.500	650	11,66	0,612	0,606	26.340
126	0,0105	3.600	55	0,55	0,01	0,105	30,5	8.000	650	1,901	0,000	0,099	27.354

Caso	$\dot{m}$ [kg/s]	β [s]	Amp_{ent} [K]	L [m]	e_s [m]	e_f [m]	k_s [W/mK]	ρ_s [kg/m³]	$c_{p,s}$ [J/kgK]		h [W/m²K]	Bi [-]	NTU [-]	τ [s]
127	0,0105	45.000	10	0,55	0,2	0,105	1	4.500	650		1,901	0,190	0,099	307.733
128	0,0105	45.000	100	0,55	0,105	0,01	30,5	4.500	300		11,66	0,020	0,606	12.157
129	0,001	45.000	55	0,1	0,105	0,105	1	4.500	650		1,532	0,080	0,152	200.473
130	0,0105	45.000	100	0,55	0,105	0,01	30,5	4.500	300		11,66	0,020	0,606	12.157

Tabela A.2 - Resultados dos casos simulados em CFD e LEM.

Caso	$Amp_{sai,LEM}$ [K]	$Amp_{sai,CFD}$ [K]	Amp_{ent} [K]	Desvio Amplitude [%]		$t_{fase,sai,LEM}$ [s]	$t_{fase,sai,CFD}$ [s]	β [s]	Desvio fase [%]
1	8,738	8,583	10	1,550		348.788	348.809	45.000	0,093
2	45,097	43,985	55	2,022		27.905	27.911	3.600	0,333
3	8,996	8,9657	10	0,303		349.456	349.561	45.000	0,467
4	45,08	44,324	55	1,375		348.796	348.818	45.000	0,098
5	16,137	15,599	55	0,978		348.904	348.985	45.000	0,360
6	45,194	44,083	55	2,020		348.875	348.913	45.000	0,169
7	46,399	45,834	55	1,027		670.540	670.744	86.400	0,472
8	92,82	91,759	100	1,061		348.806	348.827	45.000	0,093
9	40,599	38,898	55	3,093		348.905	349.001	45.000	0,427
10	48,067	47,284	55	1,424		27.900	27.911	3.600	0,611
11	41,072	39,889	55	2,151		669.963	670.029	86.400	0,153
12	45,331	44,355	55	1,775		348.784	348.809	45.000	0,111
13	54,063	54,162	55	0,180		124.071	124.083	45.000	0,053
14	29,522	29,553	55	0,056		350.230	350.238	45.000	0,036
15	0,00	1,077	55	1,958		-	-	45.000	0,000
16	87,985	86,704	100	1,281		669.988	670.094	86.400	0,245
17	50,484	50,43	55	0,098		125.381	125.369	45.000	0,053
18	48,174	47,384	55	1,436		669.811	669.882	86.400	0,164
19	48,174	47,565	55	1,107		669.811	669.855	86.400	0,102
20	8,763	8,623	10	1,400		348.873	348.919	45.000	0,204
21	50,616	50,29	55	0,593		348.965	349.016	45.000	0,227
22	6,31	5,807	55	0,915		349.502	349.903	45.000	1,782
23	45,194	44,083	55	2,020		348.875	348.913	45.000	0,169
24	52,468	52,467	55	0,002		583.701	583.794	86.400	0,215

Caso	$Amp_{sai,LEM}$ [K]	$Amp_{sai,CFD}$ [K]	Amp_{ent} [K]	Desvio Amplitude [%]	$t_{fase,sai,LEM}$ [s]	$t_{fase,sai,CFD}$ [s]	β [s]	Desvio fase [%]
25	45,454	44,409	55	1,900	348.873	348.907	45.000	0,151
26	34,055	34,76	100	0,705	351.477	351.585	45.000	0,480
27	46,399	45,834	55	1,027	670.540	670.743	86.400	0,470
28	50,989	50,396	55	1,078	27.900	27.902	3.600	0,111
29	89,957	89,658	100	0,299	304.456	304.545	45.000	0,396
30	50,609	50,49	55	0,216	304.217	304.300	45.000	0,369
31	48,067	47,397	55	1,218	27.900	27.912	3.600	0,667
32	3,406	3,475	10	0,690	351.477	351.589	45.000	0,498
33	7,752	7,685	55	0,122	352.577	353.081	45.000	2,240
34	45,236	44,164	55	1,949	348.901	348.948	45.000	0,209
35	2,963	2,882	10	0,810	27.903	27.953	3.600	2,778
36	29,878	29,207	100	0,671	671.248	671.760	86.400	1,185
37	45,706	44,888	55	1,487	349.094	349.183	45.000	0,396
38	45,072	44,027	55	1,900	27.902	27.908	3.600	0,333
39	82,012	79,987	100	2,025	348.816	348.839	45.000	0,102
40	87,633	86,226	100	1,407	348.873	348.919	45.000	0,204
41	48,06	47,202	55	1,560	348.788	348.802	45.000	0,062
42	89,957	90,036	100	0,079	304.456	304.552	45.000	0,427
43	45,194	44,083	55	2,020	348.875	348.913	45.000	0,169
44	40,599	39,205	55	2,535	348.905	348.983	45.000	0,347
45	40,911	39,867	55	1,898	27.902	27.912	3.600	0,556
46	87,381	85,829	100	1,552	348.788	348.809	45.000	0,093
47	7,668	7,525	10	1,430	349.371	349.491	45.000	0,533
48	45,194	44,083	55	2,020	348.875	348.913	45.000	0,169
49	30,802	30,801	55	0,002	677.924	676.555	86.400	3,169

Caso	$Amp_{sai,LEM}$ [K]	$Amp_{sai,CFD}$ [K]	Amp_{ent} [K]	Desvio Amplitude [%]	$t_{fase,sai,LEM}$ [s]	$t_{fase,sai,CFD}$ [s]	β [s]	Desvio fase [%]
50	45,706	45,074	55	1,149	349.094	349.135	45.000	0,182
51	51,209	50,74	55	0,853	669.828	669.906	86.400	0,181
52	7,442	7,232	10	2,100	348.836	348.859	45.000	0,102
53	8,763	8,623	10	1,400	348.873	348.919	45.000	0,204
54	76,68	75,256	100	1,424	349.371	349.492	45.000	0,538
55	7,903	10,919	55	5,484	289.697	269.507	45.000	89,733
56	46,052	45,197	55	1,555	27.934	27.947	3.600	0,722
57	45,194	44,083	55	2,020	348.875	348.913	45.000	0,169
58	45,236	44,519	55	1,304	348.901	348.927	45.000	0,116
59	45,072	44,027	55	1,900	27.902	27.908	3.600	0,333
60	95,667	95,719	100	0,052	304.015	304.061	45.000	0,204
61	45,194	44,083	55	2,020	348.875	348.913	45.000	0,169
62	47,158	46,591	55	1,031	349.298	349.421	45.000	0,547
63	54,835	54,856	55	0,038	65.133	65.137	86.400	0,009
64	51,363	51,351	55	0,022	81.423	81.423	45.000	0,000
65	48,198	47,415	55	1,424	348.873	348.910	45.000	0,164
66	30,802	31,727	55	1,682	677.924	677.444	86.400	1,111
67	50,989	50,37	55	1,125	27.901	27.903	3.600	0,111
68	9,567	9,572	10	0,050	304.015	304.062	45.000	0,209
69	34,055	34,76	100	0,705	351.477	351.585	45.000	0,480
70	52,286	52,32	55	0,062	348.842	348.843	45.000	0,004
71	8,738	8,583	10	1,550	348.788	348.809	45.000	0,093
72	54,736	54,744	55	0,015	34.022	34.022	45.000	0,000
73	16,102	16,197	55	0,173	27.930	27.930	3.600	0,000
74	3,406	3,475	10	0,690	351.477	351.589	45.000	0,498

Caso	$Amp_{sai,LEM}$ [K]	$Amp_{sai,CFD}$ [K]	Amp_{ent} [K]	Desvio Amplitude [%]	$t_{fase,sai,LEM}$ [s]	$t_{fase,sai,CFD}$ [s]	β [s]	Desvio fase [%]
75	45,194	44,083	55	2,020	348.875	348.913	45.000	0,169
76	45,123	44,132	55	1,802	27.900	27.906	3.600	0,333
77	50,055	49,485	55	1,036	348.780	348.794	45.000	0,062
78	6,31	5,807	55	0,915	349.502	349.902	45.000	1,778
79	8,798	8,67	10	1,280	669.988	670.095	86.400	0,248
80	6,31	6,171	55	0,253	349.502	349.573	45.000	0,316
81	8,201	7,999	10	2,020	348.816	348.841	45.000	0,111
82	9,282	9,176	10	1,060	348.806	348.827	45.000	0,093
83	27,384	26,396	55	1,796	348.833	348.950	45.000	0,520
84	27,873	26,99	55	1,605	349.397	349.689	45.000	1,298
85	45,194	44,083	55	2,020	348.875	348.913	45.000	0,169
86	52,286	52,061	55	0,409	348.842	348.862	45.000	0,089
87	52,123	51,702	55	0,765	348.777	348.789	45.000	0,053
88	49,12	49,006	55	0,207	304.450	304.534	45.000	0,373
89	45,194	44,083	55	2,020	348.875	348.913	45.000	0,169
90	49,853	49,924	55	0,129	584.558	584.734	86.400	0,407
91	87,381	85,829	100	1,552	348.788	348.809	45.000	0,093
92	45,08	43,961	55	2,035	348.796	348.814	45.000	0,080
93	49,853	49,924	55	0,129	584.558	584.734	86.400	0,407
94	6,021	6,146	10	1,250	308.031	307.812	45.000	0,973
95	45,454	44,787	55	1,213	348.873	348.896	45.000	0,102
96	52,286	52,061	55	0,409	348.842	348.862	45.000	0,089
97	49,12	49,141	55	0,038	304.450	304.544	45.000	0,418
98	42,273	42,218	55	0,100	349.493	349.512	45.000	0,084
99	54,004	54,113	55	0,198	168.933	168.947	45.000	0,062

Caso	$Amp_{sai,LEM}$ [K]	$Amp_{sai,CFD}$ [K]	Amp_{ent} [K]	Desvio Amplitude [%]	$t_{fase,sai,LEM}$ [s]	$t_{fase,sai,CFD}$ [s]	β [s]	Desvio fase [%]
100	52,286	52,32	55	0,062	348.842	348.844	45.000	0,009
101	45,114	44,003	55	2,020	669.737	669.778	86.400	0,095
102	40,96	39,952	55	1,833	27.901	27.911	3.600	0,556
103	74,417	72,322	100	2,095	348.836	348.856	45.000	0,089
104	45,123	44,132	55	1,802	27.900	27.906	3.600	0,333
105	42,015	41,188	55	1,504	670.717	670.930	86.400	0,493
106	16,169	15,426	55	1,351	349.264	349.455	45.000	0,849
107	54,835	54,856	55	0,038	65.133	65.137	86.400	0,009
108	33,115	35,1	55	3,609	308.031	307.938	45.000	0,413
109	45,114	44,003	55	2,020	669.737	669.778	86.400	0,095
110	2,988	2,841	10	1,470	671.248	671.762	86.400	1,190
111	8,737	8,589	10	1,480	27.901	27.905	3.600	0,222
112	87,633	86,226	100	1,407	348.873	348.919	45.000	0,204
113	8,996	9,003	10	0,070	349.456	349.552	45.000	0,427
114	87,37	85,891	100	1,479	27.901	27.904	3.600	0,167
115	40,599	38,898	55	3,093	348.905	349.001	45.000	0,427
116	29,629	28,817	100	0,812	27.903	27.953	3.600	2,778
117	46,052	45,197	55	1,555	27.934	27.947	3.600	0,722
118	6,021	6,146	10	1,250	308.031	307.812	45.000	0,973
119	45,454	44,787	55	1,213	348.873	348.896	45.000	0,102
120	6,31	6,171	55	0,253	349.502	349.573	45.000	0,316
121	18,73	18,833	55	0,187	351.477	352.015	45.000	2,391
122	45,194	44,083	55	2,020	348.875	348.913	45.000	0,169
123	82,012	81,081	100	0,931	348.816	348.848	45.000	0,142
124	45,454	44,409	55	1,900	348.873	348.907	45.000	0,151

Caso	$Amp_{sai,LEM}$ [K]	$Amp_{sai,CFD}$ [K]	Amp_{ent} [K]	Desvio Amplitude [%]		$t_{fase,sai,LEM}$ [s]	$t_{fase,sai,CFD}$ [s]	β [s]	Desvio fase [%]
125	16,102	18,535	55	4,424		27.930	27.960	3.600	1,667
126	45,097	43,985	55	2,022		27.905	27.911	3.600	0,333
127	8,201	8,108	10	0,930		348.816	348.850	45.000	0,151
128	60,208	61,484	100	1,276		353.031	352.809	45.000	0,987
129	40,599	39,205	55	2,535		348.905	348.983	45.000	0,347
130	60,208	61,484	100	1,276		353.031	352.809	45.000	0,987

Tabela A.3 - Resultados da análise dos efeitos significativos utilizando o software Minitab 18.

	Dados da amplitude						Dados da Fase					
Termo	Efeito	Coef.	SE Coef.	Valor-T	Valor-P	VIF	Efeito	Coef.	SE Coef.	Valor-T	Valor-P	VIF
Constant	-	2	0,219	9,24	0	-	-	0,17	2,17	0,08	0,938	-
$\dot{m}$	-0,824	-0,412	0,109	-3,77	0	1	-5,33	-2,67	1,09	-2,45	0,016	1
β	-0,622	-0,311	0,109	-2,85	0,006	1	-0,16	-0,08	1,09	-0,07	0,941	1
Amp_{in}	-0,035	-0,017	0,109	-0,16	0,874	1	-0,01	0	1,09	0	0,997	1
L	0,369	0,185	0,109	1,69	0,095	1	0,37	0,19	1,09	0,17	0,864	1
e_s	0,689	0,345	0,109	3,15	0,002	1	-0,08	-0,04	1,09	-0,04	0,971	1
e_f	0,191	0,096	0,109	0,88	0,384	1	-4,92	-2,46	1,09	-2,26	0,026	1
k	0,284	0,142	0,109	1,3	0,198	1	-0,01	0	1,09	0	0,998	1
ρ_s	0,356	0,178	0,109	1,63	0,108	1	-4,67	-2,34	1,09	-2,15	0,035	1
c_{P_s}	-0,068	-0,034	0,109	-0,31	0,756	1	-0,07	-0,04	1,09	-0,03	0,974	1
$\dot{m}^2$	-0,216	-0,108	0,146	-0,74	0,461	1,23	6,02	3,01	1,45	2,08	0,041	1,23
β^2	-0,225	-0,113	0,146	-0,77	0,442	1,23	-1,25	-0,63	1,45	-0,43	0,667	1,23
${Amp_{in}}^2$	-0,779	-0,389	0,146	-2,67	0,009	1,23	-1,66	-0,83	1,45	-0,57	0,567	1,23
L^2	-0,855	-0,428	0,146	-2,94	0,004	1,23	-2,15	-1,08	1,45	-0,74	0,46	1,23
${e_s}^2$	-1,142	-0,571	0,146	-3,92	0	1,23	-1,98	-0,99	1,45	-0,68	0,497	1,23
${e_f}^2$	-0,536	-0,268	0,146	-1,84	0,07	1,23	5,8	2,9	1,45	2	0,049	1,23
k^2	-0,529	-0,264	0,146	-1,81	0,074	1,23	-1,8	-0,9	1,45	-0,62	0,536	1,23
${\rho_s}^2$	-0,204	-0,102	0,146	-0,7	0,485	1,23	5,16	2,58	1,45	1,78	0,079	1,23
${c_{P_s}}^2$	-0,422	-0,211	0,146	-1,45	0,152	1,23	-2	-1	1,45	-0,69	0,493	1,23
$\dot{m}\beta$	-0,229	-0,115	0,244	-0,47	0,64	1	0,82	0,41	2,43	0,17	0,866	1
$\dot{m}Amp_{in}$	0,199	0,1	0,244	0,41	0,685	1	-0,01	-0,01	2,43	0	0,998	1
$\dot{m}L$	1,775	0,888	0,173	5,14	0	1	-0,29	-0,15	1,72	-0,08	0,933	1
$\dot{m}e_s$	1,014	0,507	0,244	2,07	0,041	1	0,35	0,17	2,43	0,07	0,943	1
$\dot{m}e_f$	1,379	0,689	0,244	2,82	0,006	1	22,03	11,01	2,43	4,53	0	1
$\dot{m}k$	-0,046	-0,023	0,173	-0,13	0,894	1	-0,35	-0,18	1,72	-0,1	0,918	1

Termo	Efeito	Coef.	SE Coef.	Valor-T	Valor-P	VIF	Efeito	Coef.	SE Coef.	Valor-T	Valor-P	VIF
$\dot{m}\rho_s$	0,934	0,467	0,244	1,91	0,06	1	22,58	11,29	2,43	4,65	0	1
$\dot{m}c_{P_s}$	0,992	0,496	0,244	2,03	0,046	1	-0,32	-0,16	2,43	-0,07	0,948	1
βAmp_{in}	-0,2	-0,1	0,244	-0,41	0,684	1	0,01	0,01	2,43	0	0,998	1
βL	0,318	0,159	0,244	0,65	0,517	1	-0,16	-0,08	2,43	-0,03	0,974	1
βe_s	0,689	0,344	0,173	1,99	0,05	1	0,13	0,07	1,72	0,04	0,969	1
βe_f	0,704	0,352	0,244	1,44	0,154	1	-0,91	-0,45	2,43	-0,19	0,853	1
βk	1,514	0,757	0,244	3,1	0,003	1	-0,07	-0,03	2,43	-0,01	0,989	1
$\beta\rho_s$	0,179	0,089	0,173	0,52	0,607	1	0,1	0,05	1,72	0,03	0,976	1
βc_{P_s}	0,403	0,201	0,244	0,82	0,412	1	-0,09	-0,05	2,43	-0,02	0,985	1
$Amp_{in}\ L$	-0,003	-0,002	0,244	-0,01	0,994	1	0	0	2,43	0	1	1
$Amp_{in}\ e_s$	0	0	0,244	0	1	1	0,01	0,01	2,43	0	0,998	1
$Amp_{in}\ e_f$	-0,008	-0,004	0,173	-0,02	0,982	1	0	0	1,72	0	1	1
$Amp_{in}\ k$	0,004	0,002	0,244	0,01	0,993	1	0,02	0,01	2,43	0	0,997	1
$Amp_{in}\ \rho_s$	0	0	0,244	0	1	1	0	0	2,43	0	0,999	1
$Amp_{in}\ c_{P_s}$	-0,004	-0,002	0,173	-0,01	0,991	1	-0,01	0	1,72	0	0,998	1
Le_s	0,048	0,024	0,244	0,1	0,922	1	0,43	0,22	2,43	0,09	0,929	1
Le_f	0,453	0,227	0,244	0,93	0,357	1	-0,4	-0,2	2,43	-0,08	0,934	1
Lk	0,111	0,055	0,173	0,32	0,749	1	0,34	0,17	1,72	0,1	0,922	1
$L\rho_s$	-0,17	-0,085	0,244	-0,35	0,73	1	-0,16	-0,08	2,43	-0,03	0,973	1
Lc_{P_s}	-0,055	-0,028	0,244	-0,11	0,91	1	-0,08	-0,04	2,43	-0,02	0,987	1
$e_s e_f$	0,281	0,141	0,244	0,58	0,566	1	-0,69	-0,35	2,43	-0,14	0,887	1
$e_s k$	0,659	0,33	0,244	1,35	0,181	1	-0,02	-0,01	2,43	0	0,997	1
$e_s\rho_s$	0,084	0,042	0,173	0,24	0,808	1	-0,1	-0,05	1,72	-0,03	0,978	1
$e_s c_{P_s}$	0,787	0,394	0,244	1,61	0,111	1	-0,72	-0,36	2,43	-0,15	0,882	1
$e_f k$	0,776	0,388	0,244	1,59	0,116	1	0,93	0,47	2,43	0,19	0,848	1
$e_f\rho_s$	1,050	0,525	0,244	2,15	0,035	1	22,2	11,1	2,43	4,57	0	1
$e_f c_{P_s}$	0,357	0,178	0,173	1,03	0,305	1	0,19	0,1	1,72	0,06	0,956	1

Termo	Efeito	Coef.	SE Coef.	Valor-T	Valor-P	VIF		Efeito	Coef.	SE Coef.	Valor-T	Valor-P	VIF
$k\rho_s$	0,284	0,142	0,244	0,58	0,563	1		-0,05	-0,02	2,43	-0,01	0,993	1
kc_{P_s}	0,13	0,065	0,244	0,27	0,79	1		0,01	0,01	2,43	0	0,998	1
$\rho_s c_{P_s}$	-0,559	-0,279	0,244	-1,14	0,257	1		0,02	0,01	2,43	0	0,997	1